Scuola di Dottorato in Fisica, Astrofisica e Fisica Applicata
Dipartimento di Fisica

Corso di Dottorato in Fisica, Astrofisica e Fisica Applicata
Ciclo XXVIII

Optical detection of molecular interactions on the surface of materials index-matched to water

Settore Scientifico Disciplinare FIS/07

Supervisore: Prof. Marco BUSCAGLIA

Coordinatore: Prof. Marco BERSANELLI

Tesi di Dottorato di:
Roberta LANFRANCO

Anno Accademico 2014-2015

Commission of the final examination:

External Referee:
Antonio J. Ricco, - NASA Ames Research Center (USA)

External Member:
Giuseppe Chirico - Univeristá degli Studi Mialno Bicocca
Fabio Ferri - Universitá degli Studi dell'Insubria
Marco Malvezzi - CNR-IOM

Internal Member:
Marco Buscaglia - Univeristá degli Studi di Milano

Final examination:

Date 12/14/2015

Università degli Studi di Milano, Dipartimento di Fisica, Milano, Italy

It's better to burn out
than to fade away

Cover illustration:

Crowding of fluorinated micro-beads

MIUR subjects:

FIS/07

PACS:

82.70.Uv
87.64.Cc

Contents

Introduction

The idea to have highly effective autonomous sensors able to measure and share information about the quality of our environment, and particularly water, in our lakes and rivers, our water supply system and the outputs of municipal and industrial wastewater treatment systems is revolutionary and fascinating. These sensors could be densely deployed at multiple locations, and the information may be available to citizens through the Internet. This idyllic vision, nowadays, is far away from being reality, despite the huge effort made to develop innovative molecular sensors. The main challenges related to the realization of these autonomous sensors network are the biofouling, power supply and compactness. In fact, despite thousands of papers in literature about development of novel nanostractured materials for sensing, for instance, there is still not a single example of any of these device being used in direct contact with water for long-term environmental monitoring.

The work presented in this thesis proposes a new kind of optical sensor that combines a fast and low cost method to detect water pollutant with good performance and robustness. In particular, this work is focused on the detection of small molecular pollutants, as oils compounds and surfactants. An innovative aspect of the proposed approach relies on the use of a novel class of materials as sensing substrate which have peculiar and fascinating optical properties: these are amorphous perfluorinated polymers with refractive index similar to that of water. When immersed in aqueous solutions, they provide extremely low reflection or scattering of light, hence they become barely visible. For this reason, this class of materials is called *phantom*. In this limit, when a thin molecular layer spontaneously adsorbs on the surfaces of these materials, the reflected or scattered light increases, providing the basis for optical detection of molecules.

In this work, three different phantom materials made of perfluorinated polymers are exploited in the framework of the detection of water contaminants: a prism, microporous membranes and micro-beads, that represent the building blocks for the assembly of an invisible chromatography column. The membrane and the micro-beads were produced for the first time during this work. The use of fluoropolymer prism substrate for molecular detection was already proposed in recent works to realize label-free biosensors based on the functionalization of the surface with antibodies. Here I extend the exploitation of this system to the detection of molecular pollutant through their adsorption on the bare surface of the fluoropolymer materials, without the need of any surface treatment. Despite the lack of surface functionalization, a selectivity in the adsorption of various classes of molecules is demonstrated.

The thesis is organized in the following way.

In *Chapter 1*, I present the context and the motivations of the work, reviewing the common techniques used to detect small polluting molecules in water samples and introducing the NAPES project, an European project aiming at developing novel analytical solutions for water quality monitoring. A relevant part of this work was performed in the framework of this project.

In *Chapter 2*, I present the perfluorinated polymers isorefractive to water used in this work, Hyflon AD® and Fomblin MD®. First, I explain previous applications of these polymers, in the form of nano-particles and planar surface, applied in the context of label-free biosensing. Then, I report the realization of novel phantom substrates: microporous membranes and micro-beads. The porous membranes were realized thanks to the collaboration with the Membrane Laboratory of *Solvay Specialty Polymers*. I used the *Non-solvent Induce Phase Separation* technique to realize homogeneous and highly porous membranes. These samples presented a porosity from 50% to 70 %, a mean pore size from 1 to 10 μm and were highly transparent in water. Regarding the micro-beads, they were synthesized via emulsification technique followed by the droplets photopolymerization. To realize the fluorinated oil-in-water emulsion, I have explored different emulsification strategies: membrane and microfluidics emulsification. In this way, solid and stable phantom colloids, with an avarage diameter from 5 to 50 μm, were produced for the first time.

In *Chapter 3*, I developed various models that describe the optical response of these phantom materials when molecular adsorption takes place. In particular, I show how the reflectivity of a planar surface and the intensity of scattered light by complex systems increases due to the presence of molecular adsorption. The model for reflectivity is derived by the Fresnel formulas for thin film reflection. In the case of phantom porous materials, an increment in scattering light intenisty is expected when molcular adsorption occurs on their surfaces. To describe the optical responce of these porous materials, such as membranes and chromatography column, I present two different scattering models. One of these models is developed in the limit of weakly scattering media having various characteristic sizes, in the frame of Rayleigh-Gans approximation. In this context, I developed an optical model that accounts for both the reflective signal of the planar surface and the scattering signal of the micro-structured materials. The second scattering model derives from the *Random Telegraph Signal*: in this case, I demonster how it is possible to obtain the light intensity scattered by the medium knowing the morphology of the porous material.

The rest of the work is dedicated to the experimental study of the interaction between different substrates and molecules in water solution. *Chapter 4* and *Chapter 5* report experimental results obtained using two different planar surfaces; *Chapter 6* and *Chapter 7* regard the characterization of the optical response of porous materials and the fabrication of microfluidic devices hosting these novel substrates, respectively.

In *Chapter 4* results concerning an extremely weak reflection sensor based on a different concept is presented. In this case, the substrate is a glass prism with optimized anti-reflective coating. Differently from fluorinated plastics, this glass chip is functionalized with a suitable copolymer and specific antibodies for diagnostic application.

Chapter 5 reportes the study of molecular interaction on the bare planar surface of a prism made of perfluorinated polymer. The adsorption of molecules provides an increase of optical reflectivity. I have experimentally investigated the spontaneous adsorption of various molecules: surfactants with different charge, a protein (lysozyme) and a constituent of gasoline (hexane). I demonstrate that suitable theoretical adsorption models, accounting for adsorption and transport, enable to extract all the relevant parameters of the molecule/surface interaction. I found that, at equilibrium, the strength of interac-

tion scales with the molecular hydrophobic contact area on the fluorinated surface. From the kinetics behavior, I found that the observed adsorption rate scales with the number of available adsorption sites and the molecular diffusion coefficient, so again with the size of the molecule. With the same experimental set-up, detection measurements using real river water samples were also performed.

Chapter 6 reports the use of microporous membrane made of the same material of the prism to detect surfactants into water. Commercial membrane filters and newly realized phantom porous membranes were optically characterized, by two different optical techniques: a static light scattering and processing of microscope images. In this way, I found that membranes with different internal morphologies have different optical responses, as predicted by the models. By means of model described in *Chapter 3*, the optical signal provided a measurement of the amount of molecules adsorbed on the surface. Concerning the adsorption studies on perfluorinated membranes, I found that the thickness of surfactant layer that forms on the inner surfaces of the micro-porous membrane is in agreement with that obtained on the planar surface of the prism sensor, *Chapter 5*.

Finally, the development of microfluidics devices incorporating porous membranes and micro-beads and their first experimental tests are presented, *Chapter 7*.

This work has regarded the realization of new substrates for optical detection of pollutant molecules in water samples. It was both experimental and theoretical, in order to prove and describe the molecular adsorption on these various phantom materials. The main results obtained in this work can be summarized as follow:

- realization of newly phantom substrates: micro-porous membranes and microbeads;
- development of novel optical models decribing the increase of scattered light intensity by a micro-structured medium in index-matching condition, when it is covered by a thin molecular layer;
- despite the different adsorption processes occurring on various phantom materials, I developed an unique optical model that accounts for the optical response of both reflective and scattering substrates interested by adsorption;
- characterization of the interaction between different molecules and the perfluorinated plastic: the strength and the kinetics of adsorption are found to depend on the size of the molecules;
- realization of novel micro-fluidic devices hosting porous membranes and microbeads.

Chapter 1:
Water pollutants

Water pollution is one of the biggest problem of this century: having uncontaminated water to drink and to use in agricultural processes is fundamental for human life. In this chapter, I am going to describe the main problems related to the presence of polluting molecules in water, from bacteria to surfactants and oils. In particular I focus on surfactants, explaining their characteristic and the most commonly used techniques to detect such molecules in a water sample. Finally, I present the NAPES project (*Next generation Analytical Platforms for Environmental Sensing*), a European project, the goal of which is to develop a network of autonomous sensors to detect various kinds of pollutants in river water.

1.1 Contaminated waters

Water is the most important resource that humans have: it is essential for living beings and it is also fundamental for all human activities dependent on, such as industrial processes, agricultural production and domestic use. Nonetheless, every day, many of these activities pour into the aquatic ecosystem tons of harmful materials, threatening the survival of the flora and fauna of our lakes, rivers and seas [1] [2] [3]. Because of the extreme importance of aquatic ecosystems, it is necessary to continually monitor the health status of these water reservoirs. Some of the most widespread pollutants, which must be continually monitored to avoid water contamination, include fecal pollutants, harmful organic and inorganic substances and free oils and emulsifiers, such as the compounds that are the basis of the detergents and soaps. Despite a general commitment to improve water quality, according to data collected by the World Health Organization, more than a sixth the world's population, ~ 900 million people, do not have access to safe drinking water. In addition, 2.6 billion people worldwide live in the absence of the most basic sanitary conditions, from which frequent infections and deaths result. The most common and widespread risks for health are related to infectious diseases caused by pathogenic bacteria, viruses and protozoa parassiti. Some pathogenic microorganisms transported by water can cause serious illness or death, such as typhoid fever, cholera and hepatitis A or E. Others microorganisms cause less dangerous disease, of which diarrhea is often the main symptom. In particular, the strain O157: H7 Escherichia Coli can lead to bloody diarrhea, and, occasionally, to renal failure and death.

Other organic pollutants widely present in river water include surfactants and oily compounds. Due to their hydrophobic nature, these molecules migrate to air/water interfaces, preventing proper oxygen exchange within and between ecosystems. Moreover, they self-assemble on surfaces of living orgaanisms, causing, in the worst cases, their death. In analytical laboratories, colorimetric methods, liquid chromatography and mass-spectroscopy are common and widely employed approaches to detect contaminants in liquids and solubilized media. However, the most common and widespread techniques to detect surfactants or oily compounds in water samples require several analytical steps performed by highly specialized personnel in suitably furnished laboratories, hence typically being expensive and time consuming. Innovative nano-structured materials, novel electrochemical transducers and engineered biomolecular probes may also provide improved detection performance under controlled laboratory conditions. Nevertheless, none of these approaches has yet met all the requirements for an inexpensive deployable system. The goal of this work is the realization of novel materials and innovative detection methods enabling the non-invasive detection of water pollutants by autonomous, deployable devices.

1.2 Surfactants

Surfactants are a particular class of molecules that decrease the surface tension of a liquid, facilitating the wetting of a surface or the miscibility of two different liquids. Generally, surfactants are made of two different parts: an hydrophobic tail and a hydrophilic head, **Figure 1.1**. Depending on the net charge of the hydrophilic part, surfactants are grouped in four classes.

- cationic: the head group is positively charged; for example, molecules composed of long carbon chains ending with an ammino group;

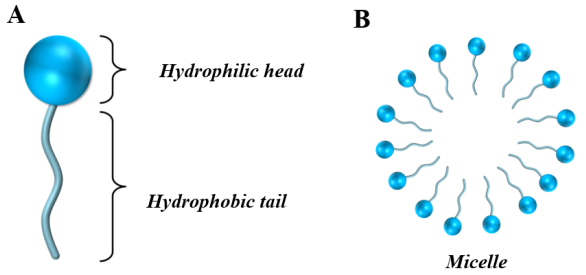

Figure 1.1: Surfactant: A) Schematic representation of a surfactant B) and of a micelle.

- anionic: negatively charged; for example molecules composed of long carbon chain ending with a carboxylate group;
- nonionic: uncharged, predominantly made of alcohol-based chains;
- zwitterionic: both cationic and anionic centers attached to the same molecule; their charge depends on solvent pH.

Most surfactants when highly concentrated, self-assemble into aggregates (micelle, **Figure 1.1**) a process driven by hydrophobic interactions that result in exposuse of least possible area of the hydrophobic chain to water. The surfactant concentration at which this phenomena occurs is called critical micellar concentration (CMC).

Thanks to their amphiphilic nature, surfactants are widely used into the production of soaps, detergents and in a vast number of industrial processes. Their hydrophobic part adheres to oily and fatty molecules dispersed into water, meanwhile their hydrophilic part stays in water. By this mechanism they solubilize hydrophobic compounds, enabling the removal of dirt from, for example, a piece of cloth. For this reason, surfactants are widely present in wastewater and, if these waters are not properly treated, may find their way to the aquatic environment. For precisely the same reasons that make them "washing molecules", surfactants are strong pollutants. They can self-assemble, for example, at a water-air interface, forming a thin molecular layer, that prevents proper exchange with the atmosphere of oxigen and other gaseous compounds, such as carbon dioxide, methane, sulfur oxides and ammonia that come from the decomposition of organic material in the water. Moreover, they destroy the thin protective mucus layer that covers fish, damaging their gills. It is clear that the presence of surfactants in water can substantially disturb the ecosystem. It is therefore evident that a method to monitor the presence of these polluting molecules in the aquatic ecosystem is a fundamental component of maintaining the health of water ecosystems.

1.3 Common techniques to detect surfactants

Surfactant detection is a research field of great interest and active development. Monitoring surfactant presence in water is so important that the European Union has issued in an official bulletin (12.3.2004 C64E/553) [4] the standard procedure to detect the presence of anionic, non ionic, cationic and zwitterionic surfactants. In this document, for instance, the detection of anionic surfactants must be achieved with the methylene blue active substance method (MBAS). This technique is based on the specificity of methylen

blue, a cationic dye, to form an ion pair with anionic surfactants, which can then be extracted into an organic phase (chloroform). To avoid interferences, the extraction step is conducted in alkaline solution. The organic phase optical absorbance is measured with a spectrophotometer: the color of chloroform increases with increasing concentration of surfactant. This method enables the detection of anionic surfactant concentrations from 0.02 to 5.0 mg/L. The main problem of this technique is that methylen blue is harmful to humans, leading to the question of how to dispose of the hazardous waste. Moreover, the analysis can be affect by the presence of cationic surfactants. The techniques presented in the bulletin to detect other classes of surfactant are all colorimetric [5]; like the MBAS, they require challenging sample preparation, create chemical hazards and do not identify specific surfactants.

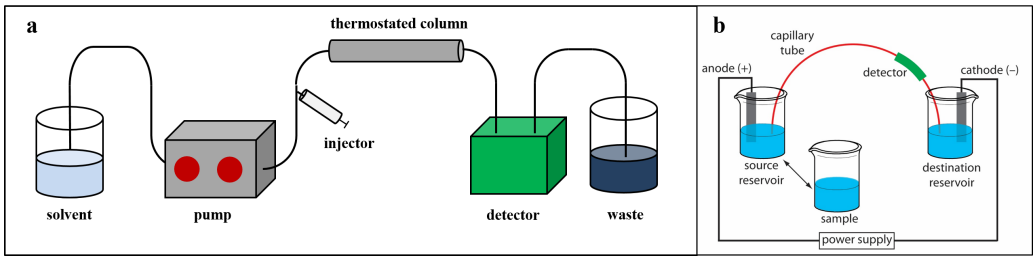

Figure 1.2: Two different methods to separe and anlayze surfactants in water samples: a) high-performance liquid chromatography (HPLC) and b) capillary electrophoresis (CE). In HPLC, the solvent is pumped through the chromatography column after injection of the water sample to be analyzed. After passing through the column, the eluant is analyzed with variuos techniques described in the text; the effluent is collected as waste. In CE, a constant potential difference is maintained between the ends of a capillary. Changes in conductivity are then measured as the water sample flows through the capillary.

New methods have been developed, to overcome problems related to the standard analysis just described. Here I report some of these new proposed methods. Microporous liquid-liquid membrane extraction (MMLLE) [6] is based on filtering a water sample through a hydrophobic membrane, on which surfactants spontaneously adsorb. Subswquently, surfactants are removed from the membrane with an organic solvent and analyzed using high-performance liquid chromatography (HPLC), **Figure 1.2a**. HPLC is an analytical technique used to separate, identify, and quantify each component of a mixture [7]. It relies on pumps to pass a pressurized liquid solvent containing the sample mixture through a column filled with a solid adsorbent material. Each component in the sample interacts slightly differently with the adsorbent material, causing different net flow rates for the different components and leading to the separation of these components so that they flow out of the column at different times. With this method it is possible to have high selectivity for the separation of anionic, nonionic and cationic surfactants in relatively short times (less than an hour). By analyzing of the eluant it is possible to learn the starting surfactant concentrations in the sample. The detection limit of MMLE is 0.7 $\mu g/L$, but this method is quite complex and time-consuming.

Another method contemplates the replacement of the chromatography column and detector by electro-spray ionization in combination with mass spectroscopy (ESI-MS). Implementing different spray ionization conditions can enable the simultaneous detection of multiple type of surfactant. The sensitivity range of this technique is 0.3-2.0 $\mu g/L$.

Another well-used technique to separe surfactants in aqueous solution is capillary electrophoresis (CE), **Figure 1.2b**. CE is a family of electrokinetic separation methods performed in submillimeter diameter capillaries and in micro- and nano-fluidic channels [8]. In this methods, analytes migrate through electrolyte solutions under the influence

of an electric field and are separated according to their mobility and/or by partitioning them into an alternate phase via non-covalent interactions. After the separation, various methods can be applied to detect the surfactant presence and concentration, such indirect photometric detection (IPD) or indirect conductivity detection (ICD). IPD [9] is often employed for the detection of cations and anions that lack suitable chromophores. In this form of detection, an absorbing co-ion, called the probe, is added to the background electrolyte. The detection is accomplished by displacemen of the co-ion, leading to a quantifiable decrease in background absorbance. In the case of ICD [10], the detected signal is the change of background conductivity due to an electrolyte, in which the CE eluant is dissolved. Detection limits of this techniques are quite high, about 6 mg/L, for the surfactants. These indirect detection methods should be avoided whenever possible because they are characterized by a limited working range, low sensitivity and specificity, and a strong dependence on temperature.

All of the above techniques must be performed in a chemical laboratory by expert personnel, are time consuming, expensive and can not be performed in real time, nor directly in the place where the water sample is obtained. The aim of this work is therefore to explore the possibility of realizing an instrument that detects the presence of polluting molecules, pheraps with less selectivity or sensitivity, but autonomous: a long-life sensor that, in real time, gives information about the polluting molecule concentration of surface waters.

1.4 NAPES Project

NAPES project (*Next generation Analytical Platforms for Environmental Sensing*) is supported by the European Union's Seventh Framework Programme for research, technological development and demonstration. *NAPES* investigates ways to deliver revolutionary advances in liquid/sample handling combined with new approaches to performing sensitive in-situ analytical measurements. Its goal is to drive down the unit cost of the associated instruments by orders of magnitude, to levels that can create a tipping point, at which the technology becomes ubiquitous.

The idealized objective of the *NAPES* project is to enable a highly effective autonomous sensor network to measure and share information about the quality of our environment, particularly water, in our lakes and rivers, water-supply systems, and outputs of municipal and industrial wastewater treatment systems. These sensors would be densely deployed at multiple locations; the information would be available to citizens through the Internet. It is a matter of great concern that, even today, science and technology cannot deliver an effective platform to make this idyllic vision a reality, and the gap between what is currently available, and what is actually needed remains very significant despite a massive effort to develop innovative molecular sensors over the past 20 years, an effort that has generated thousands of papers in the technical literature, without delivering a practical solution to the real issues associated with distributed environmental sensing. In recent years, many of these papers describe ingenious use of nanostructured materials, which, under controlled laboratory conditions, exhibit greatly improved characteristics compared to more conventional sensor materials.

However, despite these seemingly exciting breakthroughs, there is still not a single example of any of these devices being used in direct contact with water in practical deployments for long-term environmental monitoring. This is mainly due to the impact of direct exposure to real environments on these exquisitely nanostructured sensor surfaces, which rapidly leads to bio-fouling, leaching of surface components, irreversible

binding of interferes, and other processes that change the surface properties, and therefore the response characteristics of these sensors [11].

The practical solution to changes in interfacial surface properties is to enclose the sensors within a rugged enclosure, and to transport the sample to the sensors through a filtration unit that eliminates degrading and interfering components. Rather than a 'sensor', therefore, 'sensor systems' or 'platforms' would be employed to perform calibrations, add reagents and perform cleaning cycles. Consequently, such platforms would have to be able to acquire a sample, perform various actions on the sample (filter, add reagents), perform one or more measurements, store any hazardous waste generated, and make the results remotely available. In addition, they would have to undertake self diagnosis to detect faults through regular calibration, using one or more stable standards, which would need to be delivered to the detector in place of the sample.

The current state-of-the-art for autonomous environmental sensor-based monitoring of the chemical and biological status of our water includes flow systems that employ conventional pumps, valves and fluid handling components, and because of this, systems are prohibitively expensive (often $>$ \$20k per unit); the deployment model is inherently not scalable. Examples include the ABB Aztec 600 series analysers, and the Microlab 500 series, both of which incorporate expensive syringe pumps for flow generation. Still today, the vast bulk of analytical measurements related to the environment are performed in centralized facilities, from samples obtained manually 3 or 4 times per year at a limited number of locations. The key to changing this model is to drive down the unit cost – e.g. by making autonomous chemical sensors available for a unit cost of \$20 or even \$2 This is not a trivial issue – rather, it is one of the foremost challenges in modern analytical science, and as been described as such by Royce Murray, in a recent editorial in the American Chemical Society journal Analytical Chemistry:

'A Grand Challenge posed for analytical chemistry is to develop a capability for sampling and monitoring air, water and soil much more extensively and frequently than is now possible. Such goals will require improvements in sampling methodology and in techniques for remote measurements, as well as approaches that greatly lower per-sample and per-measurement costs'.

Tacklingthe core issues identified in this visionary statement is at the heart of what we want to achieve through this project.

The *NAPES* project groups different european universities and vompanies, each of them with different capabilities and expertise. The partners collaborating in *NAPES* are:

- Dublin City University
- Eindhoven University of Technology
- Macromolecules and Microsystems in Biology and Medicine, Institute Curie
- TE Laboratories Ltd
- Williams Industrial Services
- University of Milan
- Aquila Bioscience
- CIC MicroGune Microtechnologies Cooperative Centre

Each partner is mostly focused on one main objective, summarized as follow:

1. **Deliver 'revolutionary' advances in sample handling based on molecular switches and nano-scaled control of polymer structures in microfluidics.**
   A major theme is the use of biomimetic stimulus-responsive polymers/gels to control many advanced microfluidic functions, such as fluid movement (valving, pumping, capillary forces), binding activity (molecular guest uptake and release), and even dynamic control of micro/nano-scaled channel features and dimensions. Full integration of effective polymer actuators within the microfluidic chip for controlling fluid handing would clearly therefore represent the single biggest advance in the technology by which environmental monitoring is performed.

2. **Develop innovative sampling strategies.**
   Sampling is an issue that is often neglected in environmental chemical sensing research, and yet the entire analytical process depends on obtaining a representative sample. For a target like Escherichia coli bacteria (E. coli), the detection limits are extremely low, and the sampling strategy must take this into account. Large sample volumes must be processed through filtering and pre-concentration units, prior to sampling by the microfluidic system for subsequent analysis. The stages for the pre-concentration aree: initial particulate suspension removal, reverse osmosis, tubular filtration and microfluidic magnetic bead-based selective extraction, **Figure 1.3**. The detection of E. coli will be achieved using a detector based on materials that are iso-refractive with water. Modifying the material surface with appropriate receptor binding sites provides a degree of selectivity for this process, enabling very sensitive and selective detection of preselected target species via a so-called 'Reactive Phantom Interface' (RPI), **Figure 1.3**.

3. **Integrate highly innovative analyte extraction and detection schemes**.
   The availability of low cost and sophisticated fluid handling coupled with innovative sampling strategies paves the way for the implementation of more advanced detection schemes that will enable highly sensitive and selective measurements. The RPI approach will be initially implemented with more accessible yet environmentally important targets such as surfactants and oils: very sensitive surfactant detection can be successfully achieved using this detector due to the self-assembly of surfactants onto the detector interface, **Figure 1.3**.

4. **Integrate components into functioning prototypes based on existing platforms.**
   For example, prototype components integrating new materials and photo-polymer actuators will be further characterized in complete functioning chemical analysers. Existing microfluidic components based on conventional valves and pumps dominate the component costs of these existing platforms: their replacement by much lower cost, fully integrated polymer actuators will have a dramatic impact on the overall cost base.

5. **Demonstrate the utility of combinations of these components in field deployments.**
   Components that show promise under laboratory assessment will be brought through to field trials at waste water plants, and river/lake/industrial sites at which parallel trials are already ongoing. This will enable the performance of these new components incorporated within the prototype platform to be further assessed under real conditions, and against best available technologies. Such benchmarking tests will facilitate fast-tracking of these improvements to commercialization through the generation of specification sheets, marketing data and reference to exemplar deployments.

6. **Fully exploit instances of improved platform functionality arising from NAPES.** Building on the achievement of the previous objectives, the overall goal is to fully exploit all opportunities arising from NAPES with a particular emphasis on promoting advantages arising from driving down the cost of technologies required for effective remote monitoring of water quality. The vision of widely distributed sensor networks for environmental monitoring is achievable provided cost issues are addressed. If successful, the project outputs will have profound impact across the entire area of remote sensing, opening up entirely new ways to perform complex analytical tasks using low-cost, reliable, autonomous devices.

The work presented in this thesis relates mostly Oobjective 3, in particular the development of new substrates and strategies to optically detect surfactants and oils in water samples. In this part of the project innovative micro-structured materials generated from a new fluoropolymer substrate with refractive index matching that of water will be realized. These materials will be formed as porous membranes or as beads that will be the building blocks of a new kind of in micro-chromatography column.

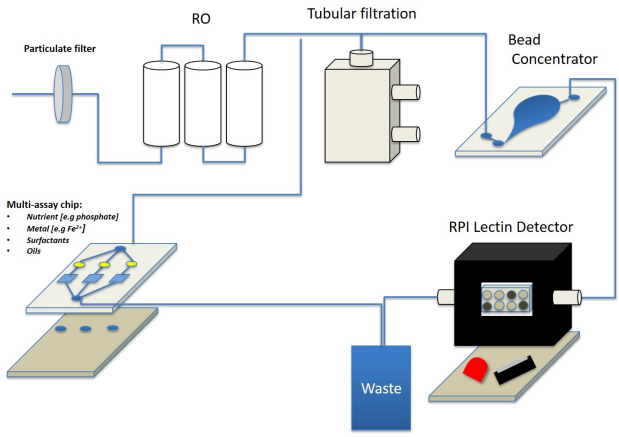

Figure 1.3: Schematic representation of the components that are used to build the autonomous device. After a particulate filter, multiple steps of pre-concentration are placed in series, including reverse osmosis, tubular filtration and bead concentration, before the sample reaches the RPI detector. For small molecule detection, the water sample is directed into a multi-assay chip after the reverse osmosis step.

Chapter 2:
Materials index-matched to water for optical sensing

In this chapter, multiple materials that matches the refractive index of water are presented and their application to biosensing devices is discussed. Two different fluorinated plastics, *Hyflon AD*® and *Fomblin MD*® , both products of *Solvay Specialty Polymers*, have been used during this work to realize porous substrates for pollutants detection. In previous works, these fluoropolymers have been employed in the shape of right angle prism and nano-particles applied io the field of label-free biosensors, as explained in Sections 2.2 and 2.3. Another low reflectivity substrate, not made from a fluorinated compound, is presented in Section 2.4, for the detection of molecular interaction.

In Section 2.5 and 2.6 I present new applications of fluorinated plastics. New materials were carried out as porous substrates for the first time in this work: micro-porous membranes (2.5) and a chromatography column formed by microbeads (2.6). These porous materials have been developed because they have more surface area for adsorption and detection. Moreover, they are more suited to integration into an autonomous, on-line system for the detection of small pollutant molecules present in very large water volumes ($\gg$ hundreds of liters).

2.1 Fluorinated polymers

Fluorinated polymers are composed of a carbon backbone, in some cases including branching, substituted mostly or only with fluorine, the element with the smallest dipole moment per unit volume induced by the electromagnetic field of visible light [12]. Consequently, fluoropolymers usually possess an extraordinarily low refractive index. Moreover, the highly polar C-F bond, which is abundant in fluoropolymers, is stronger than the C-H, typical of hydrocarbons. This leads to excellent chemical and thermal resistance of the fluorinated compounds relative to more common hydrogen-substituted carbon-based polymers. The weak intermolecular interactions associated with the low polarizability of fluorine impart to perfluopolymers some unique properties including of high surface tension in liquid phase, low friction coefficient and reduced adhesion to other surfaces [13]. This is why fluorinated oils and polymers are widely used in many applications: as insulating coatings for electronics, thanks to their dielectric properties; as non-stick coatings for cookware, because of their oleophobicity and lipophobicity; and as anti-wetting coatings for membranes, solar cell and rainwear, because of their high hydrophobicity. In particular, polytetrafluoroethylene (PTFE) is the most widely known and used fluoropolymer for such applications. PTFE is a completely non polar polymer with high crystallinity, showing very poor solubility in any solvent and high temperature of processing. To overcome this problem, the incorporation of some special comonomer results in copolymers with an amorphous structure and a better solubility and processability [14].

In this work, I report how it is possible to use special kinds of fluoropolymer materials for optical sensing purposes, exploiting their low refractive index. Here I describe in particular two different fluoropolymers, *Hyflon AD*® and *Fomblin MD*® , that have been utilized in this work to develop new kinds of porous substrates. These materials have been used previously in the form of nano-colloids and a right angle prism to study bio-molecular interactions. To do this, the surfaces of the fluorinated substrates were functionalized in order enable binding specific molecular compounds from solution. This in turn enabled the realization of a novel class of optical biosensors, based on such phantom materials [15].

Hyflon AD®, **Figure 2.1a**, is the commercial name of a copolymer of tetrafluoroethylene (TFE) and 2,2,4-trifluoro-5- trifluoromethoxy-1,3-dioxole (TTD): TTD molecules can disrupt the typical crystalline structure of TFE, making the plastic completely or fully amorphous. Depending on the quantity of TTD molecule used for co-polymerization, different categories of *Hyflon* result: *AD 60*®, contains 60mol% of TTD molecule and *AD 40*®, contains the 40mol% of TTD. The presence of this non-fluorinated moiety, makes the polymer soluble in some fluorinated solvents. The refractive indices of these two different plastics are 1.328 and 1.331, respectivel [16]

Fomblin MD®, **Figure 2.1b**, is a class of polymer modifiers that improve the performance of polymeric materials: it is manufactured through a photo-oxidation process, which leads to perfluoropolyether (PFPE) macromer having a range of molecular weights and reactive groups [17]. Usually it finds use in the following technologies and sectors: elastomers, rubbers, coatings, membranes and ultraviolet (UV) curing. This polymer is selected for its low refractive index (1.313) and because it is UVcurable. This means that, using the proper photo initiator, cross linking of the polymer is possible. A photo initiator is usually a molecule that absorbs a UV photon, becomes excited to a short-lived singlet state, then relaxes to a more stable triplet state, which in this case abstracts a hydrogen atom from the polymer backbone containing labile H, generating a polymer macro radical. This then becomes the active site for the surface grafting of a

reactive monomer which is chemically linked to the polymer structure [18].The polymer used in this work is commercially available as *Fomblin MD40*®.

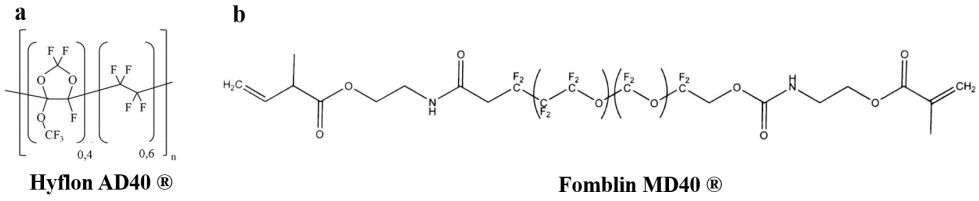

Figure 2.1: Chemical formulae of the two polymers used in this work: a) Hyflon AD® and b) Fomblin MD®

The two different fluorinated polymers used in this work have been reported as substrates for new kinds of biosensors, called label-free because the measurement does not require the labeling of the analytes with colored, fluorescent, or radioactive moieties. In particular, in previous applications, they were produced in the forms of nano-particles and a right angle prism.

The optical signal of the biosensing systems presented in this chapter can be directly converted into absolute numbers of molecules on the surface of the respective fluorinated substrate by means of suitable optical models that are presented in *Chapter 3*. The principle is that the light scattered by these materials, in the case of the nanoparticles, or the reflected light, in the case of the prism, increases significantly, when sub-nanometer layers of molecules are formed on their surfaces. These approaches enable the development of extremely simple, though highly sensitive, label-free biosensing devices. The contents of Sections 2.2 and 2.3 are the matters of a review paper, *Invisible Fluorinated Materials for Optical Sensing*, Reference Module in Materials Science and Materials Engineering, Elsevier.

2.2 Nano Particles

The first studies of molecular recognition for this thesis were carried out with low refractive index nano-colloids, the so called *Phantom nano-Particles* (PnP). These particles were made from two different fluorinated polymers. In this approach, the surfaces of nano-spheres suspended in solution provided the support for molecular receptors (probes), which then captured specific ligands (targets) present in the solution. Because of their low refractive indices, the colloids are barely detectable when dispersed in water. In contrast, most organic molecules have much higher refractive indices than does water, typically around 1.4-1.7, [19]. As a result, the formation of molecular complexes between the surface-immobilized probes and the targets induced a measurable increment of scattered light by raising the effective index of refraction of the composite layer. In practice, the scattered light was due to the formation of a spherical shell with refractive index higher than both the inner (particle) and outer medium (solution). The intensity of scattered light was analyzed using a theoretical optical model, which will be explained in detail in *Chapter 3*, enabling measurement of the number of molecules adhering to the particle surfaces.

This so-called *Dispersed Nano Scattered* method, DNS, [20] was exploited to measure a number of different molecular interactions. Two kinds of nanoparticles were used in this work: PP20 and PP40 nano-spheres, having a radius of about 20 nm and 40 nm, respectively. Both were provided by *Solvay-Solexis* (now *Solvay Specialty Polymers*, Bollate, Italy). PP20 were made of fluorinated polymer that forms an amorphous glass and had a refractive index of 1.3284. PP40 were made of rubbery fluoroelastomer and had a refractive index of 1.3248. As expected, the particles were rather hydrophobic. Nevertheless, they were stable against aggregation, because of the electrostatic repulsion provided by a small amount of negative charges on their surfaces. For these reasons, surfactants represent a suitable class of molecules to test the optical response of the PnPs. **Figure 2.2** shows the appearance of a cuvette containing 0.1% vol/vol of PP40 in water. A 5 mW HeNe laser beam passing through the cuvette was barely visible in the case of uncoated particles (Figure 2.2A). The addition of small amounts of surfactant, about 100 nmol of dodecyl -maltoside (D β M), induced a further decrease of the light scattering intensity (Figure 2.2B). Then, a pronounced increase was observed for further additions (Figure 2.2C), up to the point of complete coverage of the particles. The condition of extremely weak scattering shown in (Figure 2.2B) was due to perfect optical matching between the solution and the effective refractive index of the coated particle, obtained as a he appropriately weighted average of the refractive indices of particle and surfactant.

Figure 2.3A shows the behavior of the intensity of scattered light measured for PP20 and PP40 particles for increasing concentrations of D β M. The initial minimum was observed in both systems, although it was more pronounced for the PP40. Additionally, both systems reached a plateau of scattered light at high concentration of D β M, indicating complete coverage of the particle surface. The D β M concentration and the signal amplitude corresponding to the minimum and the plateau, provide important parameters for the characterization of these systems. The data were fit to curves representing a model combining the optical response with simple Langmuir adsorption, enabling extraction of the refractive index of the coating layer and the total particle surface available for adsorption, as well as the equilibrium constant for adsorption. The probe-target binding occurring on the surfaces of the particles provided an increase in the scattered light. In this way, the equilibrium constant of the interaction was determined from the shape of the measured scattered intensity as a function of the target concentration in the cuvette. **Figure 2.3B** shows an example of these strategies of surface functionalization and

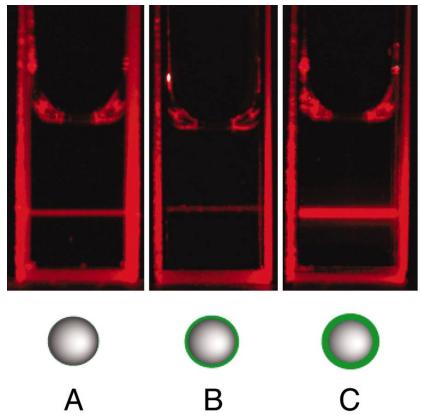

Figure 2.2: Light scattered by phantom nanoparticles. Image of a 1-cm cuvette containing a dispersion of PP40 acquired in the case of (A) bare nanoparticles, (B) adsorption of a small amount of surfactant resulting in perfect index matching of particles with water and (C) complete coverage of particle surfaces with surfactant.

of the measurement. PP40 particles were first coated with a surfactant chemically modified in order to expose a tri-peptide with the sequence lysine-alanine-alanine. Then, the antibiotic vancomycin (Van) was added to the solution and its binding with the peptide was characterized by the increase in scattered light. The antibiotic action of Van relies on the binding to the peptidoglycans forming the cell walls of Gram-positive bacteria. Van prevents the cross-linking of the long polymers that normally form the bacterial cell wall by binding to their D-alanine-D-alanine terminals, made by the dextro (D) enantiomer form of the common laevo (L) alanine amino acid present in proteins. To model the bacterial cell wall, the PP40 particles were coated with a mixture of D β M and the surfactant carrying the tri-peptide.

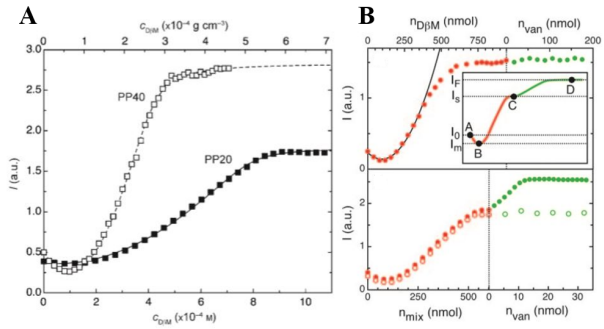

Figure 2.3: A) Intensity of scattered light as a function of D β M concentration. Increasing amounts of D β M were added to a cuvette containing a dispersion of PP20 (full symbols) or PP40 (open symbols). Lines are best fits obtained by a model combining the optical response with Langmuir adsorption. B) Measurements of the interactions between Van and lysine-alanine-alanine peptides. Top: Intensity of scattered light measured as a function of the amount of D β M and Van. The black line represents a parabolic fit to the lowest intensity data. Inset: Schematic representation of the scattered intensity as a function of the concentration of added surfactant (red) and Van (green). Bottom: Intensity of scattered light measured as a function of the amount of 98.2/1.8 (mol ratio) mixtures of D β M and KLALA (open red dots) or KDADA-1 (full red dots), and of Van (green).

The results described above demonstrate the capabilities of the DPS technique to measure subtle changes in the interactions between molecular partners. The high sen-

sitivity of the method enabled the detection of the binding of compounds with different masses, down to small molecules well below 1 kDa. Such sensitivity is ultimately provided by the extremely large total surface area within the particle suspension. The flexibility of this method was confirmed by studying a variety of interactions, including antibiotics–peptides, protein A–antibody and enzyme–substrate. Moreover, alternative strategies were proposed to functionalize the particle surface. Different probes were immobilized on avidin–coated nanoparticles and a novel approach based on suitably designed photo-polymerizable diacetylenic compounds was proposed [21] [20] [22] [23] [24].

2.3 Planar surface: fluoropolymer prism

One phenomenon that can thwart the DPS method is the aggregation of the nano-colloids, which can take place when the target compounds have multiple binding sites, or when they tend to form oligomers. In such cases, the probe-target interaction may yield to the formation of bridges between the surfaces of different nanoparticles. In order to overcome the limitation of this technique, a solid and stable support is preferable relative to a dispersed system. Arguably, the simplest way to implement the phantom detection principle on a fixed support is to use a slide or prism made of the same transparent, fluorinated material with refractive index close to that of water. This was the solution adopted in the *Reflective Phantom Interface* method (RPI) [15] [25] [26]. A right-angle prism was realized using the amorphous fluorinated plastic Hyflon AD® . In contrast to the DPS technique, the RPI optical sensing signal was provided by the intensity of light reflected by the extended planar interface separating the sample solution and the solid substrate. The prism, when immersed in water, was barely visible because of the matching of the refractive indices. In practice, its clean surface reflected about 0.001% of the intensity of the illuminating light. Under these conditions, the formation at the interface of a thin layer of material with different refractive index provided a relatively large increase in reflected light intensity. The link between the number of molecules adsorbed onto the plastic surface and the optical signal will be investigated more deeply in Section 3.1.

The planar surface format offered the advantage of enabling multiplex measurement by immobilizing different probes in different spots and measuring the binding by acquiring a sequence of images of the light reflected by the surface. In each spot, the brightness of the image pixels indicated the number of molecules (presuming their index of refraction was known) on that surface region. The measuring system employed for the experiments was extremely simple. The collimated light of a LED was used to illuminate the sensing surface. The reflected light was selected by spatial filtering and imaged on a CCD or CMOS camera. A schematic representation of the system is shown in **Figure 2.4A**. Spots of different receptors probes (e.g. antibodies) were visualized as shown in **Figure 2.4B**. The number of molecules adhering to the RPI sensing surface was directly obtained from the local brightness of the image. A suitable optical model was developed using the Fresnel equations for thin film reflection which will be explained in Section 3.1.

In general, the stable immobilization of molecular probes on the surfaces of fluorinated materials represents a challenging task, because fluorinated plastics are chemically inert to many common reagents. The functionalization of the planar RPI sensing surface was achieved by means of a suitably designed multi-functional copolymer, namely copoly(DMA-MAPS-NAS) [27], which is currently produced and distributed by Lucidant Polymers, LLC (USA). The copolymer was deposited on the prism by dip-coating, after plasma treatment to activate the surface. The copoly(DMA- MAPS-NAS) forms a thin ($\sim$ 10 nm) and highly swollen film in wet conditions, therefore providing a rather small value of refractive index (n $\sim$ 1.36). The hydrophilic nature of the copolymer yields remarkably low non-specific binding, in presence of highly complex matrices, such as cell culture media, blood, milk and vegetable extracts [28] [29] [30].

The binding of specific target molecules to the immobilized probes was detected and characterized by analyzing the increase of reflected light intensity relative to the initial brightness of the spots. The spot brightness was converted into the normalized surface density and the initial value of each spot was subtracted, thereby yielding the increase in surface density. **Figure 2.4C** reports $\Delta\sigma/\sigma_0$, that is the normalized increment of adsorbed

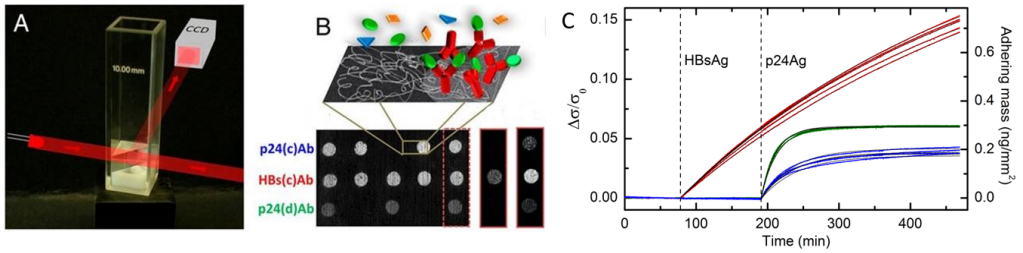

Figure 2.4: Optical set-up and sensing surface of the RPI technique. (A) The light emitted by a LED is reflected by the diagonal prism of Hyflon AD® and imaged on a CCD camera. The prism is held by a plastic support that contains a stirring magnetic bar. (B) Schematic representation of the functionalized prism surface showing the copolymer (gray threads), the immobilized antibodies (red) and the target molecules (green) and a RPI image of the surface spotted with antibodies targeting proteins HBsAg and p24Ag acquired before the addition of the antigens in solution. (C) Image of the brightness increment on the three spots on the right-hand side of C measured 110 min after the addition of 50 ng/mL HBsAg in solution

surface density, normalized to the corresponding absolute value of surface density on the spots shown in **Figure 2.4B**, after the addition of the corresponding hepatitis B (HBsAg) and HIV (p24Ag) antigens in buffer solution. The binding curves were measured in real-time. This enabled to extract both the equilibrium and the kinetic properties of each interaction. RPI detection was applied to different interactions including antigen-antibody, antibody-antibody, antibody-viruses and DNA-DNA.

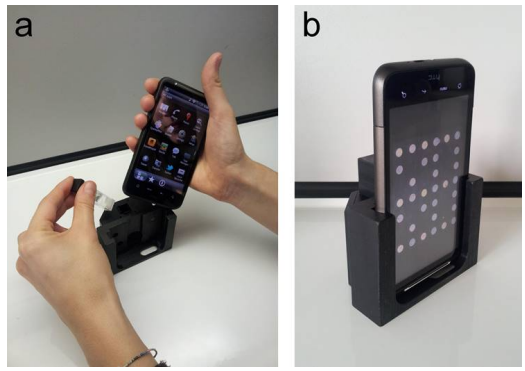

Figure 2.5: Smartphone-based RPI set-up. (a) A plastic cradle containing a few optical elements hosted the smartphone and the measuring cartridge. (b) The smartphone camera acquired RPI images of the sensing surface. Dozens of different spots on the surface were imaged at the same time.

An extremely compact RPI detection device was realized exploiting the electro-optical components and the processing capabilities of a smartphone **Figure 2.5**. A suitably designed cradle containing a few optical elements and a magnetic stirrer enabled use of the flash and the imaging camera of the smartphone to perform highly sensitive RPI measurements on blood markers of infectious diseases [25].

2.4 Planar surface: anti-reflective glass

Low surface reflectivity can be achieved also by means of a much more common material: a special glass slide with a coating of silicon dioxide that acts as an anti-reflective layer [29]. The fabrication of dielectric coatings on glass is a widely employed procedure for many applications and anti-reflective layers are commonly deposited on optical components, although with less stringent requirements than those described here. Moreover, a large number of consolidated approaches is available to treat and functionalize the silicon dioxide surface. Development of commercial products based on this anti-reflective glass substrate are currently provided by *Proxentia s.r.l.* (Italy).

Wedge-like glass chips (F2 optical glass, Schott) having a refractive index n=1.620, were coated with a thin layer of SiO_2, which provides a refractive index n=1.473 at 595 nm. With this combination of refractive indices and thickness it is possible to achieve the same low value of reflectivity at a water inteface as the fluorinated plastic presented above. This is possible because the wave reflected by the water/SiO_2 interface and the one reflected by the SiO_2/glass interface destructively interfere. In principle, this condition can be obtained for every wavelength, given he appropriate layer's thickness. A schematic representation of the structure of the sensing surface is shown in **Figure 2.6**. In this condition, the adhesion on the surface of small amounts of material (e.g. biomolecules) with refractive index n_2, different from n_s, solution's refractive index, induces a relative increase of reflectivity that can be easily measured and used to estimate the number of molecules adhered to the surface, even if forming sub-nanometer layers, with the same model developed for the fluorinated plastic substrate. Also with this glass substrate the immobilization on the surface was achieved by means of a layer of a few nanometers of copoly(DMA– NAS–MAPS).

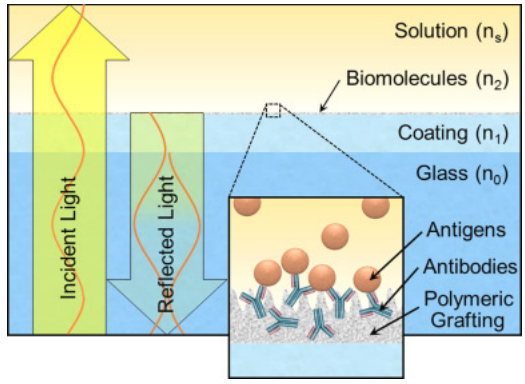

Figure 2.6: Schematic representation of the sensing material. A glass substrate with refractive index n0 was coated with a dielectric material with refractive index n1 and with the copoly (DMA–NAS–MAPS), on which different antibodies were immobilized. The chip was placed in contact with an aqueous solution with refractive index ns, containing different concentrations of target molecules. The intensity of the light reflected by the multi-layer interface depends on the thickness of a thin layer of molecules with average refractive index n2, including the spotted anti- bodies and the target molecules captured by the antibodies. The relative thickness of the layers and wavelengths are shown to scale.

2.5 Novel fluorinated material: micro-porous membrane

Phase inversion is one of the most-used techniques to prepare microporous membranes [31]. It is based on causing a polymeric solution to become unstable, which can be accomplished by the modification of the solution temperature. In this case, phase inversion is achieved by immersing the solution in a non solvent for the polymer. In the literature, this technique is called *Non-solvent Induced Phase Separation* (NIPS). Obviously, the chosen non-solvent must be miscible with the solvent in order to induce phase separation. In the following, I present the first Hyflon AD® membrane samples realized with the NIPS method. I have tested different solvent and non-solvent mixture to obtain, finally, a stable and porous membrane.

2.5.1 Non-solvent Induced Phase Separation (NIPS) method

Solution casting is commonly used to prepare flat sheet membranes [31]. An even film of an appropriate polymer solution is spread across a flat plate with a casting knife. The casting knife consists of a steel blade, resting on two runners, arranged to form a precise gap between the blade and the plate onto which the film is cast. After casting, the solution is put into a coagulation bath containing a non-solvent for the polymer. This technique for making porous membranes was used by Loeb and Sourirajan [31] to produce membranes for water desalinization. This is a special case of a more general class of membrane preparation process, often called the phase separation process, but sometimes called the phase inversion process or the polymer precipitation process. The term *phase separation* describes a process in which a single phase casting solution separates into two phases. In all phase separation processes, a liquid polymer solution is precipitated into two phases: a solid, polymer-rich phase that forms the matrix of the membrane and a liquid, polymer-poor phase that forms the membrane pores. Precipitation of the cast liquid polymer solution to form the anisotropic membrane can be achieved in several ways.

Over the years several approaches have been used to realize the formation of Loeb-Sourirajan (solution precipitation) and other phase inversion membranes. In this method the change in composition of the casting solution as membrane formation takes place can be tracked as a path through the phase diagram. The path starts at a point representing the original casting solution and finishes at a point representing the composition of the final membrane. The casting solution composition moves to the final membrane composition by losing solvent and gaining non-solvent. A typical three-component phase diagram for the components used to prepare Loeb–Sourirajan membranes is shown in **Figure 2.7**.

The corners of the triangle represent the three pure components (polymer, solvent, and non-solvent); points within the triangle represent mixtures of the three components. The diagram has two principal regions: a one-phase region, in which all components are miscible; and a two-phase region, in which the system separates into a solid (polymer-rich) phase and a liquid (polymer-poor) phase. During precipitation of the membrane, the solution loses solvent and gains non-solvent. The casting solution moves from a composition in the one-phase region to a composition in the two-phase region. Although the one-phase region in the phase diagram is thermodynamically continuous, for practical purposes it can be conveniently subdivided into a liquid polymer solution region, a polymer gel region, and a glassy solid polymer region. Thus, in the low-polymer-concentration region, typical of the original casting solution, the compositions are viscous liquids. However, if the concentration of polymer is increased, the viscosity of com-

positions in the one-phase region increases rapidly, reaching such high values that the system can be regarded as a solid gel. The transition between the liquid and gel regions is arbitrary but can be placed at a polymer concentration of 30 to 40 wt%, depending on the used polymer. If the one-phase solution contains more than 90 wt% polymer, the swollen polymer gel may become so rigid that the polymer chains can no longer rotate. The polymer gel then becomes a solid polymer glass. During the precipitation process, the casting solution enters the two-phase region of the phase diagram by crossing the so-called binodal boundary. This brings the casting solution into a metastable two-phase region. Polymer solution compositions in this region are thermodynamically unstable but will not normally precipitate unless well nucleated. The metastable region in the phase diagrams of low-molecular-weight materials is very small, but can be large for high-molecular-weight materials. As more solvent leaves the casting solution and non-solvent enters the solution, the composition crosses into another region of the phase diagram in which a one-phase solution is always thermodynamically unstable. In this region, polymer solutions spontaneously separate into two phases with compositions linked by tie lines. The boundary between the metastable and unstable regions is called the spinodal boundary. Thus, the membrane precipitation process is a series of steps. First, solvent exchange with the precipitation medium occurs. Then, as the composition enters the two-phase region of the phase diagram, phase separation or precipitation begins. The time taken for solvent/non-solvent exchange before precipitation occurs can be measured because the membrane, in general, turns opaque as soon as precipitation begins. Depending on the casting solution composition, the time to first precipitation may be almost instantaneous to as long as 30–60 s. Initially, the polymer phase that separates on precipitation may be a liquid or semi-liquid gel, and the precipitation domains may be able to flow and agglomerate at this point. In the final step of the precipitation process, dissolution of the polymer phase converts the polymer to a relatively solid gel phase, and the membrane structure is fixed. The solid polymer phase forms the matrix of the final membrane, and the liquid solvent–nonsolvent phase forms the pores.

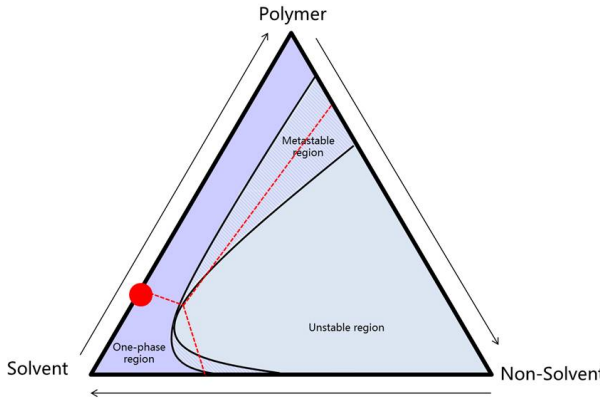

Figure 2.7: Ternary phase diagram. The starting casting solution is represented as the red dot. During the coagulation process, the nascent membrane loses solvent, gaining non-solvent, so the dot moves along the red dashed line. When the system reaches the metastable region, the sample separates into two different phases: one polymer rich, that form the structure of the membrane, and one polymer poor, that forms the pores.

2.5.2 Realization of Hyflon AD® membranes

In the present work porous membranes were prepared from Hyflon AD 40® . This amorphous glassy polymer contains 40 mol% 2,2,4- trifluoromethoxy- 1,3- dioxole (TTD). AD 40® has n=1,331 . In order to produce flat sheet porous membranes the NIPS technique was adopted. HFE 7100® and HFE 7300® (3M) were selected as solvents. These partially fluorinated solvents are non flammable and miscible with alcohols and ketones. The chemical structures of solvents are displayed in **Figure 2.8**. Hyflon AD40® was kindly supplied by *Solvay-Specialty Polymers* and was used without further purification. Flat sheet Hyflon AD40® membranes were prepared as follows: solutions were prepared by dissolving Hyflon AD40® powders in solvent for one day at room temperature. The solutions were ultrasonicated for 30 minutes to eliminate bubbles. An appropriate amount of the solution was poured on a glass plate, immediately cast, then immersed in a bath to induce phase separation. The bath temperature was set to 25° C. Different coagulation baths were used: pure ethanol, a mixture of ethanol/acetone 70/30 v/v and 50/50 v/v. After 15 minutes, the membranes were removed and rinsed in a second bath of pure ethanol and then in de-ionized water several times in order to remove the remaining solvent. The items were then stored in MilliQ water- ethanol 70/30 v/v. Note that to the casting solution was added, in some cases, a non-solvent, Ccyclohexanone, Figure 2.8, in order to accelerate the precipitation of the nascent membrane.

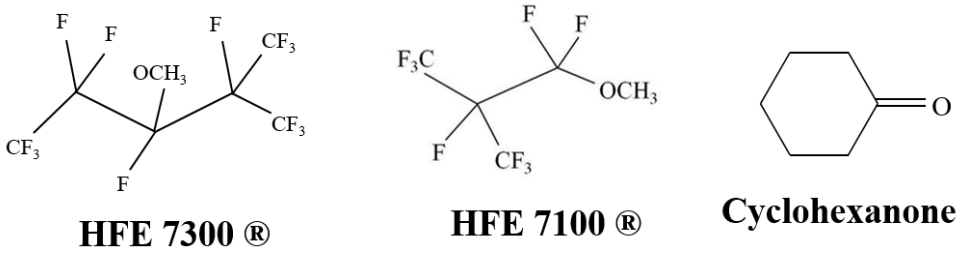

Figure 2.8: Chemical formulae of the two solvents used in this work: HFE 7100 ®, HFE 7300 ® and of the non-solvent, cyclohexanone, used in the casting solution.

The finished membranes were then characterized using classical methods adopted for membrane characterization:

- *Thickness* of the wet membranes was measured with a micrometer.
- *Porosity*: porosity is defined as the volume of the pores divided by the total volume of the membrane. Membranes were weighted after soaking in Isopropyl alcohol (here the wetting fluid) and then dried following the method described in the appendix of ref. [32] . Porosity is calculated according to the following formula:

$$\varepsilon = \frac{\frac{M_w - M_d}{\rho_i}}{\frac{M_w - M_d}{\rho_i} - \frac{M_d}{\rho_h}}$$

where M_w is weight of the wet membrane, M_d is the weight of the dry membrane and $\rho_h = 1,93 g/cm^3$ are the densities of the polymer and $\rho_i = 0,785 g/cm^3$ of isopropyl alcohol. This measurement assumes that all the pores are soaked by the wetting liquid.

- *Scanning Electron Microscopy (SEM)*: A Leo-Zeiss Supra 35 microscope, with a Field Emission Gun (Schottky type) was used to image cross-sections and surfaces of the produced membranes. Prior to testing, the dried samples were broken in liquid nitrogen and sputtered with a thin layer of gold in order to make them conductive.

- *Thermal Gravimetric Analysis (TGA)* was performed using a Perkin Elmer and was used to check the presence of residual solvent in the final items after drying. In this analysis, the loss of weight of the sample is measured as a function of temperature.

- *Pore size distribution and bubble point tests*. Both of these tests are based on measuring nitrogen flow and uptake through a wet membrane as a function of increasing applied pressure, [33]. The bubble point test is based on the fact that, for a given wetting fluid and pore size, the pressure required to force a nitrogen bubble through the pore is inversely proportional to the size of the pore diameter. The relationship is based on Laplace's law, which can be simplified to $P = \frac{2Scos(\theta)}{r}$, where P is the air pressure,S is the wetting liquid surface tension, θ is the contact angle between the wetting liquid and the filter medium and r is the radius of the biggest pore. This formula applies only to cylindrical and straight pores, and so does not take into account any tortuosity inside the membrane, **Figure 2.9A** and **Figure 2.9B**. The wetting liquid must have low surface tension and should fill all the pores of the membrane. The gas starts to flow when its pressure is larger than the surface tension. All the experiments in this work were performed using isopropyl alcohol as wetting fluid. Because this technique is based on gas flow, it is sensitive only to through-pores, not to the blind and closed ones. The measurement is performed till the membrane is completely dry. After this step, the nitrogen permeability can also be tested: from a comparison between the wet and the dry curve, **Figure 2.9C**, it is possible to determinate the mean pore diameter, the filter efficiency and the pore size distribution. These measurement were performed with a $POROLUX^{TM}1000$, product of Porometer NV.

Besides these commonly used techniques, I have developed and performed optical measurements to study the morphology of the novel membranes, as described in *Chapter 6*.

2.5.3 Characterization of Hyflon AD® membranes

In **Tables 2.1** and **2.2** are reported the experimental compositions and the characteristics of the fabricate membranes utilizing two different solvents, HFE7100® and HFE7300®.

Not all fabricated membranes were highly transparent in water: some samples become opaque during the coagulation step and form bubbles, probably because of the low boiling point of the solvents, in particular the samples made with ethanol as the non-solvent. Moreover, from TGA analysis, I learned that the HFE 7100®-derived membranes contain about 6% residual solvent and membranes made using HFE 7300® have an amount of residual solvent from 8,5 %wt to 14,8 %wt. This unusual solvent retention

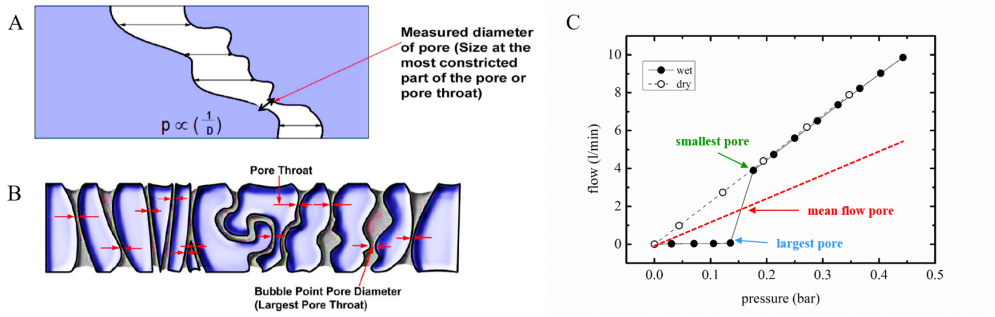

Figure 2.9: How the bubble point and pore distribution tests work. A) The porosimeter technique measures the size of the most constricted part of the pores, hence the diameter obtained from the bubble point test is the largest pore throat, B). C) Dry and wet measurements performed on a cellulose acetate membrane: from the comparison of these tests, it is possible to measure the largest pore size, which is the first to allow nitrogen to flows through the membranes and the smallest pore size. The mean pore size is that calculated at the pressure at which the wet curve and the half-dry curve meet (it corresponds to the pore size at which 50% of the total gas flow is through the pores).

by Hyflon AD® has been previously observed [34] [35] . The presence of the solvent inside membranes gives them an unstable structure that collapses over time. To overcome this problem, I perform a two-step coagulation for the Samples 12-13-14-15-16, and Samples 25-26-27-28. In these cases, the first coagulation bath was made of a 50/50 vol. mixture of acetone and ethanol, then a second coagulation process using pure ethanol was carried out for 15 minutes. Due to this procedure, the residual solvent decreases in all samples, as seen in **Figure 2.10**. A more drastic decrease in solvent retention is observed for HFE7100® samples, in particular the ones realized with non-solvent in the casting solution, 13-15-16. The two-step coagulation is a good technique to overcome the problem of residual solvent that confers an unstable structure on the membrane.

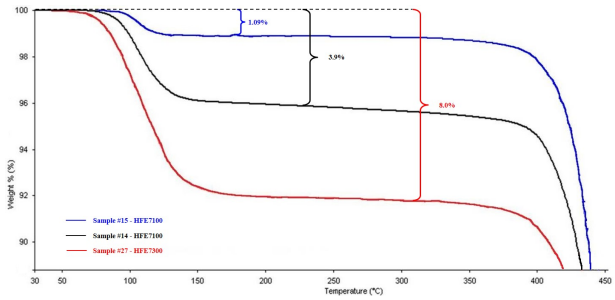

Figure 2.10: Results of the TGA analysis of three different Hyflon AD® membranes. This plot represents the percent loss in weight of the membrane as it is heated.

Concerning porosity, I observed that membranes realized with the mixed coagulation bath are more open and porous, in particular those realized with HFE7100®, 13-15-16. I do not see the same drastic difference for the HFE7300®, 21-22-23-24-27-28 samples. In both cases, the presence of the non-solvent, cyclohexanone, appeared to open the membrane structure, increasing the porosity slightly. For all these reasons, I found that the best casting solution composition uses HFE7100® as solvent with 5% of cyclohexanone, and the best coagulation bath composition is a mixture in equal parts of ethanol and acetone.

Unfortunately, HFE7100® has a low boiling point: this leads to rapid evaporation

during the casting process that generates bubbles, giving the membrane an inhomogenous morphology. To solve this problem, I cooled the casting plate with dry ice to a temperature of 10° C prior to the casting step (Samples 14-15-16). As expected, with this procedure the membranes no longer include bubbles. Despite their high porosity, these membranes have pores that intersect the upper surfaces closed, **Figure 2.13**. This is due to the rapid demixing process that occurs at the solution front that forms a skin layer.

To open the pores at the surface I exposed the membrane samples to chemical attack by placing them in a mixture of HFE7100®/ethanol 20/80% vol. for 15 minutes. Due to this chemical attack, the closed surface became porous, as seen in **Figure 2.14**. Sample prepared with this chemical procedure are more appropriate for use in a micro-fluidic chip because fluid can flow through them.

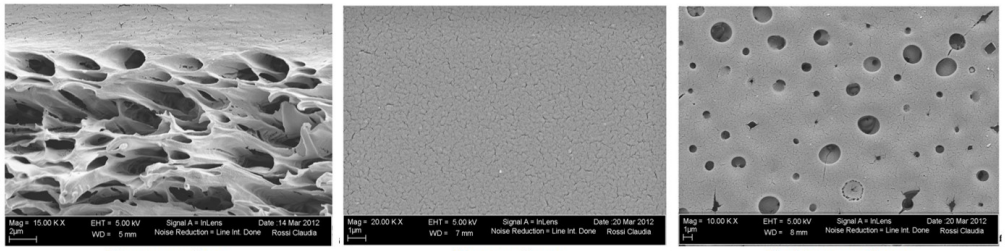

Figure 2.11: SEM images of Sample 2 realized with HFE 7300

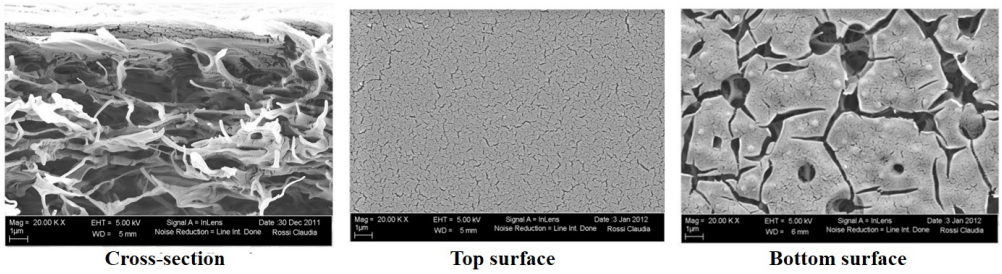

Figure 2.12: SEM images of sSample 13 realized with HFE 7100

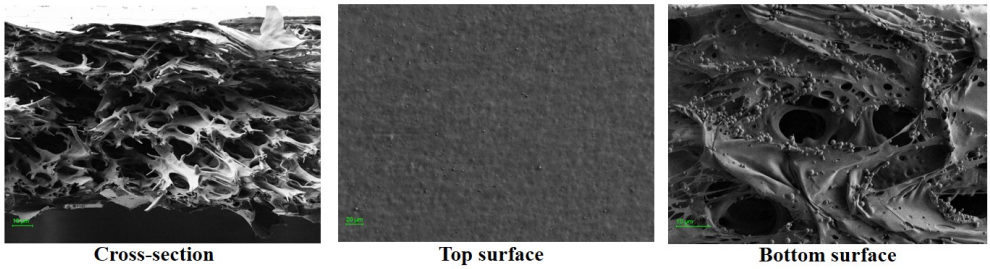

Figure 2.13: SEM images of Sample 15 realized with HFE 7100

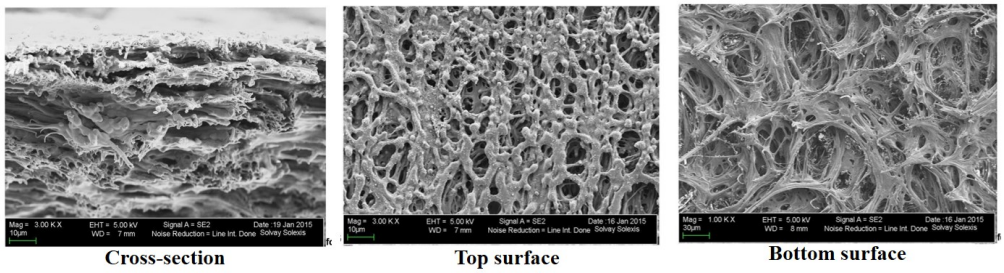

Figure 2.14: SEM images of of Sample 16 realized with HFE 7100

Table 2.1: Characteristics of the membranes realized with solvent HFE7100®

sample number	%wt polymer	%wt non-solvent	coagulation bath % vol	membrane thickness (μm)	% porosity
1	20	0	ethanol	43	64
2	20	0	ethanol	89	59
3	20	0	ethanol	33	57
4	17	0	ethanol	60	67
5	17	0	ethanol	28	45
6	14	0	ethanol	22	63
7	14	0	ethanol	34	28
8	15	0	ethanol	40	50
9	12	0	ethanol	21	40
10	12	2	ethanol	20	37
11	14	2	ethanol	25	27
12	18	0	50-50	61	70
13	18	5	50-50	120	76
14	16	0	50-50	65	66
15	15	5	50-50	91	74
16	15	5	50-50	110	73

Here compositions of casting solution and coagulation bath used to produce membranes samples are reported. Thicknesses and porosity were measurated as described in 2.5.2.

Table 2.2: Samples characteristics of the membranes realized with solvent HFE7300®

sample number	**%wt polymer**	**%wt non-solvent**	**coagulation bath % vol**	**membrane thickness (μm)**	**% porosity**
17	13	0	ethanol	36	24
18	13	0	30-70	37	56
19	14	0	ethanol	35	36
20	14	0	30-70	86	70
21	14	2	ethanol	43	47
22	14	2	30-70	45	34
23	14	4	ethanol	33	50
24	14	6	ethanol	25	28
25	13	0	50-50	54	53
26	16	0	50-50	45	52
27	15	5	50-50	61	64
28	15	5	50-50	66	59

Compositions of casting solution and coagulation bath used to produce membranes samples are reported. Thicknesses and porosity were measurated as described in 2.5.2

2.6 Novel fluorinated material: micro-beads

The term chromatography includes multiple distinct techniques, that are applied to mixtures of separable compounds. This technique was first used in 1906 by Michail Cvet: he separated chlorophyll through clay and petroleum ether, observing different colored bands on the column. Nowadays the color difference is rarely used; the methods used are often more complex. The mixture is dissolved in a fluid, called the mobile phase, which carries it through a structure holding another material, called the stationary phase. The various constituents of the mixture travel at different speeds, causing them to separate. The liquid that comes out of the column is called eluate. The eluate is analyzed, for instance in the case of adsorption experiments, to detect the substance's quantity as a function of time [36]. In the most general situation, to know the nature of the eluates, is necessary to analyze them by mass spectroscopy.

The innovative idea presented here is the realization of a new type of chromatographic analysis column composed of micro particles having the same refractive index as water: in this way surfactant detection could be done directly inside the column, as Cvet did in his experiment, but without the use of colored substances. Instead, an optical scattering signal that changes due to surfactants' presence in the flowing water will be monitored.

To realize this chromatography column, it is necessary to have small particles, roughly hundreds of nanometers in radius, inside a glass cylinder. They will form the stationary phase in the column. In this work, I produced such colloids using a particular instrument (an emulsifier from *SPG TECHNOLOGY*), which can generate low polydispersity emulsions [37]. I also performed tests with micro-fluidic techniques to produce monodisperse droplets. In order to obtain the best substrate with which to optically study molecular adsorption, the beads that form the column must satisfy several conditions: i) they should not be monodisperse, to avoid optical complications, such as diffraction or structure-related features that can complicate the optical analysis, ii) they should not be extremely polydisperse, to avoid liquid flow problems whitin the column (such as percolation or formation of preferential flowchannels). The best situation is low polydispersity microparticles, that also enable a improved optical modeling of the porous substrate.

As mentioned previously, this emulsion is made of an iso-refractive to water elastomer, Fomblin MD 40®, so it will be transparent when in water. The first step is to find the best procedure and conditions to realize micro droplets. Once this emulsion is obtained, I proceed with an UV-polymerization to crosslink the particles; finally, they will be injected into a cylindrical or square capillary tube to form the chromatography column. The creation of a chromatography capillary tube could facilitate the study of system kinetics: by inducing a flow between the ends of the tube using a specially designed mechanism, real-time direct detection becomes possible. While the surfactants flow through the filled capillary tube, the profile along the column of the scattered signal will change: this could enable the detection of molecules as they adsorb on the stationary phase [38].

2.6.1 Emulsion

An emulsion is a mixture of two or more liquids that are normally immiscible. Emulsions are part of a more general class of two-phase systems. In an emulsion, one liquid (the dispersed phase) is dispersed in the other (the continuous phase). Examples of emulsions include vinaigrettes, milk, mayonnaise, and some cutting fluids for metal

working. Common emulsions are inherently unstable and, thus, do not tend to form spontaneously. Energy input – through shaking, stirring, homogenizing, or exposure to ultrasound – is needed to form an emulsion. Over time, emulsions tend to revert to the stable state of the phases comprising the emulsion. This instability is due to hydrophobic force and entropy that drive the droplets to coalesce. To avoid this problem, normally, an emulsifier is added to the solution. The main characteristic of an emulsifier is miscibility with one of the two liquids as well as spontaneous segregation place at the liquid-liquid interface, for instance at a water/oil (W/O) interface, stabilizing the interface and lowering its surface energy. For these reasons, most widespread emulsifier are surfactants, proteins and nanoparticles (Pickering emulsions).

There are different techniques to realize emulsions, each with different advantages and disadvantages. In literature, the two most common techniques used for emulsion production are membrane emulsification and microfluidic. In the following, I discuss both procedures.

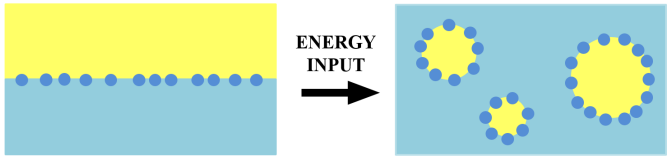

Figure 2.15: Schematic representation of making an emulsion

2.6.2 Membrane method to produce emulsions

Membrane emulsification is a simple method that has received increasing attention over the last 10 years, with potential applications in many fields [39]. The process of membrane emulsification is shown in **Figure 2.16A**. The dispersed phase is forced through the pores of a porous membrane, while a continuous phase flows along the membrane surface. Droplets grow at pore outlets until, upon reaching a certain size, they detach. This size of detachment is determined by the balance between the drag force on the droplet from the flowing continuous phase, the buoyancy of the droplet, the interfacial tension forces and the driving pressure. The droplet at a pore tends to form a spherical shape under the action of interfacial tension. The final droplet size and size distribution are not only determined by the pore size and size distribution of the membrane, but also by the degree of coalescence, both at the membrane surface and in the bulk solution. Multiple parameters can affect the characteristics of the resulting emulsion, e.g. polydispersity and average pore size, membrane type, average porosity, crossflow velocity, transmembrane pressure and choice of emulsifier.

In this work, I used the Fast-mini kit of *SPG Technologies* for emulsion production [40]. I chose this specific method because it generates quite monodisperse droplets (less than 12%) of uniform size quickly and it is also possible to choose the average size of the droplets by selecting the appropriate membrane. Moreover, it is also possible to produce inverted emulsions (water in oil, W/O) and multi-emulsions (O/W/O or W/O/W). But the most important characteristic is that this instrument functions at high pressure, enabling the passage of viscous liquids, such as Fomblin MD 40®, through the pores. A photograph of this instrument is seen in **Figure 2.16B**. The system incorporates a tubular microfiltration membrane, a pump, a feed vessel and a pressurized (N_2) oil container.

The oil phase is pumped under gas pressure through the pores of the membrane into the aqueous continuous phase, which flows across the center of the membrane.

To test the instrument, I prepared an emulsion of soybean oil in water, stabilized by 8%vol of sodium dodecyl sulfate (SDS) surfactants, using a membrane average pore diameter of 3 μm. **Figure 2.16** shows the resulting emulsion: the droplets have a mean diameter of 11 μm, 4 times larger than the membrane pore diameter, as expected based on previous work [41].

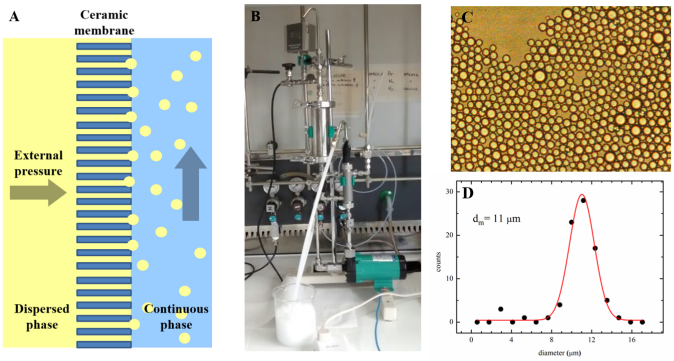

Figure 2.16: Membrane emulsification method. A) Sketch of how emulsification occurs with the membrane method. B) Experimental apparatus of SPG Technology for the realization of emulsions. On the right soybean oil in water emulsion: C) microscope images of a soy-beam oil emulsion in water, stabilized with SDS. D) Histogram of the sizes of the droplets present in Panel C.

I performed various emulsification tests with the fluorinated oil using the experimental conditions described in Figure 2.17. The resulting droplets, 2.17 have a quite wide poly-dispersity, probably due to the high emulsification pressures required by the high viscosity of Fomblin MD 40®.

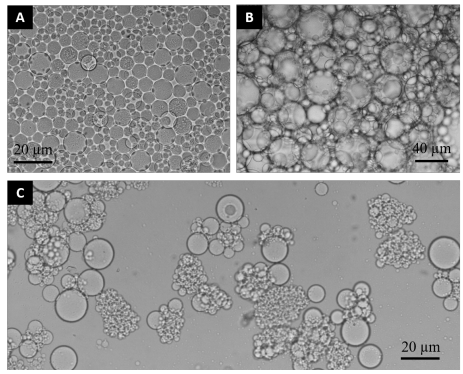

Figure 2.17: Micro-droplets obtained using the membrane method emulsification. The production parameters are: A) membrane pore size 0.3 μm, emulsification pressure 109 kPa, SDS concentration 1%wt; B) membrane pore size 10.1 μm, emulsification pressure 11 kPa, SDS concentration 1%wt; C) membrane pore size 0.3 μm, emulsification pressure 190 kPa, SDS concentration 0.5%wt. It is evident that the samples are not mono-dispersed.

2.6.3 Microfluidic method to produce emulsions

Microfluidic devices offer an alternate and versatile route to produce emulsions. In contrast to bulk emulsification methods, an emulsion in a microfluidic device is made by precisely fabricating one drop at a time. This process results in a highly monodisperse emulsion. However, it is of course a slow and time-consuming method. One of the most attractive features of microfluidic techniques is that they enable the fabrication of double, triple, and even higher order emulsions [42], where the size and number of the encapsulated droplets can be manipulated with unprecedented accuracy.

The principle of drop formation in microfluidic devices can be explained using a water faucet as an example. If we turn on a faucet at a low flow rate, water drips out one drop at a time. The drop size is a result of the balance between the surface forces of the dangling drop and gravity, and therefore depends on the surface tension of the fluid and the size of the faucet. Since both the surface tension and the faucet size are constant, all the drops emerging from a dripping faucet exhibit a narrow size distribution. However, if we increase the flow rate through the faucet, a water stream, or jet is formed. Although the jet eventually breaks up into drops too, these drops have a larger range of sizes. The same principle can be employed in microfluidic channels that have sizes in the range of tens of micrometers. The main difference between drop formation from a faucet and in microfluidic devices is that in the former case drops are formed in air, whereas in the latter case drops are formed in another immiscible liquid.

There are three different geometries to produce emulsions with the microfluidics: coaxial capillaries, T-junctions (TJ) and flow focusing (FF).

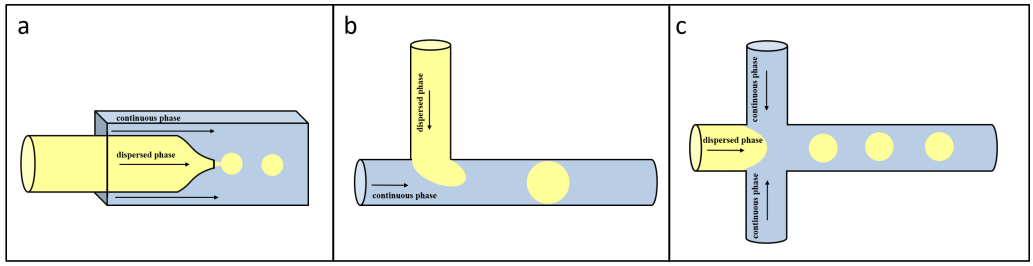

Figure 2.18: Different microfluidic geometries to product emulsions: a) coaxial capillaries, b) t-junction and c) flow focusing.

Capillary microfluidic devices consist of coaxial assemblies of glass capillaries on glass slides, **Figure 2.18a**. In this method, there is a continuous phase flow past the end of a capillary through which the dispersed phase is extruded. Essentially, drops form at the tip on the capillary and then detach when they reach a size where the drag due to the coflowing liquid exceeds the interfacial tension. With this geometry, the sizes of the produced droplets depends of the inner capillary tip diameter, viscosities of the two liquid, and their flow rates. In the literature, droplets from 2 to 200 μm have been realized by controlling these parameters [43]. The T-junction, **Figure 2.18b**, consists of a single straight channel containing the continuous phase and a side channel from which the dispersive phase is injected into the flow as droplets. In this case, the smallest particles that can be realized, have the diameter of the continuous phase channel [44]. The focused flow design, **Figure 2.18c**, consists of a cross junction where the inner fluid or dispersive phase enters through a single channel and the outer fluid, the continuous phase, impinges on the dispersive phase from two channels diametrically opposite one another. This combination of dispersive phase surrounded by continuous phase flows

through the output channel, via the orifice. The orifice is a constriction in the channel used to create a controlled break-up of the dispersive phase into droplets.

Ultimately, the choice of geometry is generally based on the fluids used and the production rates required. A general rule is that for higher flow rates the focused flow geometry and coaxial capillary tend to provide a more stable droplet formation system than the T-junction. The use of flow rate ratio variation as a control parameter for selecting droplet size is a well-established technique due to both its simplicity and robust repeatability. It is notable that an increase in the continuous phase flow rate relative to the dispersive phase flow rate enables the creation of smaller droplets and conversely a decrease in continuous phase flow will lead to an increase in size. The system reaches a natural limit in its variations, as too slow a rate of flow for the inner fluid causes droplet production to stop and to fast a rate causes the dispersive phase to run parallel to the continuous phase with no droplets formed.

A further effect of varying the flow rate ratio is to alter the production frequency. This, however, is not purely dependent on the flow rate ratio, but is also affected by the individual flow rates as well as the fluid parameters themselves. A general rule of thumb for a particular microfluidic device is: the smaller the droplets created the faster the frequency at which tthey can be created. Naturally, there is a lower limit to the size a particular device can achieve and this is based upon the physical size and individual geometry of that particular device. As a general rule, increased total flow rates lead to increased production frequencies for the droplets. However, there is a natural limit to this trend: at sufficiently high flow rates, the fluids flow parallel to one another with no real interaction or droplet formation occurring.

Thanks to a collaboration with dott. Davide Ferraro, of the *Institut Curie, Macromolecules and Microsystems in Biology and Medicine* (MMBM), I have also explored the feasibility of emulsion production in microfluidics, in particular with T-junction and flow focusing geometries. Here I present the preliminary results of this collaboration.

We tested multiple types of microfluidic chips to produce the emulsion:

- Polydimethylsiloxane (PDMS) treated with oxygen plasma to make the inner surfaces hydrophilic, then soaked in a 2%wt solution of SDS in water for one night in order to maintain surface hydrophilicity. Such chips can be customized; here, they were implemented a T-junction (T-J), **Figure 2.19a**.
- Glass chips, commercially produced by *Dolomite Microfluidic*. We had both the T-junction geometry and flow-Ffocusing geometry, **Figure 2.19b** and **Figure 2.19c**.

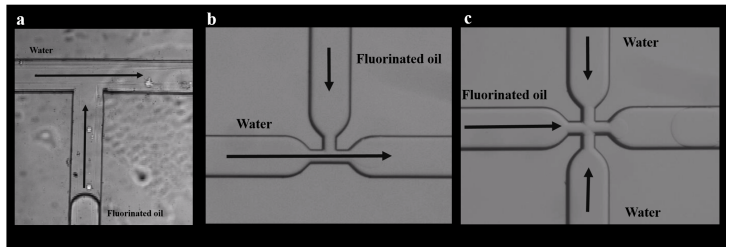

Figure 2.19: Microfluidic chips used to produce fluorinated emulsions: a) PDMS chip with T-junction geometry, b) glass chip with t-junction and c) flow-focusing geometry.

Even with the high viscosity of the fluorinated oil, there were no problems making the oil flow inside the channels of the chips: the applied flow rates was always low and

there was no leakage. For all of the following emulsification tests, we used 2%wt SDS in distilled water as continuous phase.

With PDMS chips we explored several flow rates: water flow, from 0.1 to 1 $\mu L/s$, oil flow: from 0.0005 to 0.0001 $\mu L/s$. With this chip, there were wettability problems: the hydrophilization did not work perfectly, so the oil adhered to the channel surfaces leading to a not proper emulsion production. Nevertheless, we obtained mono-disperse droplets, 150 μm in diameter.

With glass flow-focusing chips we explored several flow rates, reported in caption of **Figure 2.20**. From **Figure 2.20** it is evident that, by changing the flow rate, it is possible to obtain droplets of different sizes yet very mono-disperse. If we define γ as the ratio between the oil flow rate and water flow rate, the smaller γ is, the smaller the droplets are.

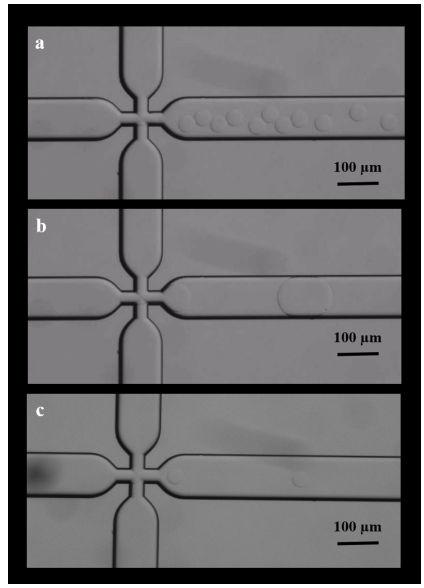

Figure 2.20: Images of Fomblin MD® emulsions during the production at different flow rates of the two phases, oil (f.r.o.) and water (f.r.w.). Depending on the flow rate ratio γ it is possible to control the sizes of the resulting droplets. In particular: a) γ =0.1 (f.r.o.= 1 nL/s and f.r.w.=10 nL/s), particle diameter= 40 μm b) γ =0.4 (f.r.o.= 4 nL/s and f.r.w.=10 nL/s) particle diameter=125 μm and c) γ =0.014 (f.r.o.= 1 nL/s and f.r.w.=70 nL/s) particle diameter=35 μm.

With glass T-J chips, we explored the various flow rates, from 1 to 50 nL/s for the oil phase and from 100 to 300 nL/s for water phase. Also with T-J we obtained highly mono-disperse droplets, as can be seen in **Figure 2.21**. These emulsions are stable and can resist mechanical stress (we have experimentally tested that they maintain their sizes after pipetting, for example). These droplets coalesce when ethanol is addedto the continuous phase, as expected.

As a result of these experiments, we proved that it is possible to create emulsions with fluorinated oil using a microfluidic device. We found that the flow-focusing technique enables more control of drop size: tuning the continuous and dispersed phase flows it is possible to control the size of the resulting droplets precisely. We obtained better results using glass chips than PDMS, due to wetting problems. Unfortunately, glass chips are commercial, expensive and can not be customized (dchoosing the size of the channels, for instance). An alternative solution may be to fabricate chips using Norland Optical Adhesive, NOA: a hydrophobic photo-sensitive polymer that, with appropriate surface

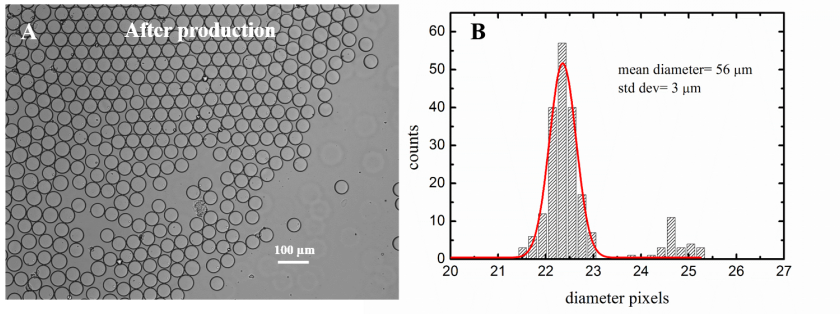

Figure 2.21: Fluorinated emulsion realized in microfluidics devices. A) Images of monodispersed Fomblin MD® droplets and B) their sizes distribution.

treatment, can be easily converted to hydrophilic. In this way, the realization of any kind of emulsification geometry (T-J or FF), with any kind of channel diameter (from 5 to 200 μm) is possible.

2.6.4 Realization of Fomblin MD 40® micro-beads

The micro-particles synthesized in this work are made using a fluorinated oil, Fomblin MD 40® (*Solvay Specialty Polymers*). An emulsion of Fomblin MD40® in water is made, using as stabilizer 1%wt SDS, with the membrane emulsification method. Before this emulsification, I tested two different photoinitiators to add to the emulsion composition in order to obtain solid particles: *potassium persulfate* (PP) and *Ciba Igracure 651* (CIBA). The main differences between these two photoinitiators are that PP is soluble in water, it degrades under UV radiation or temperatures exceeding 80° C and it is a bleaching agent, so the resulting samples do not change color over time [45] [46]. In contrast CIBA is not soluble in water, so it must be dispersed into the oil phase and it could confer a yellow color due to exposure to visible light.

Preliminary tests have shown that particles realized with PP are not stable over time in a range of solvents. In fact, as visible in **Figure 2.22**, when the emulsion continuous phase is replaced with ethanol, phase separation occursbetween the fluorinated oil and the alcohol, meaning that the particles are not completely solid, but still have a soft center that melts the photopolymerized external shell. On the other hand, beads produced with CIBA are solid in multiple solvents and remain so several months after their stnthesis. Therefore, I have decided to use CIBA for all the membrane emulsification.

Prior to the membrane emulsification, I dissolved 0.1%wt of photoinitiator CIBA in the dispersed phase. I performed the emulsion with a SPG membrane of nominal pore size 10.1 microns, under a pressure of 11 bar. Then I put the emulsion under UV lamp for 10 minutes (*Helio Italquarz*, 500 W), keeping the sample under slow-stirring agitation, to avoid sedimentation of the particles. The resulting colloids (**Figures 2.23B** and **Figure 2.23C**) have a wide polydispersity, probably due to an overlyo high emulsification pressure. After polymerization, I washed the colloids with MilliQ water, obtaining a low light scattering (**Figure 2.23A**). These colloids have an optimal chemical (in ethanol and bleach) and mechanical resistance (same sizes after centrifugation, 300 g) and they remain stable for several months after production.

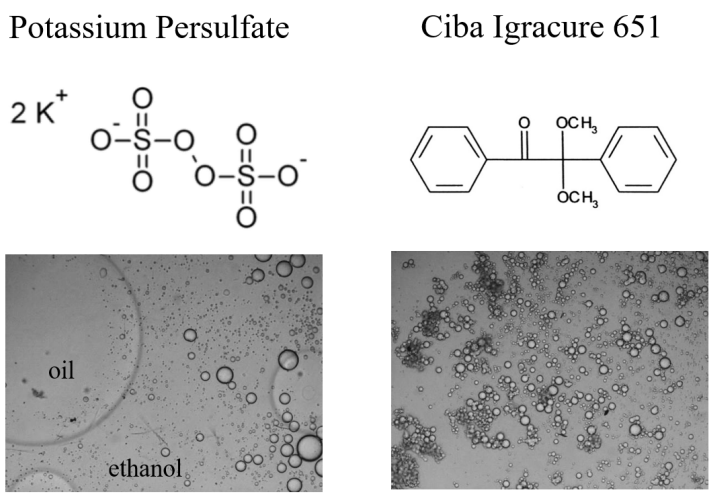

Figure 2.22: Chemical formulae of the two photo-initiators used in the photopolymerization tests. Also shown are microscope images of the beads in ethanol after UV radiation. It is noticable that the sample made with PP separates into two phases, meaning that the photopolymerization was not successful. The sample realized with CIBA remains stable into ethanol.

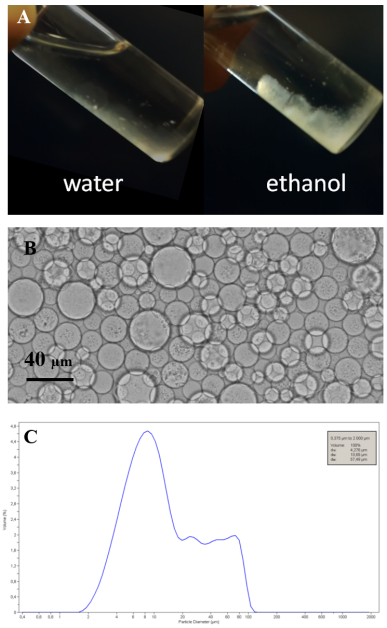

Figure 2.23: Fluorinated micro-beads. A) Beads dispersed in water are less visible than when dispersed in ethanol. B) Microscope images of the fluorinated beads. C) Size analysis of the fluorinated beads.

Chapter 3:
Optical response of phantom materials

In this chapter, I present the optical theories developed to describe the optical signal of materials iso-refractive to water when their interfaces are covered by a thin layer having different refractive index. First of all, I describe the *Reflective Phantom Interface* (RPI) approach, explaining how the reflectivity of a surface changes as a function of the number of molecules adsorbed [15]. This method comes from thin-layer interference theory. We developed this theory both in the case of an index-matched substrate and in the case of glass covered with an anti-reflective coating [29].

For porous materials, two different models are presented to describe their optical response when covered by a thin film: one has its origins in Rayleigh-Gans scattering theory (R-G) for core-shell media, [47], the other one is an implementation of the Random Telegraph Signal [48] [49] for a medium composed of three different materials.

3.1 Reflectivity by a thin layer: index-matched material

In the most general case, when there is an interface between two media that have different refractive indices n_1 and n_2, for light at normal incidence, the reflectivity R is $(\frac{n_2-n_1}{n_2+n_1})^2$. If the incoming light is not perpendicular to the interface, R depends on the incidence angle as well. When a thin layer of thickness h is present at this interface and has a refractive index equal to n_3, as shown in **Figure 3.1**, the reflectivity can be written as [50]:

$$R = \frac{(n_1 cos(\delta)\, cos(\theta_0) - n_3 cos(\delta)\, cos(\theta_{t2}))^2 + \left(n_1 n_3 cos(\theta_{t2})\, cos(\theta_0) - n_2^2 sin^2(\delta)\, cos^2(\theta_{t1})\right)^2}{(n_1 cos(\delta)\, cos(\theta_0) + n_3 cos(\delta)\, cos(\theta_{t2}))^2 + \left(n_1 n_3 cos(\theta_{t2})\, cos(\theta_0) + n_2^2 sin^2(\delta)\, cos^2(\theta_{t1})\right)^2} \tag{3.1}$$

where n_1, n_2, n_3 are the refractive indices of the three media, θ_0 is the incidence angle, θ_{t1} is the transmittance angle of the first material, θ_{t2} is the transmittance angle of the second material and $\delta = \frac{2\pi}{\lambda} n_1 h * cos(\theta_{t1})$. If the thickness h of the covering layer is small compared to the wavelength λ, it is possible to expand Equation 3.1 in the limit of $\delta \ll 1$, obtaining [15]:

$$R = R_0 \left(1 + \frac{h^2}{h_0^2}\right) \tag{3.2}$$

$$where\ h_0 = \frac{\lambda\sqrt{R_0}}{4\pi n_l r_{1l} cos(\theta_{t1})} \tag{3.3}$$

with R_0 the reflectivity of the surface in absence of the layer and $r_{1L}$is the reflection coefficient of the substrate/film interface. h_0 is the thickness at which the reflectivity doubles. If the layer is composed by molecules that are not uniformly distributed over the interface, h is the equivalent thickness, namely the thickness that the molecules would occupy if their mass were uniformly distributed over the entire surface. Knowing the density of the adsorbed molecule ρ, it is possible estimate the surface adsorbed mass density $\sigma = \rho h$, so Equation 3.2 can be re-written as:

$$\sigma = \sigma_0 \sqrt{\frac{R - R_0}{R_0}} \tag{3.4}$$

where $\sigma_0 = \rho h_0$. Hyflon AD®, an amorphous perfluoropolymer, has a refractive index equal to 1.328, hence the reflectivity of its surfaces in water is on the order of 10^{-6}.

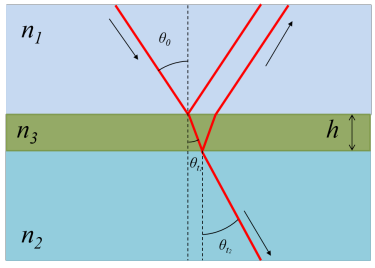

Figure 3.1: Scheme of reflected light intensity in the presence of a thin layer of thickness h and refractive index n_3 between of two media having refractive indices n_1 and n_2.

3.2 Reflectivity by a thin layer: reflectionless glass

It is possible to achieve low reflectivity in water by means of another technique, based on anti-reflective coatings with the possibility of optimal performance. This layer must cause a destructive interference between the rays reflected at the water/coating interface and the coating/substrate interface [29]. The reflectivity of this interface can be written as:

$$R = \frac{|r_{01} + r_{1s}e^{j2\alpha}|^2}{|1 + r_{01}r_{1s}e^{j2\alpha}|^2} \tag{3.5}$$

where for normal incidence $r_{01} = \frac{n_0 - n_1}{n_0 + n_1}$, $r_{1s} = \frac{n_1 - n_s}{n_1 + n_s}$ and $\alpha = kn_1h_1$, with $k = 2\pi/\lambda$ and λ being the wavelength of monochromatic illumination. Refering to **Figure 3.2**, when $n_1^2 = n_0n_s$ and $n_1h = \frac{\lambda}{4}$ the thin film acts as an ideal anti-reflection coating, leading to $R = 0$. In principle, this condition can be achieved by selecting a glass substrate and a dielectric coating with suitable refractive indices. In this work, I used glass with $n_s = 1.620$, and a coating of SiO_2 of refractive index $n_1 = 1.473$ and thickness of 101 nm. The use of this kind of glass substrate has been reported for the detection of molecular interaction [29] and in *Chapter 4* I will present the application of this approach to characterization of the interaction between human growth hormone in solution and the corresponding antibodies immobilized on the sensing surface, both in buffer and human serum.

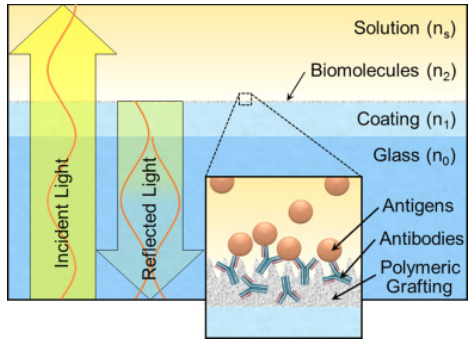

Figure 3.2: Schematic representation of the sensing material. A glass substrate with refractive index n0 was coated with a dielectric material with refractive index n1 and with the copoly (DMA–NAS–MAPS), on which various antibodies were immobilized. The chip was placed in contact with an aqueous solution with refractive index ns, containing various concentrations of target molecules. The intensity of light reflected by the multi-layer interface depends on the thickness of a thin layer of molecules with average refractive index n2, including the spotted anti- bodies and the target molecules captured by the antibodies. The relative thickness of the layers and wavelengths are drawn to scale.

In order to develop a simplified and practical model for the reflectivity of the functionalized surface, enabling a rational design of the sensing material, I consider a small perturbation around the condition of minimum reflectivity. Let me consider a multi-layered structure, where N layers with refractive indices n_1, ..., n_N, and thickness h_1, ..., h_N, respectively, are sandwiched between two semi-infinite media with refractive indices n_0 and n_s. If only the first layer with refractive index n_1 has a thickness h_1 comparable with the wavelength and all the other layers are much thinner than λ, their effects to the total reflectivity of the multi-layered surface can be accounted for just by adding an extra contribution to the phase retardation of the first layer. Accordingly, the

reflectivity can be computed using Equation 3.5 with

$$h = h_1 + \sum_{k=2}^{N} c_k h_k \tag{3.6}$$

Here $c_k = \frac{\left(n_k^2 - n_s^2\right)}{\left(n_1^2 - n_s^2\right)}$ are factors weighting the contribution from each thin layer to the effective thickness h, according to the corresponding refractive index. Note that $c_k <$ (=, >) 1 if $n_k <$ (=, >) n_1. It is worth noting that the effect of any modification in the structure (changes in the thickness and/or refractive index of the layers) can be accounted for by adjusting a single parameter, namely the effective thickness h of the equivalent single layer structure. Equation 3.5 can be further simplified considering small variations of the refractive indices and the thickness h relative to the condition of $R = 0$. Defining $\varepsilon = 2\,\alpha - \pi$, $\beta = \frac{r_{1s} - r_{01}}{r}$ and $r = \frac{r_{1s} + r_{01}}{2}$, Equation 3.5 can be rewritten in the lowest order in ε and β as:

$$R \approx \left(\frac{r}{1 + r^2}\right)^2 \left(\beta^2 + \varepsilon^2\right) \tag{3.7}$$

Equation 3.7 is a function of the effective layer thickness h, the wavelength λ (through ε), and the medium refractive index n_s (through β). Moreover, in the case of moderate polychromaticity of the illuminating light, characterized by an average wavenumber $< k >$ and a variance $\Delta k^2 =< k^2 > - < k >^2$ in vacuum, the reflectivity is obtained by averaging Equation 3.7 over the spectrum, thus yielding:

$$R \approx \left(\frac{r}{1 + r^2}\right)^2 \left(\beta^2 + < \varepsilon^2 >\right) \tag{3.8}$$

where $< \varepsilon^2 >= \left(2hn_1 < k > -\pi\right)^2 + \left(2hn_1 \Delta k\right)^2$. A minimum value of reflectivity R_0 is obtained for an effective thickness $h_0 = \frac{\pi}{2n_1 < k >}$.

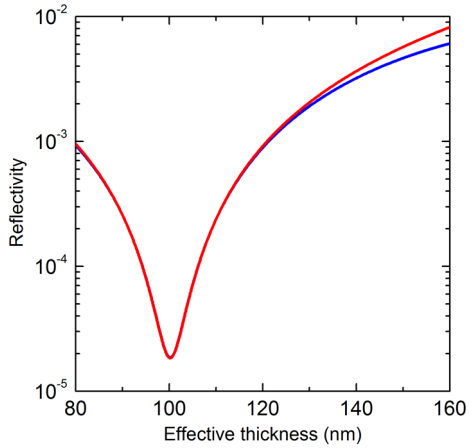

Figure 3.3: Reflectivity as a function of the effective thickness h calculated from Eq. (7) (red curve) in comparison to the exact Fresnel formula of Eq. (5) (blue dashed curve).

Figure 3.3 reports the reflectivity as a function of h calculated from Equation 3.7 (red curve) in comparison to the exact Fresnel formula of Equation 3.5 (blue curve) for a LED

illumination centered at 595 nm, which was used in the experiments presented later in *Chapter 4*. For thicknesses within h_0+ 20 nm the difference between the two approaches is less than 3%. Inspection of Equation 3.7 allows evaluation of the factors limiting the depth of the reflectivity minimum for $h \approx h_0$. Two additive contributions are present: the non-optimal agreement of the refractive index through the term β and the spectral width of the illumination source through Δk. Accordingly, the working conditions can be in principle adjusted so as to have the term $< \varepsilon^2 >$ always larger then β^2, hence strongly reducing the dependence of the reflectivity on uncontrolled variations in the refractive indices, possibly due to temperature fluctuations or variability of solution composition.

A simple inversion of Equation 3.8 expressing the effective thickness h as a function of R is obtained when the width of the illuminating spectrum is narrow relative to the average wavelength, namely $\Delta k^2 \ll < k^2 >$. In this case, the effective thickness can be obtained from the measured reflectivity R as:

$$h = h_0 + h^* \sqrt{\frac{R - R_0}{R_0}} \tag{3.9}$$

where the factor $h^* = \frac{\left(\beta^2 + \left(\frac{\pi \Delta k}{< k >}\right)^2\right)^{1/2}}{2n_{1<k>}}$ represents the effective thickness variation that, when added to h_0, leads to $R = 2R_0$. Accordingly, $\frac{1}{h^*}$ indicates the response sensitivity of the reflected intensity to increases of h. Combining Equation 3.8 with Equation 3.5, the measured reflectivity can be directly ascribed to the thicknesses and the refractive indices of different layers. In particular, in the case of a two-layer structure, in which the thickness h_1 of the first layer is close to h_0 and the thickness h_2 of the second layer is much smaller than λ, we obtain:

$$h_2 = \frac{1}{c_2} \left(h^* \sqrt{\frac{R - R_0}{R_0}} - \delta h \right) \tag{3.10}$$

where $\delta h = h_1 - h_0$and $c_2 = \frac{\left(n_2^2 - n_s^2\right)}{\left(n_1^2 - n_s^2\right)}$.

3.3 Optical response of weakly scattering systems

In this section, I present a model that describes the increase in the intensity of light scattered by a medium due to the presence of a thin molecular layer on its surfaces, when the medium and the solvent have almost the same refractive indices. This model is derived from reference [47], where the optical response of core-shell spherical nano-particles was described. Here, I extend the validity of this model to media with different shapes and characteristic lengthscales, in a quasi index-matching condition.

When the index matching condition between the medium and the dispersing solvent is nearly achieved, $|\frac{n_s}{n_m} - 1| \ll 1$, and when the typical dimension a of the medium exceeds the light wavelength λ subject to the phase condition $\frac{4\pi a}{\lambda}|\frac{n_s}{n_m} - 1| \ll 1$, Rayleigh-Gans theory describes the intensity os scattered light, [51]. In the most general case:

$$I_s = N\left\{(n_m^2 - n_s^2)\, F(k,a)\right\}^2 \tag{3.11}$$

where N is a constant that depends on the experimental apparatus and the number of scattering centers, n_m and n_s are the refractive indices of the medium and the solvent, respectively, and the function $F(k,a)$ is given by:

$$F(k,a) = \int_V e^{ik*r} dV \tag{3.12}$$

where V is the volume of the medium, k the scattering vector and r is the vector indicating the positon in space of the infinitesimal volume dV. In the case of spherical particles, $F(k,a)$ is equal to $\frac{3[sin(ka) - ka\, cos(ka)]}{k^3 a^3}$, where a is the radius of the sphere. Equation 3.12 is valid for all shapes of particles. If the medium is covered by a thin layer of thickness d with a different refractive index n_l, the scattered light becames:

$$I_{sl} = N\left\{(n_m^2 - n_s^2)\, F(k,a+d) + (n_l^2 - n_m^2)\,[F(k,a+d) - F(k,a)]\right\}^2 \tag{3.13}$$

If we now consider a system composed of spherical particles, polydispersed in radii around an average value $\check{r}$ with a gaussian distribution, the ratio of Equation 3.13 to Equation 3.11 gives the increase in the intensity of scattered light due to the presence of the thin covering layer. Without any approximation, it is possible to compute this ratio, taking into account the polydisperisity of the radii that is necessary to eliminate the oscillatory form of the shape factor. In **Figure 3.4** we report the ratio $\frac{I_{sl}}{I_s}$ as a function of $\check{r}$. It is apparent that, for large value of $\check{r}$, the ratio does not go to 1, but to a value that depends on the refractive indices of the particles and of the layer. In the case reported here, this value is equal to 1.83 ± 0.01.

To develop a more general model to describe the increase in scattered light intensity due to the presence of a thin covering layer, I can now consider the thickness of the layer d to be much smaller than the typical lengthscale of the medium, $d \ll a$. I can then expand $F(k,a)$ in the limit of small d, because the dependence on the thickness is only in this term. Equation 3.13 becomes:

$$I_{sl} = N\left\{(n_m^2 - n_s^2)\, F_d + (n_l^2 - n_s^2)\, \frac{dF_d}{da}\, d\right\}^2 \tag{3.14}$$

In the limit of small particles ($ka \ll 1$), we obtain $F = V$, and the behavior of phantom nano-particles is obtained. In particular, if I define the contrast C as the ratio of scat-

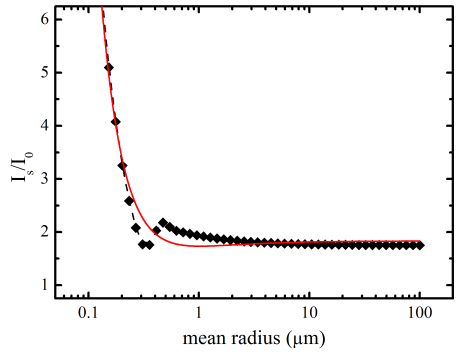

Figure 3.4: Ratio of scattered light from a system of polydispersed spheres with and without a thin molecular covering layer and without the layer. The system of polydisphersed spheres has a gaussian distribution around a mean radius value. The contrast is numerically calculated by taking the ratio of Eqs. 11 and 13 at a scattering angle of 30° , wavelength of 532 nm, layer thickness of 3 nm and with the following refractive indices: n_m=1.334, n_s=1.331 and n_l=1.435. The red line is a hyperbolic fit used to extrapolate the value of the contrast at large $\vec{r}$, which is 1.83 ± 0.01

tered light intensity by particles covered with a thin layer and bare particles, $C = \frac{I_{sl}}{I_s}$, for spherical particles, I obtain:

$$C = 1 + \frac{d^2}{d_0^2}, \tag{3.15}$$

where

$$d_0 = \frac{n_m^2 - n_s^2}{n_l^2 - n_s^2} \frac{a}{3} \tag{3.16}$$

As expected, the smaller particles provide a higher increase in scattered light intensity due to the presence of the shell layer [20].

In contrast, in the limiting case of $ka \ll 1$ with a quite significant polydispersity of the lengthscales a, Equation 3.14 must be averaged over these lengths to obtain the scattered light intensity:

$$I_{sl} = N \left((n_m^2 - n_s^2)^2 < F_d^2 > + (n_l^2 - n_s^2)^2 < \left(\frac{dF_d}{da} \right)^2 > d^2 + (n_m^2 - n_s^2)(n_l^2 - n_s^2) < F_d \frac{dF_d}{da} > d \right) \tag{3.17}$$

Thus, when the quantities F_d has several oscillations in the range over in which the average is calculated, the linear term in d, $< F_d \frac{dF_d}{da} >$ vanishes because F_d and $\frac{dF_d}{da}$ are in quadrature of phase, so their product is zero. The contrast C, now has the following form:

$$C = \frac{I_{sl}}{I_s} = 1 + \frac{(n_l^2 - n_s^2)^2}{(n_m^2 - n_s^2)^2} \frac{< \left(\frac{dF_d}{da} \right)^2 >}{< F_d^2 >} d^2 \tag{3.18}$$

The ratio between the two averaged quantities in this limit is always equal to k^2, as can be easily demonstrated in the case of spherical particles. So, for $d \ll a$ and $ka \gg 1$, the contrast can be written as in Eq. 3.15, but this time the term d_0 is given by:

$$d_0 = \frac{(n_m^2 - n_s^2)}{(n_l^2 - n_s^2)} \frac{1}{k} \tag{3.19}$$

where $k = 4\,\pi\,n_s sin(\theta_s/2)/\lambda$ and $\theta_s$the scattering angle. This relationship has exactly the same form as Eq. 3.2 or reflectivity by a thin layer at the interface between two media under index-matching conditions. If I take into account the equivalence between the angle of incidence θ_0 in the case of the reflection and the scattering angle θ_s in the case of a scattering geometry, as shown in **Figure 3.5**, $\theta_0 = \frac{\pi}{2} - \frac{\theta_s}{2}$, then the two quantities in Eqs. 3.3 and 3.19, quite surprise, assume the same numerical values. In **Figure 3.6** the ratio $\frac{h_0}{d_0}$ is reported as a function of θ_0, calculated for the same media refractive indicis and wavelength of light. These two quantities differ by less than 20% for a reflective angle up to $80°$ or a scattering angle up to $20°$.

The optical model developed here can be applied to the study of molecular adsorption both on porous-media and into a region of close packed micro-beads.

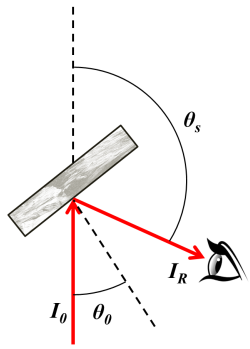

Figure 3.5: Scattering angle relative to the incidence angle.

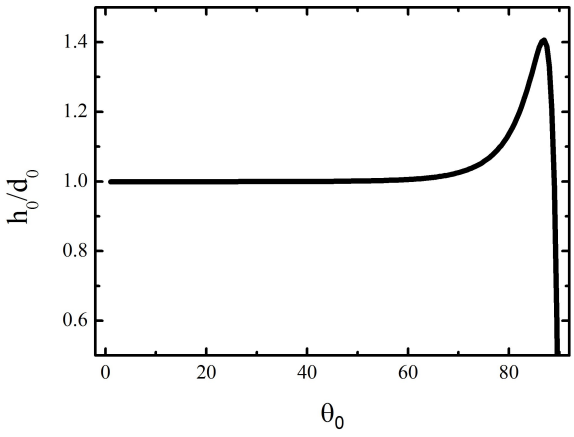

Figure 3.6: Ratio h_0/d_0 as a function of the incidence angle.

In the sections above, I found that the increase in reflected and scattered light intensities due to molecular adsorption in different geometries follows the same formula, namely Eqs. 3.2, 3.8 and 3.15, with different values for the sensitivities, which are h_0, h^* and d_0 respectively. To summarize these results, I report the sensitivity values in **Table 3.3** for the cases studied.

Table 3.1: Optical responce of various substrates with their respective sensitivities.

	Contrasts	**Sensitivities**
Reflectivity: phantom prism	$R = R_0 \left(1 + \frac{h^2}{h_0^2}\right)$	$h_0 = \frac{\lambda\sqrt{R_0}}{4\pi n_l r_{1l} cos(\theta_{t1})}$
Reflectivity: coated glass	$R = R_0 \left(1 + \frac{(h-h_0)^2}{h*^2}\right)$	$h* = \frac{\left(\beta^2 + \left(\frac{\pi\Delta k}{<k>}\right)^2\right)^{1/2}}{2n_{1<k>}}$
Scattering: polydispersed spheres	$I_s = I_0 \left(1 + \frac{d^2}{d_0^2}\right)$	$d_0 = \frac{(n_m^2 - n_s^2)}{(n_l^2 - n_s^2)} \frac{\lambda}{4\,\pi\, n_s sin(\theta_s/2)}$

3.4 Scattered light from a random porous material: Random Telegraph Signal

Here I present a theoretical model that describes the optical response of a porous material under quasi-index-matching conditions. This model is derived from a previously developed model, known as *Random Telegraph Signal* (RTS) [48] [49]. I implemented it to describe the adsorption on porous media surfaces of a thin molecular layer. I show how the scattered light and the turbidity of a porous material depend on two characteristic lengths: the typical pore size p and the typical length of the polymer matrix inside the membrane m. To understand the meaning of these lengths, see **Figure 3.7B**.

To obtain changes in the intensity of light scattered by a medium, it is necessary to know how the dielectric constant changes inside this material as a result of the process being studied. By calculating the autocorrelation function of the dielectric constant, it is possible to obtain the scattered light intensity $I(q)$. Inside a porous medium, along any straight line, the dielectric constant $\varepsilon(r)$ varies between two typical values: ε_m, the dielectric constant of the membrane, and ε_p, the dielectric constant of the solvent that fills the pores of the membrane.

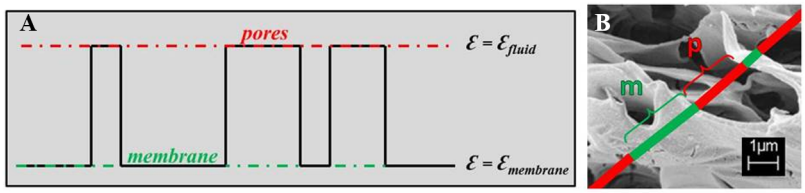

Figure 3.7: Step function of the dielectric constant inside a porous membrane along a straight line that transects the material.

The function $\varepsilon(r)$ is a steps function, as shown in **Figure 3.7A**, where the lengths of the steps are randomly distributed around two average values: m, the characteristic length of the membrane, and p, the characteristic length of the pore. We can build the correlation function of $\varepsilon(r)$ by computing the jumping probability from one value of ε to another in small steps. In fact, the correlation function is defined as follows:

$$< \varepsilon(r)\,\varepsilon(r+dr) >= \sum_{i,j} \varepsilon_i \varepsilon_j \,[Prob\,\varepsilon(r) = \varepsilon_i]\,[Prob\,\varepsilon(r+dr) = \varepsilon_j,\, beeing\,\varepsilon(r) = \varepsilon_i] \quad (3.20)$$

For instance, the probability to be in the state characterized with $\varepsilon = \varepsilon_m$, for any value of *r*, is $\frac{m}{m+p}$, and, in the same way, the probability to be in a state with $\varepsilon = \varepsilon_p$, for any value of r, is $\frac{p}{m+p}$. So we can re-write relation (20) :

$$< \varepsilon(r)\,\varepsilon(r+dr) >= \varepsilon_p\varepsilon_m \frac{p}{m+p} P_{pm}(r) + \varepsilon_p\varepsilon_m \frac{m}{m+p} P_{mp}(r) + \quad (3.21)$$

$$+\varepsilon_p^2 \frac{p}{m+p} P_{pp}(r) + \varepsilon_m^2 \frac{m}{m+p} P_{mm}(r)$$

where $P_{ij}(r)$ is the probability to jump from state i to state j. These probabilities must satisfy the completeness relation: $P_{mm}(r) + P_{mp}(r) = 1$ and $P_{pp}(r) + P_{pm}(r) = 1$. Replacing these two relations in Equation 3.21, the system reduces to the solution to

two differential equations. Each probability in Equation 3.21 can be written as follows, with the help of **Figure 3.8**. Starting from the white point, there are two different paths to be in the membrane state with $\varepsilon = \varepsilon_m$ after a step $r + dr$: one described by the red arrows, in which at distance r, $\varepsilon = \varepsilon_p$ with the following step dr, we come back into $\varepsilon = \varepsilon_m$,or the path described by the yellow arrows, in which $\varepsilon = \varepsilon_m$. I have just described the probability $P_{mm}(r + dr)$, which can be written as: $P_{mm}(r + dr) = P_{mp}(r)\frac{dr}{p} + P_{mm}(r)\frac{m-dr}{m}$. If I assume an infinitesimal step dr, this probability becomes:

$$\frac{dP_{mm}(r)}{dr} = \frac{1}{p} - \left(\frac{1}{m} + \frac{1}{p}\right) P_{mm}(r) \tag{3.22}$$

with solution

$$P_{mm}(r) = \frac{1}{p+m}\left(p\, e^{-(\frac{1}{m}+\frac{1}{p})} + m\right) \tag{3.23}$$

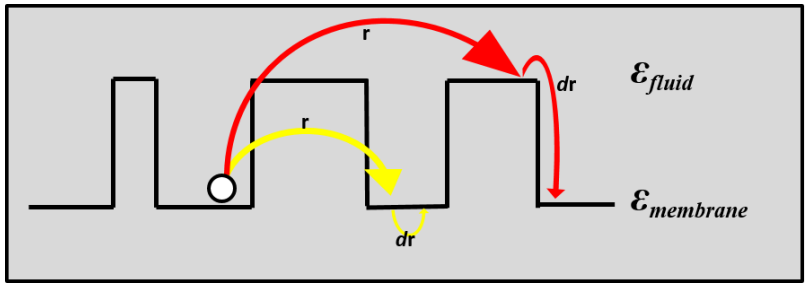

Figure 3.8: Probability Pmm(r+dr), to start and come back in the membrane state, after a step r+dr

It is possible to write the same relations for $P_{pp}(r)$ and finally to substitute these probabilities into Eq.3.21. Subtracting from this the average value of the dielectric constant, it is possible to obtain the fluctuations:

$$< \delta\varepsilon(r)\, \delta\varepsilon(r + dr) >= \frac{p\, m}{(p+m)^2} \left(\varepsilon_p - \varepsilon_m\right)^2 e^{-a\, r} \tag{3.24}$$

$$where\ a = \frac{1}{p} + \frac{1}{m}.$$

Applying the Fourier Transform process to this last quantity, it is possible to know the scattered intensity by a medium with such fluctuations in its dielectric constant, because $I_s(q, R) = \frac{k^4 |E_0|^2}{16\,\pi^2 R^2 \varepsilon_a^2} < |\delta\varepsilon(q)|^2 >$ [52], where R is the distance between the scattering volume and the observation point, k is the wave vector, $|E_0|^2 = I_0$ is the incident light intensity and ε_a is the average dielectric constant of the medium. Once we have the scattered intensity, it is also possible to compute the turbidity of the medium, since it is defined as the total scattering cross section per unit volume and it is given by integrating $I(q, R)$ in all directions [52]:

$$\tau = \frac{\int I_s(q) R^2}{I_0 V} \tag{3.25}$$

Turbidity here represents the loss of total energy per second per unit volume, scaled to the incident light intensity. Therefore, these two quantities for the porous medium,

can be written as follows:

$$I(q) = \frac{k^4 I_0}{16\,\pi^2 R^2 < \varepsilon >^2} \frac{p\,m}{(p+m)^2} (\varepsilon_p - \varepsilon_m)^2 \frac{4\pi\, V\, a}{(q^2+a^2)^2} \tag{3.26}$$

$$\tau = \frac{\frac{p\,m}{(p+m)^2} (\varepsilon_p - \varepsilon_m)^2}{< \varepsilon >^2} a \frac{\frac{k^4}{a^4}}{1 + 4\frac{k^2}{a^2}} \tag{3.27}$$

$$where \;\; < \varepsilon >^2 = \frac{\varepsilon_m m + \varepsilon_p p}{(m+p)^2}$$

With this model, the optical properties of the porous medium depend only on the refractive indices of the membrane and the soaking fluid and on two characteristic lengths, m and p.

To understand what happens to the scattered light and to turbidity when a thin molecular layer adsorbs onto the surfaces of the porous membrane, I developed the model just presented in the case of another jump in the dielectric function at each solvent/membrane interface, due to the presence of the molecular layer, **Figure 3.9**.

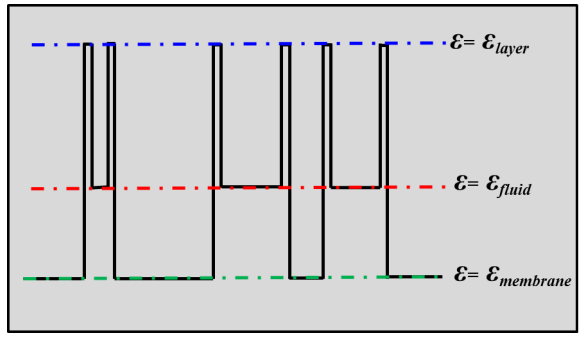

Figure 3.9: Step function inside the porous medium in the presence of a molecular layer adsorbed at the fluid/membrane interface.

Now it is necessary to write the autocorrelation function of this new step function. Also in this case, the definition in Eq. 3.21 is still valid, but the probabilities of jump are different. If I define by the label T_1 the layer between the membrane and the fluid, by T_2 the layer between the fluid and the membrane, and by t the thickness of the surfactant layer having a dielectric constant equal to ε_t, then the autocorrelation function becomes:

$$< \varepsilon(r)\,\varepsilon(r+dr) >=$$

$$\frac{m\,\varepsilon_m}{m+p+2\,t} \left(\varepsilon_p\, P_{mp}(r+dr) + \varepsilon_m\, P_{mm}(r+dr) + \varepsilon_t\, P_{mT1}(r+dr) + \varepsilon_t\, P_{mT2}(r+dr)\right) +$$

$$\frac{p\,\varepsilon_p}{m+p+2\,t} \left(\varepsilon_p\, P_{pp}(r+dr) + \varepsilon_m\, P_{pm}(r+dr) + \varepsilon_t\, P_{pT1}(r+dr) + \varepsilon_t\, P_{pT2}(r+dr)\right) +$$

$$\frac{t\,\varepsilon_m}{m+p+2\,t} \left(\varepsilon_p\, P_{T1p}(r+dr) + \varepsilon_m\, P_{T1m}(r+dr) + \varepsilon_t\, P_{T1T1}(r+dr) + \varepsilon_t\, P_{T1T2}(r+dr)\right) +$$

$$\frac{t\,\varepsilon_m}{m+p+2\,t} \left(\varepsilon_p\, P_{T2p}(r+dr) + \varepsilon_m\, P_{T2m}(r+dr) + \varepsilon_t\, P_{T2T1}(r+dr) + \varepsilon_t\, P_{T2T2}(r+dr)\right)$$

Now I have to write the different probabilities that appear in the previous equation. For instance, the probability to be in state m after a step dr is:

$$P_m(r+dr) = P_m(r)\frac{m-dr}{m} + P_{T2}(r)\frac{dr}{t}$$

which is the probability of being at r in state m and staying in that state after the step dr, plus the probability of being in the state T_2 at r and jumping to the state m with the step dr. All the other probabilities can be written in the same way. If now I suppose the step dr infinitesimal, the problem is reduced to this set of differential equations:

$$\frac{dP_m(r)}{dr} = \frac{P_{T2}(r)}{t} - \frac{P_m(r)}{m}$$

$$\frac{dP_p(r)}{dr} = \frac{P_{T1}(r)}{t} - \frac{P_p(r)}{p}$$

$$\frac{dP_{T1}(r)}{dr} = \frac{P_m(r)}{m} - \frac{P_{T1}(r)}{t}$$

$$\frac{dP_{T2}(r)}{dr} = \frac{P_p(r)}{p} - \frac{P_{T2}(r)}{t}$$

To obtain the correlation function of the dielectric constant, it is necessary to solve this system of appropriate equations with different boundary conditions. For example, if wI want to know the probability to start at state m and arrive in any other state, the boundary condition is $P_m(0) = 1$. Because of the complexity of this system, a set of 16 differential equations, the solution can be only obtained numerically. The resulting autocorrelation function has the form of a double exponential decay wherein the two characteristic decorrelation times depend on the three lenghtscales m, p and t. To obtain the scattered intensity, I numerically Fourier transform the autocorrelation function and then an average around the experimental observation q is performed. In **Figure 3.10** the calculated autocorrelation is shown with the corresponding scattered intensity.

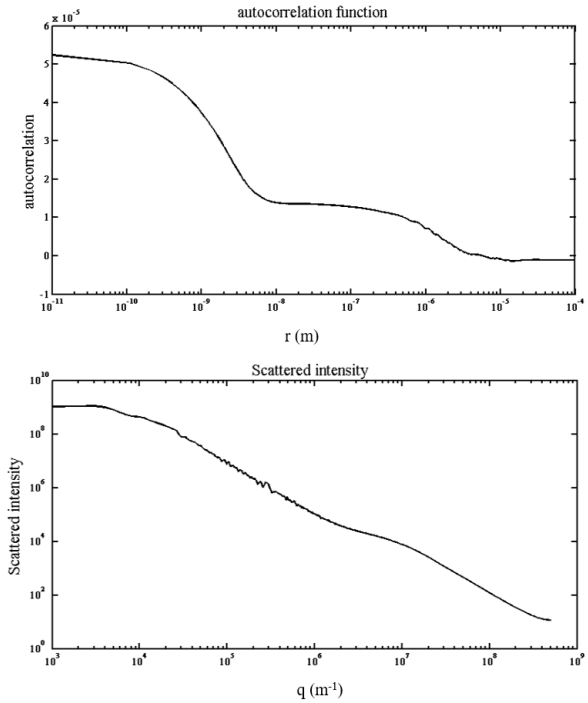

Figure 3.10: Autocorrelation function (a) and scattered intensity (b) analytically computed for a medium with $m = 2 * 10^{-6}$, $p = 4 * 10^{-6}$ and $m = 2 * 10^{-9}$.

Chapter 4:
Label-free, optical biosensor based on reflectionless glass

In this chapter, a different method to obtain a reflectionless media, that is not based on fluorinated material, is presented. In this case, a glass with a proper anti-reflective SiO_2 coating is the sensing surface and can serve as disposable label-free biosensing chips, enabling the multiplex detection and characterization of biomolecular interactions. A thin, multi-functional copolymer coating based on dimethylacrylamide provides the covalent immobilization of antibodies onto the surface, while maintaining at a minimum the non-specific adsorption in complex media. Here I present experiments that demonstrate the detection performance of this glass substrate by characterizing the interaction between human growth hormone in solution and the corresponding antibodies immobilized on the sensing surface, both in buffer and human serum, yielding a limit of detection of a few ng/ml. The work reported in this chapter is the content of a publication, *Multi-Spot, Label-Free Immunoassay on Reflectionless Glass*, Biosens. Bioelectron., Volume 74, 15 December 2015, Pages 539–545, [29].

4.1 Assay design

In this section, the *Reflective Phantom Interface* method, already used to describe the molecular interaction that takes place on a fluorinated phantom surface [15], is exploited to quantify the amount of bio-molecular targets in solution (antigens) captured by specific probes (antibodies) immobilized on two different glass substrates. These glass chips have a SiO_2 anti-reflective coating layer of two different thicknesses: 79 nm (A chip) and 101 nm (B chip) optimized for having a minimum of reflectivity in the yellow or in the blue spectral region, respectively. These substrates were coated with the copoly(DMA-NAS-MAPS) [27] and spotted with hGH-Ab. Defining $\Delta h = h - h_p$, where h_p is the effective thickness estimated from the reflectivity of the probe layer before binding of the targets through $h = h_0 + h^* \sqrt{\frac{R-R_0}{R_0}}$ (Equation 3.9 in Section 3.2), the surface density of surface bound targets is obtained as $\sigma = \rho_0 \Delta h$, where $\rho_0 = \rho \frac{(n_1^2 - n_s^2)}{(n_2^2 - n_s^2)}$ and where ρ and n_2 are the volume density and the refractive index of a packed layer of target molecules, respectively, n_s is the refractive index of the solution and n_1 is the refractive index of the SiO_2 coating. From a practical point of view, a simple experimental set-up enables to easily measure a signal $u(t)$ arbitrarily proportional to the absolute reflectivity of the interface. **Figure 4.1a** shows the image of the intensity reflected by a surface spotted with Bovine serum Albumin (BSA, green) and antibodies targeting the human growth hormone (hGH-Ab, brown). A horizontal profile of reflectivity calculated from the pixel brightness is reported in **Figure 4.1b**, from which the thickness of the biomolecular layer on the top of the antibody spots is obtained through Equation 3.9 in Section 3.2 (**Figure 4.1c**). In practice, h_2, Δh and σ can be more simply estimated from $u(t)/u_0 = R/R_0$, where u_0 is the brightness of the bare SiO_2 surface, which can be obtained from a reference area.

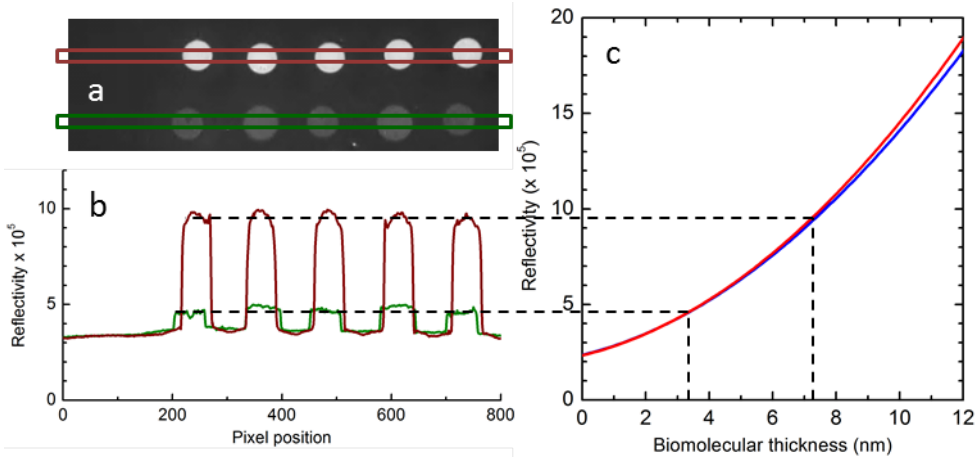

Figure 4.1: a) Image of the light reflected by a surface spotted with hGH-Ab antibodies (upper row) and BSA (lower row). b) Horizontal profile of reflectivity calculated from the pixel brightness of panel b, across the hGH-Ab (brown curve, brown region in panel b) and BSA (green curve, green region in panel b) spots. c) Reflectivity as a function of the thickness of the biomolecular layer on the top of the antibody spots calculated with Equation # (red curve) and Equation # (blue curve). The dashed lines indicate the thickness corresponding to the reflectivity extracted from panel b.

The different brightness of the two spot types in **Figure 4.1a** directly indicates a different amount of biomolecules immobilized on the surface. In terms of thickness, values of about 3.3 nm and 7.2 nm are extracted for the BSA and the hGH-Ab spots, respectively.

The observed difference cannot be ascribed to the different molecular mass and volume of the two species. A different spacing among the surface immobilized molecules must be considered, being the surface density of BSA slightly lower than a compact mono-layer and that of hGH-Ab slightly higher, hence indicating some degree of 3D positioning of the antibodies due to the swollen structure copoly(DMA-NAS-MAPS). More generally, the amount of surface immobilized compounds, even after optimization of the immobilization conditions, is found to depend rather strongly on the specific kind of molecules, arguably reflecting differences in the effective availability of amine groups suitable for the immobilization reaction.

4.2 Quantification of antibody-antigen interaction

The surface immobilized antibodies are capable of capturing their specific target antigen in solution, hence providing an increase of the spot reflectivity. **Figure 4.2a** reports the surface density measured on the top of hGH-Ab spots, while increasing concentrations of hGH were added in solution under continuous stirring, using a B chip. Concentrations as small as a few ng/ml provide a clear signal, distinct from the substantially constant signal of reference spots and also distinct from the signal noise, which corresponds to an uncertainty of a few pg/mm^2. Single exponential growths were observed after each addition, with amplitudes and characteristic rates depending on the hGH concentration c in solution. In particular, the asymptotic value of surface density after each addition $\sigma_{eq}(c)$ was found to follow a simple Langmuir behavior (**Figure 4.2b**, red points and line), from which the saturation amount of target molecules σ_0 and the equilibrium dissociation constant K_D are extracted, being:

$$\sigma_{\text{eq}}(C) = \frac{\sigma_0}{1 + \frac{K_D}{C}} \tag{4.1}$$

Also the characteristic rate $\Gamma(c)$ was also found to depend on c. In **Figure 4.2c** we plot the values of the initial slope of the binding curves $\Gamma_i(c) = \sigma_{eq}(c)\,\Gamma(c)$. From Eq. 4.1 and since $\Gamma(C) = k_{on}C + k_{off}$, we obtain $\Gamma_i(c) = \sigma_0\, k_{on}c.$, where k_{on} and k_{off} are the association and dissociation kinetic coefficients and $K_D = k_{off}/k_{on}$. Therefore, the c dependence of $\Gamma_i(c)$ is expected to simply show a linear growth without intercept. As shown in **Figure 4.2c** (red points and line), this behavior is confirmed up to about $c = 1\mu g/ml$. Higher concentrations led to larger surface density of bound target molecules, where the crowding may restrict the access to the remaining binding sites, hence affecting the rate. The parameters extracted from the fits are K_D = 7.41 nM and $k_{off} = 1.66 \cdot 10^{-3} s^{-1}$, and consequently $k_{on} = 2.24 \cdot 10^5 M^{-1} s^{-1}$

The consistency of the optical model described in Section 3.2, was confirmed by similar experiments performed on different sensing substrates. The equilibrium surface density and the observed kinetic binding rates measured with A chips are reported in **Figure 4.2b** and **4.2c** (purple points and lines), respectively. The values of the equilibrium dissociation constant and the kinetic rates extracted from the fit were very similar to those measured with the B chips, being K_D = 6.92 nM and $k_{off} = 2.53{\cdot}10^{-3} s^{-1}$, for the A chips. Additionally, the amount of antigen that saturated the spot surface was similar for the two glass chips. A further validation of the method was obtained from the comparison with the detection method previously proposed, based on fluorinated plastic substrates [15]. Equilibrium and kinetic parameters of the interaction between hGH and hGH-Ab obtained with the glass chips were confirmed also using the fluorinated substrate.

Considering the extracted values of the dissociation constant K_D for the hGH/hGH-Ab interaction, Equation 4.1 enabled to estimate the limit of detection for hGH, in this

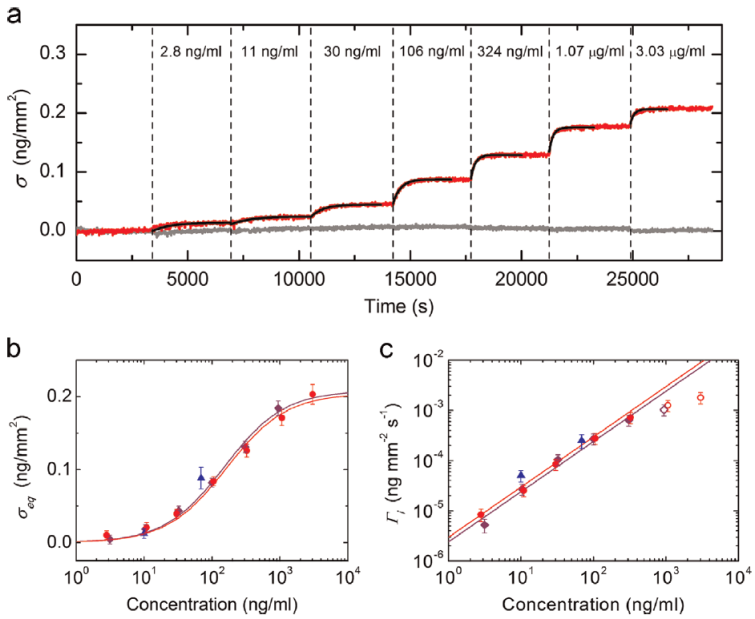

Figure 4.2: Equilibrium and kinetics of hGH binding. (a) Surface density as a function of time on the top of hGH-Ab spots (red) and of HBs-Ab spots (gray) measured after the addition of increasing amounts of hGH in buffer, at the times indicated by the vertical dashed lines, using a B chip. The corresponding total concentration in cuvette is reported. The black lines are single exponential fits. The asymptotic values (b) and initial slopes (c) of the binding curves reported in panel a are reported as red circles. The values from a similar experiment on a A glass are reported as purple diamonds. The blue triangles represent the values obtained in 60% human serum. Error bars on the data points of panels b and c are the standard deviations of the values extracted from about a dozen of spots. In panel b and c the lines represent the fit of the full points with corresponding color using equation (1) and a linear dependence with zero intercept, respectively.

experimental conditions. The signal fluctuations corresponded to an instrument detection limit at three standard deviation slightly smaller than $5\,pg/mm^2$. The concentration of hGH expected to provide a signal corresponding to such instrument detection limit was obtained from Equation 4.1 and it is about 3 ng/ml.

4.3 Effect of complex matrices

Given the sensitivity of the RPI detection to minute increases of reflected light intensity, in principle significant limitations could be expected in the case of particularly complex matrices, potentially providing a refractive index rather different from water, as well as a pronounced absorbance and a strong background of scattered light. On the contrary, the acquisition of a narrow angular range of light around the direction of specular reflection provides a rather effective suppression of scattered light. Additionally, the presence of absorbance to a certain extent may also be beneficial, contributing to the limitation of stray light originating from the sample cuvette. The capability of the method to detect tiny amounts of biomolecules immobilized onto the sensing surface is demonstrated by the fact that antibody spots are imaged at high quality even in absorbing and scattering media. **Figure 4.3** shows different kinds of spots in buffer, fetal bovine serum (FBS) in concentration of 66% and 100%, a cell culture medium (Dulbecco's Modified Eagle's medium, DMEM), cow milk and 10% cocoa cream. The spots are formed by BSA, hGH-Ab and antibodies targeting human hepatitis B surface antigen (HBs-Ab), HIV p24

capsid protein (p24-Ab) and beta-lactoglobulin (bL-Ab). Remarkably, in all cases the reflectivity of the spots provides a clear signal relative to the copolymer background, despite the absorbance and the opacity of the corresponding bulk media, as shown in **Figure 4.3**.

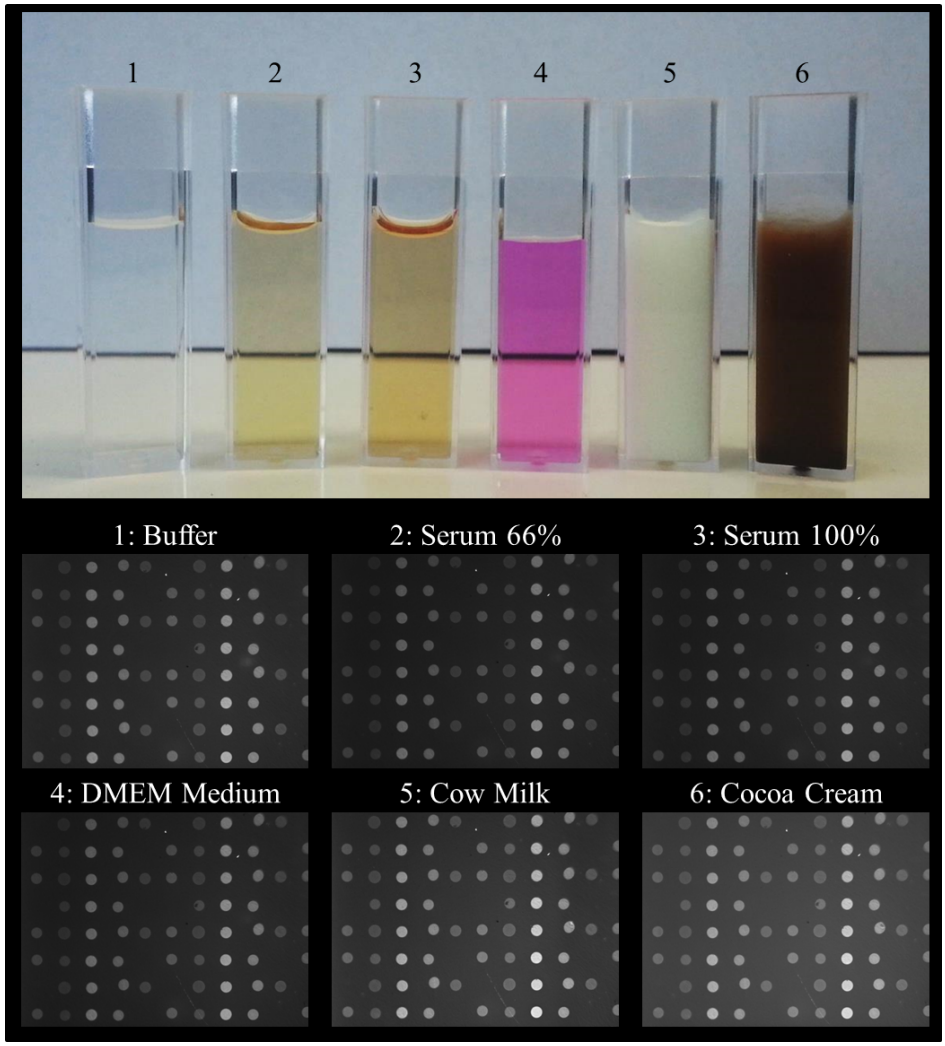

Figure 4.3: RPI images in complex media. (Upper panel) Picture of cuvettes filled with buffer (1) serum 66% (2) and 100% (3), cell culture medium (4), cow milk (5) and 10% cocoa cream (6). (Lower panel) RPI images of the light reflected from the same glass chip in contact with the samples 1-6. The spots within a column are made with the same probe molecule. From the left: BSA, hGH-Ab, HBs-Ab, p24-Ab and bL-Ab, then, the sequence of spot column is repeated.

The high contrast of the spots indicates that fractions of a biomolecular monolayer can be easily measured, with performance similar to those obtained in a clear buffer solution. The physical capability of the method to detect molecular binding even in complex matrices represents an important feature, which however does not guarantee high sensitivity if the non-specific interactions are kept to a minimum. Indeed, major limitations may commonly arise from the non-specific adsorption of undetermined matrix components. High levels of non-specific binding can prevent the quantitative determination

of molecular recognition processes in any kind of detection method, and in particular in label-free approaches, which do not make use of secondary antibodies linked to reporter molecules. On the other hand, only label-free methods can provide a detection signal without secondary antibodies, thus offering an opportunity of designing a much simpler assay procedure and increasing the multiplex capability thanks to the absence of constraints possibly due to cross-interactions. In order to investigate the effect of non-specific adsorption, the amount of material adhering onto the sensing surface was measured as a function of time, when in contact with bovine serum. **Figure 4.4a** reports the raw signal of reflectivity of spots of BSA and of antibodies targeting bL-Ab and HBs-Ab, measured at increasing concentrations of serum, in comparison with the signal of the copolymer background. The jumps in correspondence of the serum additions are due to sudden changes of the refractive index of the solution and do not contribute to the estimate of the mass adhering onto the surface (**Figure 4.4b**). The amount of adsorbed substances is found to depend strongly on the kind of molecular layer on the surface, being negligible for the copoly(DMA-NAS-MAPS) and the BSA spots, and relatively pronounced for bL-Ab and HBs-Ab, although qualitatively different. In particular, the average asymptotic value of surface density as a function of time for 67% vol/vol of serum is found to be about 1 ng/mm^2 for the bL-Ab spots and 1.8 ng/mm^2 for HBs-Ab. The dependence of the asymptotic values on the serum concentration also shows different behaviors depending on the immobilized molecules, as reported in the inset of **Figure 4.4b**. In particular, for HBs-Ab, a strong dependence on serum concentration is found until about 20%-30%, whereas further additions of serum have smaller effects on the non-specific binding to the surface. More generally, the amount of non-specific binding observed at 10% serum is comparable to what was found with the perfluorinated plastic substrate with a similar copolymer coating for the same concentration of serum and, accordingly, much lower than what typically measured on dextran coating layer.

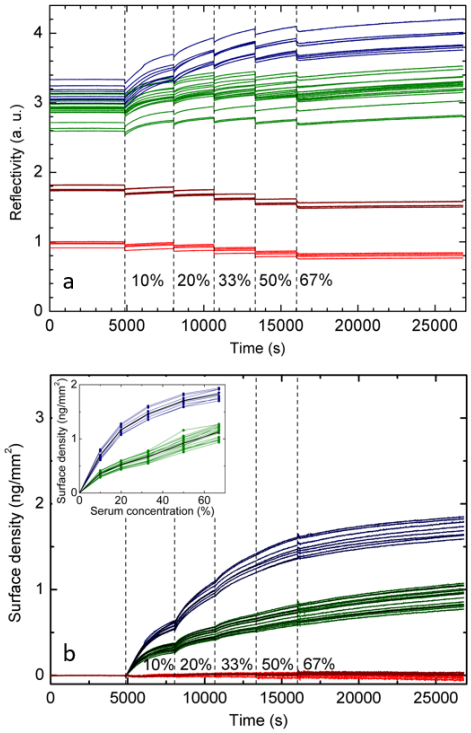

Figure 4.4: Non-specific adhesion of serum components. (a) Raw data of reflected light intensity, where the jumps are due to the sudden changes of refractive index upon addition of bovine serum to the concentration indicated, and (b) corresponding values of surface density. The addition times are indicated by the vertical dashed lines. The curves refer to copoly(DMA-NAS-MAPS) (red) and spots of BSA (brown), bL-Ab (green) and HBs-Ab (blue). Inset: estimated surface density at equilibrium as a function of the serum concentration for bL-Ab (green) and HBs-Ab (blue) spots.

4.4 Detection of human growth hormone in serum

From the comparison of **Figure 4.2** and **Figure 4.4**, it is derived that the non-specific binding can provide an increase of surface density significantly higher than that due to the specific recognition of hGH. However, it was surprisingly found that the spotted antibodies still preserve almost unaltered their function of specific binders to the corresponding antigen, even at high serum concentration. **Figure 4.5** shows that the amount of material adhering onto hGH-Ab spots after the addition of 33% and 60% human serum containing tiny amount of hGH, of the order of 1 ng/ml, reaches a rather low value of less than 0.3 ng/mm^2 after a few hours, although maintaining a significant increase as a function of time. On the top of this increase, the addition of 10 ng/ml of hGH yields a detectable response, whose exponential component shows characteristics similar to those measured in buffer at analogous concentrations. The behavior is also confirmed for 70 ng/ml of hGH, which induces a much higher response. The signal contribution due to hGH binding can be extracted subtracting the extrapolated signal of the non-specific adsorption of serum and fitting the resulting curve with a single exponential growth. The plateau and the rate of the obtained binding curve are reported as blue dots in **Figures 4.2b** and **4.2c**, respectively, where their consistency with the behavior measured in buffer is shown. The limited effect of non-specific binding of bovine fetal serum on antibodies targeting biomarkers of hepatitis B and HIV was previously reported for serum dilution of 10%. The results reported here, although consistent with the previous studies, show that even in the case of human serum at much higher concentrations the amount of non-specific binding on hGH-Ab spots is generally lower and, remarkably, the specific antigen-antibody interaction still takes place with characteristics similar to those observed in buffer solution.

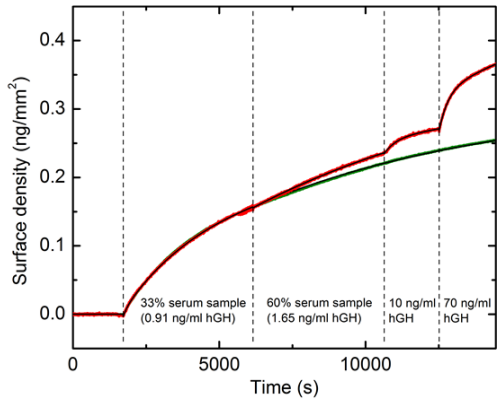

Figure 4.5: Binding of hGH to hGH-Ab spots in human serum. Surface density on the top of hGH-Ab (red) and HBs-Ab (green) spots measured after the addition of human serum to 33% and 60%v/v, and after the addition of hGH to 10ng/ml and 70 ng/ml in 60% serum, as indicated by the vertical dashed lines and the corresponding legends.

In this chapter, I have shown that also the deposition of anti-reflective coatings on glass enables to reach extremely low reflectivity in aqueous solution, of the same order of magnitude of fluorinated plastics. In these conditions of low background signal, the surface can serve as a novel kind of sensing interface for the recently proposed RPI label-free bio-detection. By using this substrate, obtained high sensitivity and clean images of the spotted surface even in turbid and absorbing media can be obtained. Moreover, and rather unexpectedly, I found that the binding performance of the immobilized antibodies

was unaltered by the presence of non-specific adsorption due to 60% human serum. This method enabled detecting hGH in a few minutes, with an estimated limit of detection of about 3 ng/ml. Such performance is of interest for the monitoring of hGH-related diseases and therapies and for anti-doping tests. Additionally, the insensitivity of the optical detection to the presence of strongly absorbing and scattering media and the existence of a large variety of consolidated surface treatments for SiO_2 layers are important features. These are expected to boost the further developments of RPI glass slides for a wider range of applications that involve complex matrices, such as human diagnostics and biochemical analysis on food and beverages.

Chapter 5:
Study of molecular adsorption by the prism sensor

Molecular adsorption is the adhesion of molecules from a fluid onto a surface. This process creates a film of the adsorbate on the surface of the adsorbent. The adsorption can take place spontaneously if a driving force is present , for example thydrophobic interactions in a polar solvent. In this case, all molecules that have a hydrophobic part can spontaneously adsorb on a hydrophobic surface. The simplest model that describes this phenomenon is Langmuir adsorption. However, experimentally, deviation from this ideal adsorption model can be found.

In this chapter, I present the theory of adsorption including some special cases, such as the presence of an large number of adsorption sites and mass transport-limited adsorption. I present the characterization of the interaction between small pollutant molecules, such as surfactants with various charges, an alkane (hexane) and a biomolecule (lysozyme), and a hydrophobic fluorinated material, performed with the *Reflective Phantom Interface* method. I show that the planar sensing surface enables extraction of the equilibrium constant for adsorption, even in the case of depletion of analytes in solution.

This label-free detection method provides direct access to the kinetics of adsorption. I find that the three classes of molecules escribed above behave very differently. The concentrations yielding half-coverage of the surface differ by orders of magnitudes, as do the characteristic times for adsorption. Surprisingly, all the studied surfactants display similar behavior, despite the different net charge and structure. The lysozyme has a stronger interaction with the surface and faster adsorption kinetics relative to the surfactants, whereas hexane interacts weakly and more slowly. Remarkably, once the effects of mass limitation and transport are considered through a suitable analytical model, rather simple and general scaling rules with molecular size are obtained. Studying adsorption on a planar surface is necessary to obtain the interaction constants that will be later used to study more complex substrates, namely micro-porous membranes. Finally, I present preliminary detection results obtained with the RPI approach on real water samples, taken from the river Lambro, and the first test of surface functionalization in order to confer selectivity to the process of surfactants adsorption. The content of this chapter is the topic of a paper: ”Selective adsorption on fluorinated plastic enables the optical detection of molecular pollutants in water”, R. Lanfranco, F. Giavazzi, M. Salina, G. Tagliabue, E. Di Nicoló , T. Bellini and M. Buscaglia, submitted.

5.1 Characterization of fluorinated material

To quantify the number of molecules adsorbing onto the prism surface, it is necessary to determine the refractive index of the RI-matched plastic. This was obtained by performing reflectivity measurements for various solvent compositions. In particular, I used different mixtures of water-glycerol to change the solvent's refractive index. The water-glycerol refractive index was measured by means of an Abbe refractometer. As shown in **Figure 5.1**, the surface reflectivity has a parabolic dependence as a function of the solvent refractive index. By fitting these data, the refractive index at which the reflectivity is minimum was obtained, corresponding to the refractive index of the Hyflon AD® prism. From the data reported in **Figure 5.1** the refractive index of the prism was determined to be $n_h = 1.3279 \pm 0.0003$.

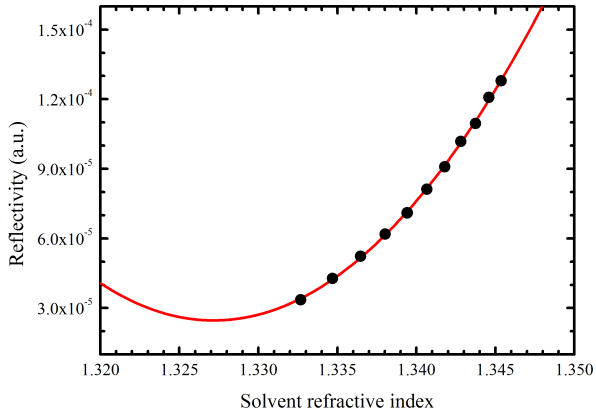

Figure 5.1: Reflectivity of the liquid/prism interface as a function of the refractive index od the liquid: the black points are the experimental data and the red line is a parabolic fit, from which the prism's refractive index is extracted.

5.2 Adsorption model

The theoretical framework for this investigation was provided by the Langmuir model [53], arguably the simplest adsorption model, which is based on the following assumptions:

- the adsorbing surface is homogeneous;
- all the adsorbing sites are energetically equivalent;
- each site can hold at most one molecule, meaning that only mono-layer coverage is allowed;
- there are no interaction between adsorbate molecules on adjacent sites.

The adsorption process can be easily represented by this balanced equation $[M] + [S] \rightleftarrows [MS]$, where $[M]$ indicates the concentration of the free molecule, $[S]$ the total

concentration of free binding sites and $[MS]$ is the adsorbed (filled) site concentration. In this approach, there are two characteristic speeds: the speed of adsorption, $v_{on} = k_{on}\ [M]\,[S]$, and the speed of desorption, $v_{off} = k_{off}\ [MS]$, where k_{on} and k_{off} are adsorption and desorption rates, respectively. The ratio of these two rates is the desorption equilibrium constant: $K_D = \frac{k_{off}}{k_{on}}$. If I introduce the ratio of occupied sites, $\varphi = \frac{[MS]}{[S]+[MS\}}$, the relation that describe the variation in time of ϕ is:

$$\frac{d\varphi}{dt} = v_{on} - v_{off} = k_{on} C_0\,(1-\varphi) - k_{off}\varphi \tag{5.1}$$

The molecular concentration in the bulk, C_0, in the simplest scheme is constant throughout the process; this is the case of an infinite reservoir of molecules. If this reservoir is not infinity, we must account for the variation of concentration during the adsorption process. Concentration is not longer constant but varies in the following manner:

$$C = C_0 - \varphi\,\frac{N_S}{V} \tag{5.2}$$

where C_0 is the total molar concentration in the cuvette and V the volume of the liquid phase, and thus the term N_S/V represents the volume concentration of binding sites in the cuvette, [S], and $\varphi\,\frac{N_S}{V}$ represents the volume concentration of molecules adsorbed onto the surface. Since the adsorption process is substantially governed by the concentration of available analytes in solution *C*, in principle, can vary by changing either the concentration C_0 in the cuvette or by changing the liquid volume V at some fixed concentration. Substituting Equation 5.2 into 5.1, the variation of binding sites in the case of a limited number of analyte molecule in solution, becomes:

$$\frac{d\varphi}{dt} = v_{on} - v_{off} = k_{on}\left(C_0 - \varphi\,\frac{N_S}{V}\right)(1-\varphi) - k_{off}\varphi \tag{5.3}$$

Solving this equation at the equilibrium, $\frac{d\varphi}{dt} = 0$, the Langmuir Isotherm in the limit of mass limitation can be written:

$$\varphi_{eq} = \frac{V\ (C_0 + K_{eq}) + N_S - \sqrt{(V\ (C_0 + K_{eq}) + N_S)^2 - 4\,V\,N_S\,C_0}}{2\,N_S} \tag{5.4}$$

The fraction of binding sites at equilibrium depends both on the concentration and on the sample volume, so it is possible to observe adsorption by increasing either the molecular concentration or the sample volume. From Equation 5.4, the concentration at which half of the binding sites are occupied is $C_{\frac{1}{2}} = K_D + \frac{N_S}{2V}$.

The time-dependent solution of 5.3 takes the form of a hyperbolic tangent, which, in practice, differs only slightly from single exponential behavior for all conditions of interest in this study. This is because the coefficient of the term linear in φ is always larger than that of the quadratic one. Therefore, it follows that fitting the experimental adsorption curves with single exponential functions offers a good approximation and provides a robust approach to extract φ_{eq} as well as the kinetic parameters of the process, as discussed in Sections 5.4 and 5.5.

5.3 Adsorption of different molecules studied with RPI

Mechanical machining, printing and molding are common approaches for plastic manufacturing, including application to fluorinated polymers. Prisms of Hyflon AD® (*Solvay*

Specialty Polymers, Bollate, Italy) were previously produced by cutting and polishing and utilized for optical bio-sensing applications [15]. In the present work, I used a similar prism without any surface coating or functionalization in order to detect and quantify the spontaneous adsorption of molecules on the prism's planar surface. The prism was inserted in a 1-cm cuvette as show in **Figure 5.2**. When immersed in water, the prism became barely visible. The adsorption of molecules with refractive index different from that of water, sketch of **Figure 5.2**, provided a clear increase of reflected light intensity that was measured by a simple optical set-up that is formed using only a few components, **Figure 5.2**: a He-Ne laser, a square glass cuvette into which the right-angle Hyflon AD® prism is placed and a photodiode that collects the reflected light.

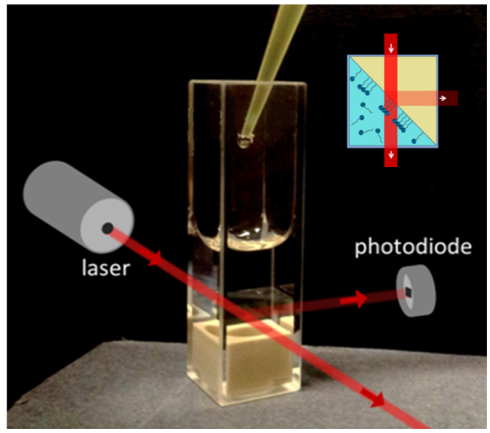

Figure 5.2: Photograph of the measuring cell of the RPI apparatus. The Hyflon AD® prism is placed inside the cell on top of a holder, inside of which is a magnetic stir bar. In the sketch, a schematic representation of adsorption within the cell is shown.

Molecular compounds with refractive indices as low as that of water are rare and they are almost all fluorinated. Therefore, a very large variety of molecules can adsorb on these fluorinated surfaces and yield an optical signal, in principle. Typically, spontaneous adsorption onto fluorinated surfaces is mediated by hydrophobic interactions, although ionic forces may also play a role. Amphiphilic compounds represent a suitable class of molecules to test the optical response to spontaneous adsorption. In this work, I explore the interactions between different types of surfactants and the bare hydrophobic Hyflon AD® surface. In particular, I studied the anionic surfactant SDS, the cationic surfactant benzyldimethylstearylammonium chloride monohydrate SBSAC and non-ionic Tween 20, all provided by Sigma Aldrich. Moreover, I investigated how the behavior of these amphiphilic molecules differs from a protein (lysozyme) and an alkane (hexane). The characteristics of these molecules are reported in **Table 5.3**, **Figure 5.3**. To reproduce in laboratory the typical salinity of river water, I performed experiments in a saline buffer (0,049 mM magnesium chloride, 0,09 mM calcium chloride, 1 mM phosphate buffer, 0.27 mM potassium chloride and 13,7 mM sodium chloride) and also with MilliQ ® water.

Figure 5.4A reports the intensity of reflected light measured after the addition to solution of increasing concentrations of the cationic surfactant SBSAC. The data are for the equilibrium value of reflectivity measured about 500 s after the addition. A continuous increase of reflectivity was observed until saturation was reached at high concentration, corresponding to full coverage of the prism surface.

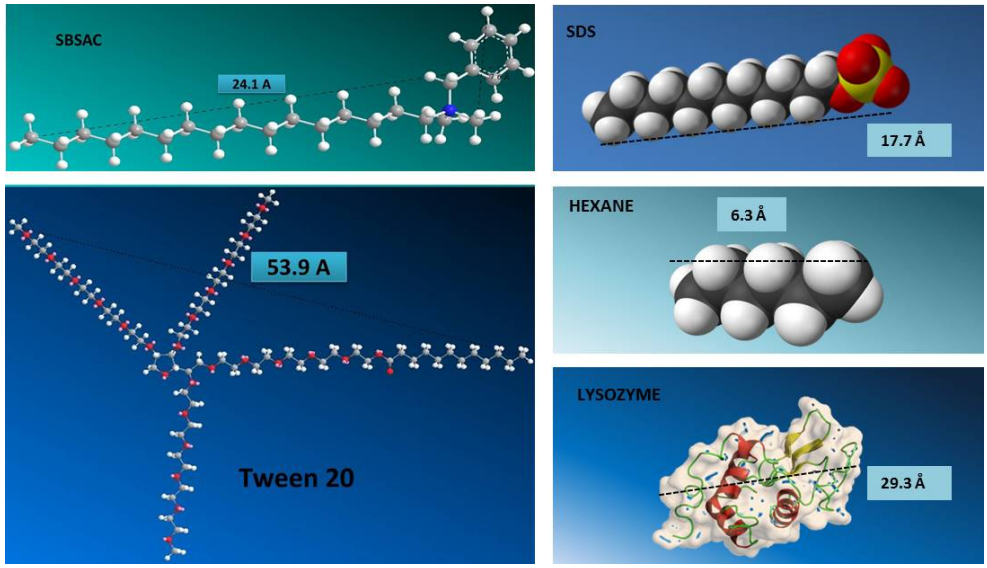

Figure 5.3: Representation of the studied molecule with *ChemBio3D* program. The typical lengths of the molecules are reported within the figure.

Because this thin molecular layer has a refractive index different from both the substrate (1.327) and the acqueous solution (1.334), the reflectivity *R* of the surface is higher than the bare surface. In particular, if I add successively increasing concentrations of a cationic surfactant inside the measuring cell, the reflectivity increases in time, as in **Figure 5.4A**. The maximum amplitude at each concentration and the characteristic rise time depend on the surfactant concentration within the measurement cell, in accord with the Langmuir adsorption process. When the reflectivity, at high concentration, does not grow anymore, adsorption is supposed to end. This reflectivity can be converted in an effective layer thickness: $h = h_0\sqrt{\frac{R-R_0}{R_0}}$, **Figure 5.4B**. Moreover, knowing the density of the adsorbed molecules ρ, it is possible to convert this effective thickness h into a surface density of adsorbed molecules, $\sigma = \rho h$, and so it is possible to estimate the maximum adsorbed mass density on the surface.

At each successive surfactant addiction to the cell, the signal rises, meaning that the molecular mass density is increasing. Each of these increases can be fitted to a negatively growing exponential $\Delta h = \Delta h_{max}(1 - e^{-\frac{t}{T_c}})$, from which I can extract two parameters: the maximum adsorbed density $\Delta h_{max}$and the characteristic rise time T_c. In this way, I can study separately the equilibrium and the kinetics of adsorption.

It is experimentally observed that, in experiments at fixed concentrations, increasing only the volume inside the cuvette causes the reflectivity to grow, meaning that adsorption occurs on the surface, **Figure 5.4C** and **5.4D**. This happens because, in the measurement cell configuration, there is a large number of binding sites, despite the large volume [58]. Also, these adsorption curves display exponential behavior so I can extract again Δh_{max} and T_c, which, in this case, depend on the volume within the cell. The equilibrium and the kinetics of adsorption are in agreement with the Langmuir behavior with mass limitation, as expressed by Eq. 5.4.

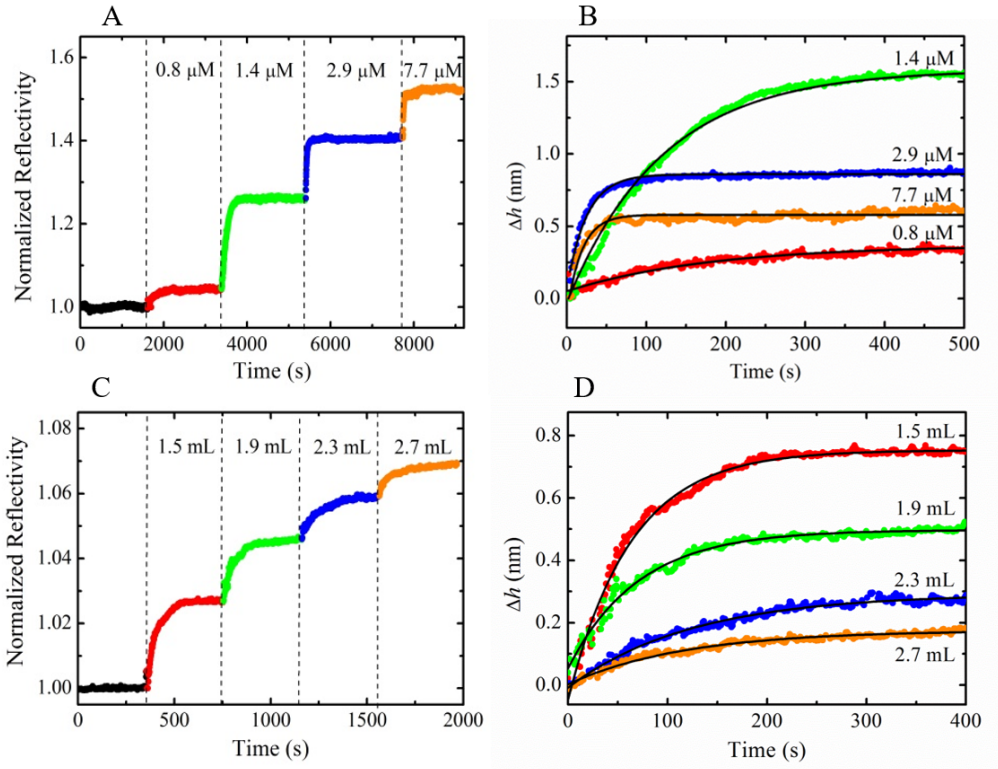

Figure 5.4: Experimental reflectivity measurements with RPI apparatus of the SBSAC adsorption from MilliQ water. A) Normalized reflectivity $R_n = (R - R_0)/R_0$ as a function of time with increasing surfactant concentration inside the cell, shown in the graph. These adsorption data were converted into thickness h using $h = h_0\sqrt{\frac{R-R_0}{R_0}}$ and fitted with a decreasing exponential (black lines in B). C) Normalized reflectivity as a function of time with increasing volumes inside the cell, shown in the graph, at a fixed concentration equal to 1.92 μM. In D the conversion to h is reported along with a fit to a decreasing exponential (black lines).

5.4 Equilibrium constant and mass limitation effect

Similarly to what performed in the case of SBSAC, the saturation values of h extracted about 500 s after the addition of the analyte in cuvette provided a measurement of the equilibrium thickness of the adsorbed layer h_{eq}, reached for a particular concentration C_0 and for a total amount of molecules C_0V. **Figure 5.5A** and inset report the values of $h_{eq}(C_0, V)$ for the different molecules considered. By increasing the concentration C_0 or the volume V at fixed concentration, the tested molecules generally showed a saturation of the adsorption. Remarkably, the different classes of molecules displayed very different behaviors. The protein lysozyme displayed a response at concentrations much smaller than surfactants, whereas hexane provided a detectable signal at much higher concentrations.

For each molecule, the adsorption curve as a function of C_0 and V were concomitantly fitted using Equation 5.4 and the parameters K_D, N_s and h_{max} were obtained.

The results are reported in Table 5.4. In particular, the obtained K_D values are in agreement with the typical equilibrium constants reported for similar surfactants adsorbing on solid surfaces 1citeSurf. The behaviors of the cationic and non-ionic surfactants were very similar. Surprisingly, also the anionic surfactant in saline buffer presented values of K_D and N_s similar to the other surfactants, despite the lower thickness h_{max} at saturation. These results suggest that the intrinsic affinity of surfactants for the perfluorinated surface does not depend directly on the net-charge of the hydrophilic head, at least in saline buffer. Additionally, these results indicate that, in general, different molecular structures can yield to very similar interaction with the surface. On the other hand, lysozyme and hexane displayed very different affinities and numbers of binding sites on the surface: the values of K_D and N_s were order of magnitudes different from those of surfactants. In particular, the protein had a higher affinity (lower value of K_D) and fewer binding sites, whereas hexane had a lower affinity and many more adsorption sites. In all cases, it was found that $N_s/V > K_D$, hence confirming that the adsorption process was affected by mass limitation.

We observe that, for all the studied surfactants and the protein, these values are comparable with the size of the molecules, estimated with *ChemBioDraw 3D*. This indicated the formation of a molecular monolayer at the perfluoropolymer-water interface. For surfactants, the thickness of the adsorption layer also indicated a rather oriented structure of the amphiphilic molecules, which substantially stood on the surface, facing the hydrophobic group toward the plastic material. This interpretation is coherent to other experimental observations of surfactant adsorptions on hydrophobic surfaces made by different experimental approaches for concentrations below the CMC [59] [60]. The anionic SDS represented an exception because the lower value of h_{max} relative to the molecular size indicated a lower degree of packing relative to the other surfactants. The observed behavior of hexane was different from those of the other molecules examined here: the maximum thickness extrapolated at high concentrations was not compatible with a single molecular layer. Therefore, the formation of multiple layers was assumed. In the following, the thickness of the corresponding monolayer of hexane is derived from the expected geometric packing (Table 5.4)

A useful parameter to interpret the different values of adsorption affinities is represented by the contact area per molecule A_{mol} on the surface. In general, stronger interactions are expected for higher numbers of surface interacting sites per molecule. For instance, it has been observed that larger proteins tend to stick to various kinds of surfaces, whereas smaller ones only adsorbs on interfaces with lower wettability [61]. For the studied molecules, the values of A_{mol} was obtained as $A_{mol} = V_{mol}/h_{max}$, where V_{mol} is the molecular volume estimated either as the molecular mass divided by the density or from the molecular structure. Remarkably, despite the differences in terms of net charge and geometry, the obtained contact area was similar for all the considered surfactants, being in the range 0.7-1.0 nm^2. This result is in agreement with the maximum packing obtained from geometrical constraints that was estimated to be in the range 0.8-1.2 nm^2. As expected, the surface contact areas for lysozyme and hexane were very different from those of surfactants. From the adsorption of the protein, a value of 7.75 nm^2 was obtained, which was consistent with the expected packing of the folded molecule onto the surface. Differently, the average contact area per hexane molecule was found to be 0.06 nm^2, significantly smaller than the estimated geometrical packing of 0.31 nm^2, in agreement with the hypothesis of the formation of a molecular multilayer onto the surface, as also derived from the analysis of the thickness of the adsorbed layer.

The experimental observations indicated that the equilibrium constant for adsorp-

tion/desorption on the perfluorinated surface does not depend on the net charge of surfactants and does depend on the class of the molecule (i.e. alkane vs surfactant vs protein). On the basis of these results, I tested the consistency of a simple model for molecular adsorption on the perfluorinated surface. I assumed that only the hydrophobic components of the molecules adhere to the surface and that all the hydrophobic interactions have all the same strength per unit surface. With these assumptions, a linear scaling of the binding free energy with the hydrophobic portion A_h of the molecular contact area A_{mol} is expected. In the case of hexane and all the surfactants, the measured contact area Amol was all ascribed to hydrophobic moieties, therefore$A_h = A_{mol}$. Differently, only a fraction of the amino acids composing the protein lysozyme could be considered hydrophobic. Accordingly, in this case I assumed $A_h = f_h * A_{mol}$, where $f_h = 0.28$, was obtained as the fraction of hydrophobic residues (W, F, Y, L, I, C, M) over the entire protein sequence [62]. **Figure 5.5B** reports the measured value of the equilibrium constant for adsorption $1/K_D$ as a function of A_h. Remarkably, despite the diversity of the analyte molecules considered, a scaling of $log(1/K_D)$ with A_h was observed. From this dependence, I derived a free energy increment for molecular adsorption of about –1.83 kcal $\frac{1}{mol^1 nm^2}$. This value is in agreement with the adsorption free energy per hydrocarbon unit reported in previous works, which typically is in the range 0.2-0.6 kcal mol^{-1} [63] [64]. Moreover, the estimated adsorption strength is coherent with the reported free energy of hydrophobic interactions among amino acids [62]. Overall, these observations are in agreement with the hypothesis of a relevant contribution of the hydrophobic contact area to the adsorption free energy on the perfluorinated surface and suggest the validity of this approach to predict the surface binding affinity from the molecular size and structure.

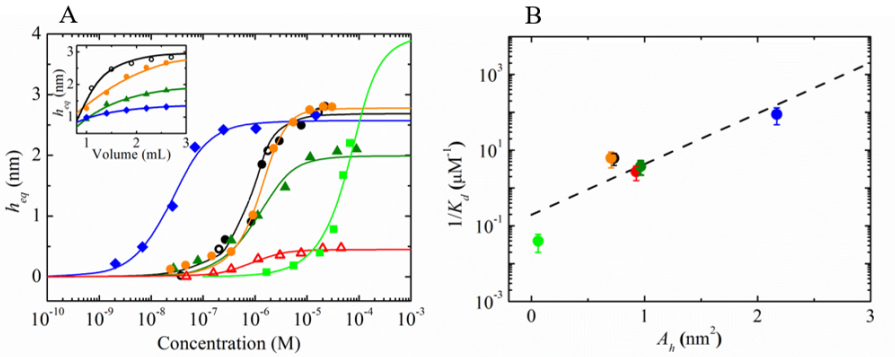

Figure 5.5: Equilibrium of molecular adsorption on the perfluorinated surface. The layer's thickness at equilibrium h_{eq} is reported for various concentrations of SBSAC in deionized water (black open circles) and in saline buffer (orange full circles), Tween20 in saline buffer (green full triangles), SDS (red open triangles), lysozyme (blue full diamond) and hexane (light green square). The lines of the corresponding colors represent fits to the Langmuir adsorption model with mass limitation. Inset: h_{eq} measured as a function of sample volume at fixed concentration (SBSAC in deionized water: 1.92 μM; SBSAC in saline buffer: 1.08 μM: Tween 20: 1.62 μM; lysozyme: 19.3 nM). The color code is the same as in the main panel. (B) Value of the equilibrium adsorption constant $1/K_D$ extracted from a fit of the data in panel A as a function of the hydrophobic molecular contact area A_h on the perfluorinated surface for each molecule. The color code is the same as in panel A. The black line represents a fit to the data to the function $log_{10}(1/K_D) = C_1 + C_2 A_h$, where $C1 = 5.29(\pm 0.42)$ and $C2 = 1.34(\pm 0.37) nm^{-2}$

Table 5.1: Characteristics of the studied molecules.

molecule	MW (Da)	CMC (mM)	$\rho(g/mL)$	n	D (10^{-6}cm$^2/s$)	h_0(nm)
SBSAC	442.15	0.34 MQ- 0.13 b	0.376	1.435	4	3.15
Tween 20	1227.54	0.3 b	1.1	1.469	1	2.35
SDS	288.37	0.54 b	1.01	1.461	1.76	2.49
Lysozyme	14000	-	1.2	1.5	1.1	1.89
Hexane	86.18	-	0.655	1.373	2.3	8.39

Molecular mass, (MW), Critical Micellar Concentration (CMC) measured with conductivity experiments, density ρ, diffusion coefficients, taken from [54], [55] [56] [57] and the calculated value of h_0 with equation reported in Table 3.3 for each molecule.

Table 5.2: Adsorption parameters obtain from the study of the adsorption.

molecule	h_{mol} (nm)	h_{max}(m)	A_{max} (nm^2)	K_D (nM)	N_S (nmol)	k_{on} (M^{-1}ms^{-1})	k_{off} (ks^{-1})
SBSAC MQ	2.41	2.68	0.73	165	2.17	4.43	0.7
SBSAC b	2.41	2.77	0.70	163	2.79	3.51	0.57
Tween 20	2.0	1.99	0.93	372	2.33	1.86	0.69
SDS	1.77	0.45	0.97	270	1.33	8.5	2.3
Lysozyme	2.93	2.57	7.75	11.3	3.08 10^{-2}	107.2	1.21
Hexane	0.78	3.98	0.06	>25200	185	<0.013	0.33

5.5 Kinetics of transport and adsorption

The time behavior of the adsorption process is described by $\varphi(t)$ through Equation 5.3. As in the case of the equilibrium analysis, the calculated adsorption curves as a function of time depended on both concentration and volume, because of the finite number of molecules in the cuvette. The dependence of the measured adsorption rate Γ on the sample volume V at fixed concentration was experimentally confirmed, as reported in the inset of **Figure 5.6A**. In general, as discussed above, the time-dependent solutions of Equation 5.3 are not exponential functions. However, in practice, they differ only slightly from exponential behavior. Therefore, in order to compare the measured adsorption rates with those predicted by the model, I calculated effective adsorption rates from Equation 5.3. I considered the initial, linear growth of adsorption after a concentration increase. In the case of exponential growth with amplitude φ_{eq} and rate Γ, the initial slope is given by the product $\varphi_{eq} * \Gamma$. On the other hand, according to Equation 5.3, the initial slope of $\varphi(t)$ is always equal to $k_{on}C_0$. Accordingly, I modeled the rate of adsorption as

$$\Gamma = \frac{k_{on}\, C_0}{\varphi_{eq}} \tag{5.5}$$

where φ_{eq} is given by Equation 5.4. In the case of negligible mass limitation, that is for $Ns/V \ll Kd$, the rates assume the simpler analytical form $\Gamma = k_{on}C_0 + k_{off}$. More generally, the expression of Γ becomes simple for very small and very large values of the analyte concentration C_0 relatively to $C_{\frac{1}{2}}$, and for $C_0 = C_{\frac{1}{2}}$. In these limits, $\Gamma = k_{on}(N_s/V) + k_{off}$, $\Gamma = k_{on}C_0$, and $\Gamma = k_{on}(N_s/V) + 2k_{off}$, respectively. Importantly, for sufficiently large analyte concentrations, the adsorption rate is always given by $k_{on}C_0$, and, therefore, it is not affected by mass limitation. This allowed us to directly extract the apparent kinetic constant for adsorption k_{on} from the slope of the measured rate $\Gamma(C_0)$ for the largest concentrations. In practice, the data reported in **Figure 5.6B** and **5.6D** were fitted using Equation 5.5, constraining the values of N_s and $K_D = \frac{k_{off}}{k_{on}}$ to those previously extracted from the study of the equilibrium data, **Table 5.4**. In this way, only one free parameter (either k_{on} or k_{off}) was determined by the fit. The obtained fitting curves are reported in **Figure 5.6A** and inset, and the values of k_{on} and k_{off} are reported in **Table 5.4**. The desorption kinetic constant k_{off} was rather similar for the three surfactants and the protein, whereas the kinetic constant for adsorption was much faster for the protein. Both kinetic constants extrapolated for hexane were much lower than those of the other molecules, as expected from the small values of the measured adsorption rates $\Gamma(C_0)$.

In analogy to the case of ligand-receptor binding, the observed adsorption and desorption process can be affected by the transport of analyte molecules from the bulk solution to the sensing surface [65]. This condition occurs when the mixing of molecules in the proximity of the surface is not fast relative to the intrinsic kinetics for molecular binding. Processes characterized by more rapid binding kinetics are more prone to be affected by such transport limitation effect. Importantly, the adsorption kinetics measured in this study were much faster than what typically observed for specific antibody-antigen binding performed with a similar measuring system [15] . Therefore, transport phenomena were expected to play a more relevant role in the observed adsorption kinetics. An indication of the relevance of the transport limitation on the adsorption rates measured in this study was provided by the dependence of the adsorption kinetics on the stirring speed. As shown in the inset of **Figure 5.6B**, the measured adsorption rates

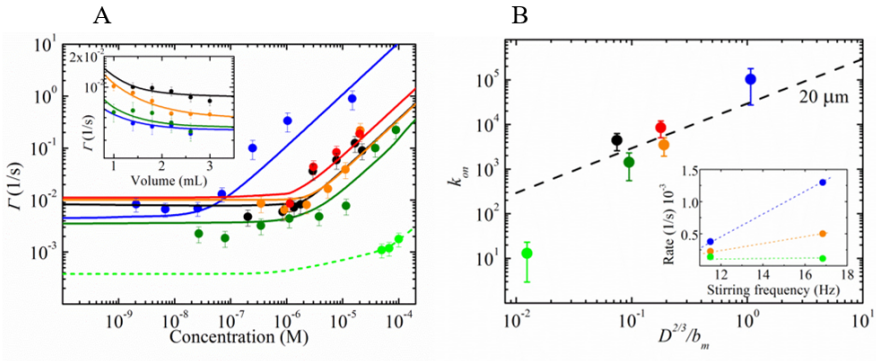

Figure 5.6: Kinetics of molecular adsorption on the perfluorinated surface. The rates Γ extracted from the exponential fit of the adsorption curves is reported as a function of the concentration of SBSAC in deionized water (black open circles) and in saline buffer (orange full circles), Tween20 in saline buffer (green full triangles), SDS (red open triangles), lysozyme (blue full diamond) and hexane (light green square). The lines of corresponding colors represent fits to linear dependence on C0. Inset: Γ measured as a function of the sample volume at fixed concentration (SBSAC in deionized water: 1.92 μM; SBSAC in saline buffer: 1.08 μM: Tween 20: 1.62 μM; lysozyme: 19.3 nM). The color code is the same as in the main panel. (B) Value of the observed kinetic constant for adsorption k_{on} as a function of $D^{2/3}/b_m$. The dashed line represent the expected behavior for a constant depletion layer of 20 μm . Inset: dependence of the measured adsorption rate on the stirring velocity at fixed concentration of SBSAC in saline buffer (orange, C_0 = 3.3 μM), lysozyme (blue, C_0 = 71 nM) and hexane (light green, C_0 = 55.6 μM).

of hexane were almost insensitive to the rotational speed of the stirrer, whereas those of SBSAC surfactant and lysozyme strongly depended on it. This indicated a more relevant contribution of transport limitation for the surfactants and the protein. In general, binding or adsorption processes can be characterized by intrinsic kinetic constants k^i_{on} and k^i_{off} that depend on the detailed interactions between the analyte molecules and the surface. Only in the case of sufficiently fast transport of molecules (i.e., fast flow and mixing near the surface), k^i_{on} and k^i_{off} are equal to the observed kinetic constants k_{on} and k_{off}, respectively. More generally, the transport process may affect somewhat both the observed kinetic constants k_{on} and k_{off} in the same way. In the case of adsorption, the transport contribution may play a non-negligible role even for high flow rates, because of the high densities of binding sites on the surface. This is, in fact, a necessary condition for non-specific adsorption processes. In the experimental set-up employed here, the use of a magnetic stir bar provided the advantage of rather efficient mixing of a relatively large volume of solution, approaching the turbulent regime at the highest stirring rates. Nevertheless, extremely large, and substantially impractical flow rates or stirring speeds may be required to reduce the effect of transport limitations in the case of large densities of surface binding sites. In the case of a fully transport-limited process, a rather thick layer of fluid in contact with the surface could have a lower concentration of analyte relative to the bulk solution and the measured rate could therefore be limited by the diffusion time across such a depletion layer. The thickness δ of the depletion zone depends on the flux close to the surface, on the geometry of the measuring cell and on the free diffusion of the studied molecule. The value of δ can be estimated as in [65]:

$$\delta = \sqrt[3]{\frac{LD}{\gamma}} \tag{5.6}$$

where L is the length of the adsorption area of the sensor along the flow direction, $\gamma^{\bullet}$ is the derivative of the flux normal to the surface and D is the diffusion coefficient of the molecule. In general, transport limitation of the observed kinetics are more relevant for larger values of δ. However, according to Equation 5.6, δ scales only with the cube root of the flow parameter $\gamma^{\bullet}$.

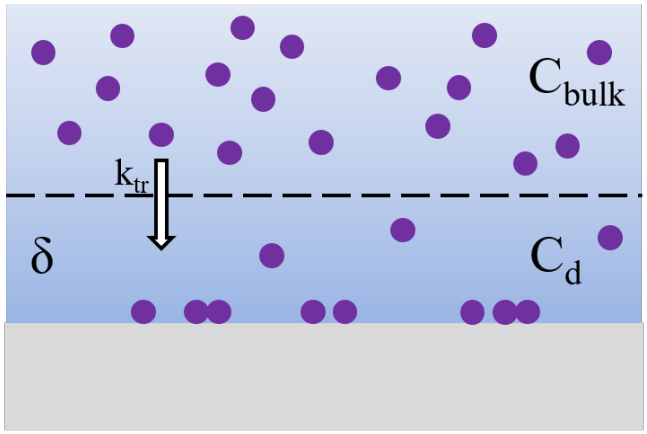

Figure 5.7: Schematic representation of the two compartment model. Inside the depletion layer δ the concentration C_d is lower with respect the bulk concentration C_{bulk} because of the rapid adsorption at the interface. A concentration gradient is present and so a mass transport, regulated by the flow rate k_{tr}, occurs between these two compartments.

A common approach to compute the effect of transport on the observed kinetic rates is to consider two regions (i.e., two compartments, **Figure 5.7**): the depletion layer and the rest of the sample volume. The two compartments have two spatially uniform concentrations, $C_d(t)$ and $C_{bulk}(t)$, respectively [66]. Using this approximation, the adsorption process was again modeled by Equation 5.3 with the substitution $C_0 = C_d$, and with the value of C_d provided by the diffusive equilibrium between the two compartments. Considering an initial condition without analyte molecules in the cuvette and a sudden increase of concentration from zero to C_{bulk}, for a negligible value of δ the initial flux of molecules toward the surface is given by $J^{kin} = k^i_{on} C_{bulk} b_m$, where b_m represents the surface density of available binding sites. At the other extreme, a purely diffusive flux is given by $J^{diff} = DC_{bulk}/\delta$, according to Fick's first law of diffusion. The ratio $Da = J^{kin}/J^{diff}$ is known as the Damkohler number and its value indicates to what extent the observed kinetics is affected by the transport process [65] [67]. In general, the measured characteristic time $\tau_{obs} = 1/\Gamma$ for a binding process on a surface differs from the intrinsic molecular interaction time $\tau_R = (k^i_{on} C_0 + k^i_{off})^{-1}$ according to:

$$\tau_{obs} = (1 + Da)\tau_R \tag{5.7}$$

In the case of pronounced transport limitation ($Da >> 1$) and for $C_0 >> C_{\frac{1}{2}}$, from the above definition of Da I derived $\Gamma = k^{tl}_{on} lC$, where

$$k^{tl}_{on} = \frac{D}{\delta b_m} \tag{5.8}$$

Accordingly, the value of the apparent kinetic constant for binding is in the range ${k_{on}}^{tl} < k_{on} < k^i_{on}$.

In order to investigate the dependence of the observed adsorption kinetics on molecular properties, I focused on the limiting case of a fully transport-limited process. Substituting the expression of δ given in Equation 5.6 into Equation 5.8, the terms that depend on the cuvette geometry and flow, but not on the properties of the molecular analyte, were grouped in the parameter $F = (\frac{\gamma}{L})^{1/3}$, thus leading to

$$k_{on}^{tl} = F \frac{D^{\frac{2}{3}}}{b_m} \tag{5.9}$$

Similar equations for the transport-limited rate are often encountered in studies of sensors in micro-fluidic cell formats [67]. Here I generalized the model to the cuvette-based cell and focused on the two parameters that depend on the specific adsorbing molecule, namely D and b_m. **Figure 5.6B** reports the measured values of k_{on} as a function of the parameter $\frac{D^{2/3}}{b_m}$. The dashed line indicates the expected scaling for a fully transport-limited case, assuming $\delta = 20\mu m$. This represents an upper limit for the value of δ, obtained assuming that $k_{on} = k_{on}^{tl}$ and taking as the value of b_m the reciprocal of the molecular contact area onto the surface, $1/A_{mol}$. In practice, this is the largest value of δ consistent with the measured values of k_{on} for all the surfactants and the lysozyme. **Figure 5.6B** shows that the kinetic rates for adsorption measured for the surfactants and the protein were consistent with the dependence indicated in Equation 5.9, whereas hexane did not follow the same scaling. Consequently, the measured kinetics of the surfactants and the protein were in agreement with the expected behavior in the case of a fully transport-limited regime. In contrast, the slower adsorption rates of hexane showed that transport was not the limiting process in this case, and the observed k_{on} was actually ascribed to the molecule-surface interaction. Remarkably, the scaling indicated by Equation 5.9 provided a tool to quantitatively discriminate among the adsorption kinetics of different molecules. In practice, both terms D and b_m of Equation 5.9 scaled with the size of the analyte, either through its hydrodynamic radius or the contact area onto the sensing surface, respectively. As reported above, the strength of the adsorption interaction at equilibrium was found to scale with the hydrophobic contact area of the molecule. Here I linked the observed transport-limited kinetics to other parameters derived from the molecular size. Overall, these results indicated that the measurement of the spontaneous adsorption of molecules onto Hyflon AD® surfaces can enable detection of multiple classes of molecules in solution and their discrimination on the basis of their size and hydrophobicity.

5.6 Test with real river water samples

As a preliminary test, I collected and examined two samples of water from a river that flows through the city of Milan (Italy), the Lambro river. The two samples were taken upstream (SU) and downstream (SD) of the city. They were centrifuged to separate particulates and then filtered with a PTFE 0.2 μm Millipore filter. The addition of the resulting water samples to the measuring cell produced an increment of the reflectivity signal, as shown in **Figure 5.8A**. The SD sample yielded a higher signal that the SU one, hence indicating a larger amount of molecules adsorbing onto the sensing surface. The reflectivity signal was converted into the normalized surface density, using as h_0 the average of the values extracted for the three surfactants studied in this work. In this way, the SU and SD samples were directly compared to the equilibrium and kinetic behavior modeled for the studied surfactants, as shown in **Figure 5.8B** and **5.8C**, respectively. The observed amplitudes and rates of the adsorption curves of the SU and SD samples are both compatible with a surfactant concentration between 0.4 μM (SU) and 0.7 μM (SD). This test demonstrate the feasibility of a sensitive detection system for monitoring molecular contaminant of water [26].

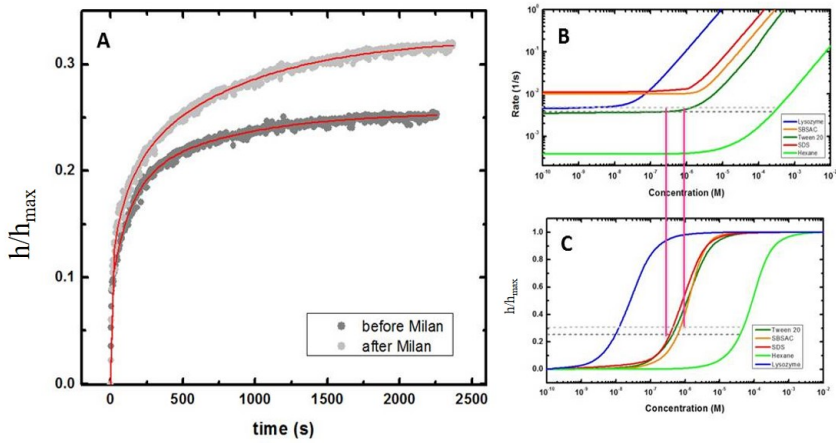

Figure 5.8: Adsorption tests with river water sample. (A) Adsorption curves of SU (dark gray) and SD (light gray) samples. Comparison of the adsorption rates of SU (dark gray dashed line) and SD (light gray dashed line) samples with the kinetics (B) and the normalized adsorption surface density at equilibrium (C) for the different molecular models presented here. In panel (B) and (C), the curve color refers to SBSAC in saline buffer (orange), Tween20 (dark green), SDS (red), hexane (light green), Lysozyme (blue).

5.7 Surface functionalization tests

In order to distinguish the different classes of surfactants (cationic from anionic from non-ionic), it is necessary to change some property of the fluorinated surface, for instance its charge. An effective means to alter the properties of the sensing surface is by functionalization. To perform such studies, it is necessary to directly compare surfactant adsorption on the bare surface to the treated one. Using the experimental apparatus presented in [15], it is possible to directly visualize the Hyflon AD® surface. I therefore used that experimental apparatus to directly visualize the Hyflon AD® prism surface, treated with half-coating (meaning that only half of the prism surface was functionalized), pro-

duced by a dipping procedure, **Figure 5.9A** and **5.9B**. The first half-coating consisted iof dimethylacrylamide (DMA), N-acryloyloxysuccinimide (NAS), and 3-(trimethoxysilyl) propyl methacrylate (MAPS) - copoly(DMA-NAS-MAPS). I observed that the functionalized substrate does not affect the affinity of surfactants, **Figure 5.9C**, although; the adsorbed surface density is lower in the presence of the DMA coating than with the bare surface. Further coatings will be studied to obtain selective surfactant detection.

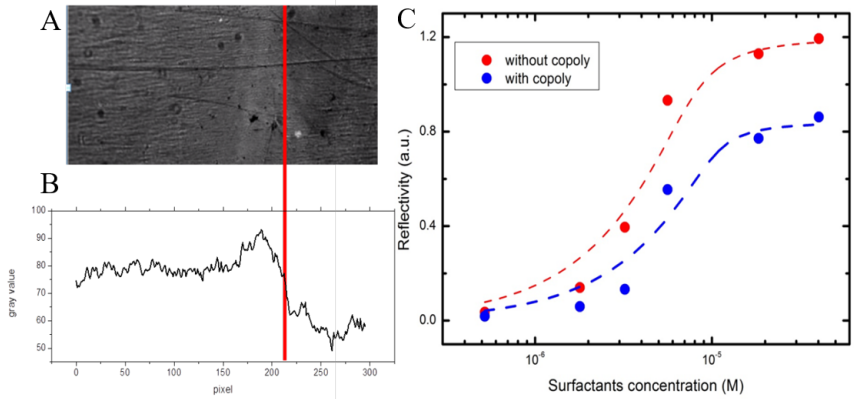

Figure 5.9: A) Image of the Hyflon AD® surface: the red line indicates the border between the zone without copoly functionalization (on the right), characterized by less reflectivity, and the functionalized part (on the left), that resuls int brighter reflection using the intensity profile reported in B). C) Equilibrium behavior of these two different zones. The only difference is the plateau value reached at high surfactant concentrations, indicating that the functionalization blocks some of the adsorption sites. I do not notice any difference in the affinity constant (the concentration at which the signal shows an inflection point), meaning that the surface treatment does not affect the interaction. Experiments were performed with the cationic surfactant SBSAC.

Chapter 6:
Optical characterization of invisible porous media and molecular adsorption experiments

In this chapter, optical experiments performed with different samples of commercial and newly fabricated Hyflon AD® membranes are presented. The study of small angle scattered light intensity by porous membranes was already be proposed in literature to obtain information about internal morphology of porous filters [68] [69] [70]. I used two different approaches to measure the light scattering signal: a conventional static light scattering instrument, where turbidity and scattered light intensity at a fixed angle are simultaneously measured, and a novel method based on the analysis of images acquired by an optical microscope. The latter approach was implemented because it could be an easier and faster technique to study index-matched porous media. It is shown that membranes with different internal morphology have different optical responses, both in scattering and in microscopy experiments, as the RTS model presented in Section 3.4 states. With regard to surfactant adsorption, we analyzed the experimental measurements with both of our models: R-G, Section 3.3, and RTS, Section 3.4. Using the R-G model enables determination of the thickness of the adsorbed surfactant layer, which, surprisingly, is comparable to the result from the RPI approach. Then, using the RTS model in the presence of a layer on the membrane surface, we can find the mean pore dimensions, the results indicating larger values than those obtained with most common techniques presented previously, such as SEM images or nitrogen flow measurements. This can be explained with by an improper evaluation of the size distribution used for the original development of the RTS model.

6.1 Static light scattering instrument

The optical set-up shown in Figure 1 was built to study the optical response of porous media. This instrument allows the simultaneous measurements of transmitted and scattered light at a fixed angle from the sample. It is composed of a green diode laser(λ = 532 nm *Coherent Compass* 315M-100), a spatial filter, and a thermostatic cell holder. The measuring cell is made of a square quartz cuvette and a rectangular frame custom-made to accommodate membrane samples ,**Figure 6.1**. Mixing of the solution was provided by a magnetic stirring bar. With this cell configuration, the angles that can be studied are relatively few (from $25°$ to $40°$). The scattering signal is collected with a multimode optical fiber at $\theta = 30°$. This cell enables the study of light transmitted by the media: it is focused with a lens on a pinhole of 50 μm diameter.In this way, only light rays that are not scattered or deflected inside the sample are collected, enabling measurement of the turbidity of the membrane. In fact, the light that passes through a medium of thickness d decreases its intensity in the following way:

$$\frac{I_T}{I_0} = e^{-\tau\, d} \tag{6.1}$$

where I_0 is the incident light intensity and τ the turbidity. Thus, turbidity can be easily recovered as:

$$\tau = \frac{1}{d}\,[log(I_0) - log(I_T)] \tag{6.2}$$

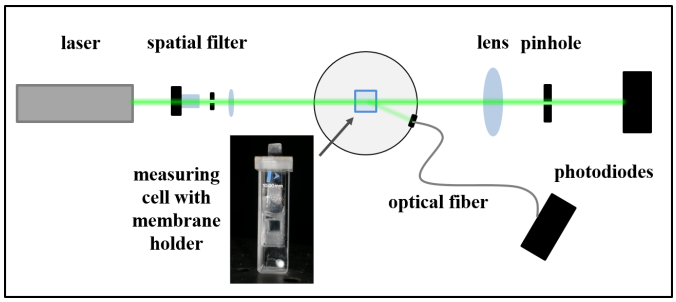

Figure 6.1: Representation of the scattering apparatus and the home-made membrane holder suitable for scattering measurements.

6.2 Optical microscopy measurements

Another method used in this work to understand the optical response of porous membranes was to study the contrast of these samples under an optical microscope in the sample's optical near field. Because the membrane's structural elements are small (below the diffraction limit), what is measured is the diffraction pattern by this medium, also called the speckle pattern, **Figure 6.2**. This pattern changes with the refractive index of the liquid in which the membrane is immersed. The pattern is generated by constructive and destructive interference between the strong transmitted field E_0 and the weak diffused one, E_s:

$$I_S \propto I_0 + \alpha\, E_0 E_s(x) \tag{6.3}$$

where $I_0 = E_0^2$ is the incident light intensity, I_s the diffused intensity and α an appropriate proportionality coefficient that depends on the microscope's transfer function. In Equation 6.3, we omitted the term for interaction between the scattered fields because it is much smaller that the other terms. This kind of approach has been used with X-rays [71]; but it is possible to apply this theory to these membranes because of their low contrast in water. It is possible to estimate the scattered intensity and the turbidity by analyzing the speckle pattern observed with a microscope. To understand how, we start from the definition of the variance σ^2 of a variable x, distributed as described by a probability function $f(x)$:

$$\sigma^2 = \int_{-\infty}^{+\infty} (x-\mu)^2 f(x) dx =< (x-\mu)^2 > \tag{6.4}$$

where μ is the mean value of the variable x. In our case, the interesting quantity is the scattered intensity $I_s(q)$, and, applying Equation 6.3 its variance can be written as:

$$\sigma^2 =< (I_s(x) - I_0)^2 > \propto < (\alpha E_0 E_s(x))^2 >= \alpha^2 I_0 < E_s^2(x) >= \alpha^2 I_0 \int |E_s(x)|^2 dx \tag{6.5}$$

The term that refers to the mean square value of the scattered field can be written in Fourier space, using the Perceval theorem, that states: $\int |E_s(x)|^2 dx = \int |E_s(q)|^2 dq$. With this formalism we have linked a property that can be easily obtained from the image of the speckle pattern, the normalized variance, and the scattered intensity:

$$\sigma_n^2 = \frac{\sigma^2}{I_0} \propto \alpha^2 \int |E_s(q)|^2 dq \propto \alpha^2 \int I_s(q)\, dq \tag{6.6}$$

So, recalling the definition of turbidity in the previous chapter, we obtained that the normalized variance σ_n^2 is proportional to the turbidity of the media. To obtain the normalized variance of a microscope image, we need to plot the grey-scale intensity histogram,**Figure 6.2**: it has a Gaussian shape so the mean value and the variance are easily obtained.

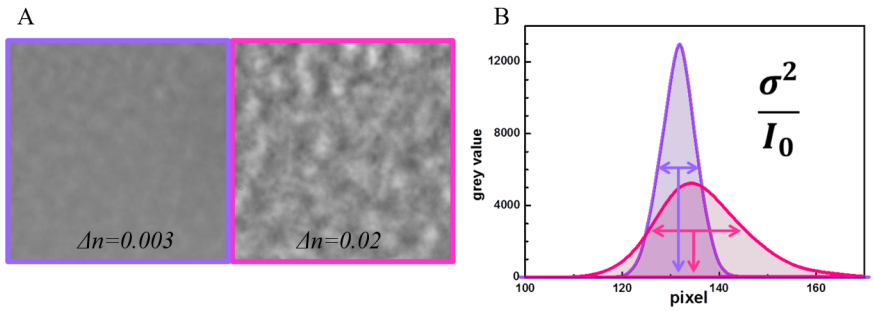

Figure 6.2: Image analysis of the microscope experiment. A) How the speckle pattern changes due to different mismatches Δn of solvent-membrane refractive indices. B) Histogram of the images in panel A: mean value and variance change with the refractive index of the solvent.

6.3 Scattering and Microscopy experiments with Cellulose Acetate (CA) membranes.

To prove the RTS model and the two different experimental approaches presented previously, we have performed optical analysis with commercial membranes: three different filters made of cellulose acetate (AC), with nominal pore size of μm, 0.65 μm and 5μm. Cellulose acetate has a refractive index of 1.475, much higher than that of water, so, to achieve index matching conditions, we soaked AC filters with mixtures of p-cymene (n=1.4905) and isopropyl alcohol (n=1.3776), [70]. To perform the microscope experiments, we put the membrane inside petri dishes 2 cm in diameter and added increasing amounts of p-cymene to this cell. To mix the liquid, we gently used a pipette and, after the measurement, collected some of the soaking liquid to measure its refractive index with an Abbe refractometer.

From the SEM images, **Figure 6.3**, we can obtain an idea of the internal morphology and also an estimate of the two characteristic lengths m and p (m_{sem} and p_{sem}), that are fundamental for the RTS model. We also analyzed these filters with the porosimetry method p_{poro} in **Table 6.3**, from which we found the mean pore dimensions. All these pore dimension estimations are reported in **Table 6.3**.

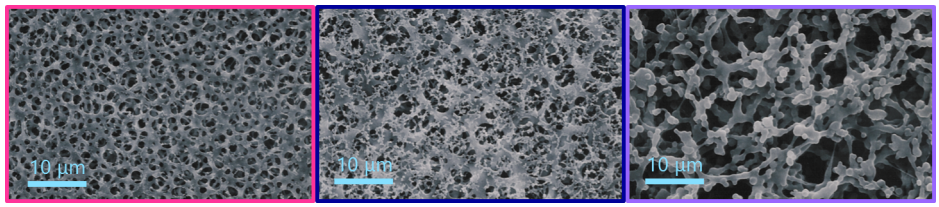

Figure 6.3: SEM images of AC filters. A) with nominal pore size of 0.45 μm, B) with nominal pore size of 0.65 μm and C) with nominal pore size of 5 μm. Bars are 10 μm.

These three different CA filters have very different internal structures, as well as different turbidity measured by both scattering and microscopy experiments. **Figure 6.4** reports turbidity measurements with the scattering apparatus and with microscope, respectively.

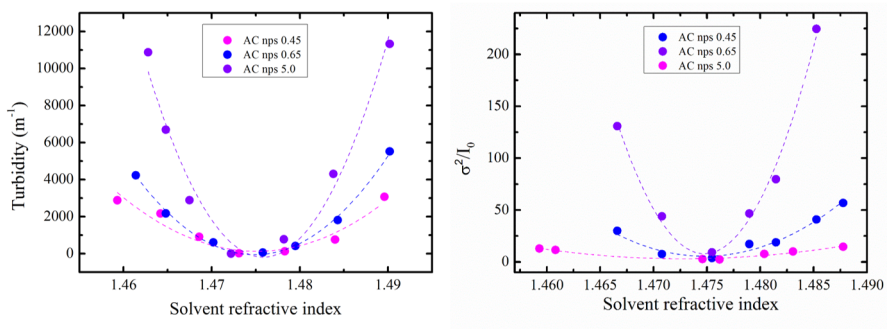

Figure 6.4: : Optical response of the three AC filters with both experimental setups. A) Measured turbidity with the light-scattering instrument, circular dots, and their parabolic interpolation to obtain the filter's refractive indices, dashed lines. B) Optical microscope measurements: normalized variance as a function of different refractive indices (circular points) and their fit to obtain the refractive index of the membranes (dashed lines).

First of all, we fit both scattering and microscopy measurements with a parabola (dashed lines in **Figure 6.4**) to obtain the refractive indices of the porous materials. The values of *n* obtained are all comparable and in agreement, **Table 6.3**.It is also possible to fit these experimental turbidities with the turbidity formula of the RTS model previously developed, 3.27:

$$\tau = \frac{\frac{p\,m}{(p+m)^2}\left(\varepsilon_p - \varepsilon_m\right)^2}{<\varepsilon>^2}\; a\; \frac{\frac{k^4}{a^4}}{1+4\,\frac{k^2}{a^2}} \tag{6.7}$$

$$where\ <\varepsilon>^2 = \frac{\left(\varepsilon_m m + \varepsilon_p p\right)^2}{\left(m+p\right)^2}$$

Using this approach there are two independent parameters, *m* and *p*, during the data fitting. But the porosity of the samples relates these two lengths to each other. In fact, the volume of the membrane matrix V_m scales with the cubic of the linear length *m*, $V_m = \alpha\, m^3$, as the volume of the empty phase sacles with *p*, $V_p = \alpha\, p^3$. The ratio between these volumes depends only on the characteristic lengths and, taking this into account, the porosity can be defined as the ratio of the volume of the empty phase to the total volume of the membrane; this can be written as:

$$\varepsilon = \frac{p^3}{p^3 + m^3} \tag{6.8}$$

Fitting the experimental data of **Figure 6.4A** with the Equation 6.7 and the constrain of Equation 6.8, values of *m* and *p* cab be obtained, reported in **Table 6.3**, (m_{fit} and p_{fit}). It is possible to compare these values with that obtained with the porosimetry test (p_{poro} in **Table 6.3**) and analysis of the SEM images, (m_{sem} and p_{sem}). We note that the lengths obtained with the scattering experiment are always larger than those achieved with other techniques. This might be imputed to more than one reason. First, the lengths taken from the SEM analysis are quite difficult to extrapolate, because the SEM images do not provide a pure two-dimensional area of the membrane, but instead provides access to different depths, which complicates image processing and accurate evaluation of the lengths. Therefore, the values in **Table 6.3** were extrapolated manually, with a relatively low statistical sample. In contrast, porosimetry measurement provides mean pore diameter, which still results in smaller pore sizes than the optical approach. This can be explained by arguing that the scattering is more sensitive to the larger structure of a polydisperse-pore-size sample, not to the mean value. Even though length overestimates are obtained with the scattering experiments, the scaling of turbidity with the different evaluated lengths is still observed, as shown in **Figure 6.5** where the turbidities calculated with Equation 6.7 for *m* and *p* values reported in **Table 6.3** are shown.

From the microscope experiments, we note that the same behavior observed in the scattering apparatus with the three different samples is present, meaning that the quantity being measured is proportional to the actual turbidity. However, to obtain an absolute value of turbidity, it is necessary to take into account that, with a microscope objective, we are also collecting a relatively wide range of scattering vectors, which depend on the α values and on the objective characteristics. To obtain the absolute turbidity, we must know the proportional constant present in Equation 6.3, which is strongly correlated to the transfer function of the microscope. This kind of analysis has not yet been done, so the microscope measurements have only descriptive content at present.

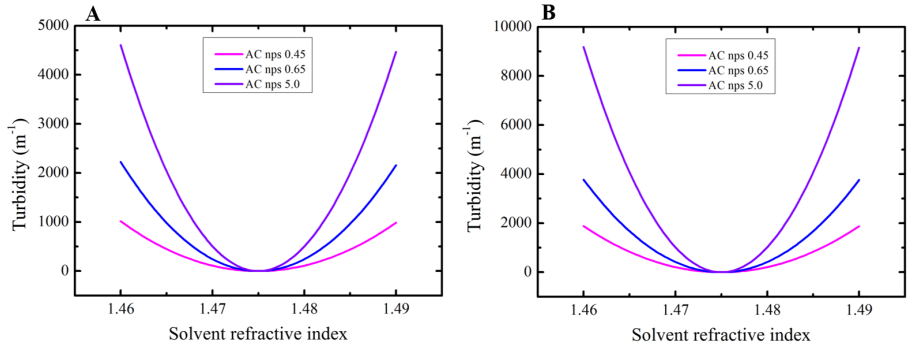

Figure 6.5: Comparison of turbidities of AC filters obtained from the different methods used to find m and p. Turbidities were calculated with Equation 6.7, using the m and p values reported in **Table 6.3** A) Here, $p = p_{poro}$ and $m = p_{poro}\sqrt[1/3]{\frac{1-\varepsilon}{\varepsilon}}$ B) Here $m = m_{sem}$ and $p = p_{sem}$. The absolute values of turbidities are different, but the same scaling observed in the optical experiments is maintained, **Figure 6.4A** and **6.4B**.

Table 6.1: Characteristic lengths of the three different CA filters achieved with three different methods.

membrane	m_{sem}	p_{sem}	p_{poro}	m_{fit}	p_{fit}	ε	n_s	n_m
CA 0.45	2.3 μm	0.9μm	0.8 μm	1.2 μm	2.0 μm	0.82	1.4751	1.4761
CA 0.65	2.4 μm	1.9 μm	1.8 μm	2.36 μm	4.1 μm	0.84	1.4749	1.4753
CA 5	4.4 μm	6.7 μm	3.9 μm	7.47μm	13 μm	0.86	1.4758	1.4756

Lengths taken from the analysis of the SEM images, the porosimety measurements and the fitting of the optical turbidity with RTS model. Here the measured porosities ε of the different CA filters are reported. Refractive indices of filters are reported for both scattering and microscope experiments, extracted from the minimum of the paraboic fit in Figure 6.3.

6.4 Scattering experiment on Hyflon AD® membranes: solutions with different refractive index

To study the newly prepared Hyflon AD® membranes, we chose to use the light scattering instrument only, because with this method the absolute turbidity of the porous medium can be obtained and thus compared with that calculated with the scattering models presented in *Chapter 3*. I have selected four samples of Hyflon AD® membranes, described in **Table 6.4**. Their SEM images are shown in **Figure 6.6B**: these membranes have significantly different internal morphologies. The samples 1, 2 and 3, unfortunately, have only one open surface and, for this reason, we could not obtain a reliable evaluation of the average pore size with the porosimeter instrument. Instead, because both of Sample 4's surfaces are porous, we found the mean pore dimension, using nitrogen flow, to be 9 μm.

I studied the turbidity of these fluorinated membranes in water. We found that this quantity changes depending on the wetting treatments undergone before carrying out a measurement. The lowest values of turbidity are always obtained when the membrane is wetted with a mixture of water/ethanol for several days, changing the solvent each day and then leaving the membrane in water for 4 hours before the experiment. We used this hydration method for all of the following experiments

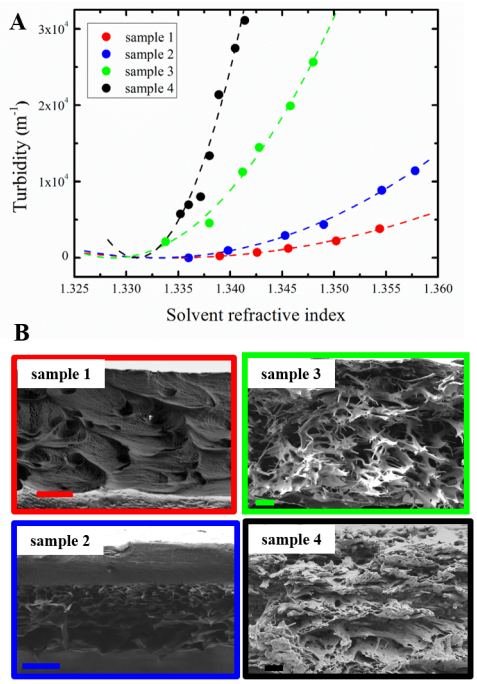

Figure 6.6: Optical experiments with Hyflon AD® membranes. A) Turbidity of Hyflon AD® membranes as a function of the solvent refractive index. B) SEM images of the studied sample are shown. Bars are 10 μm.

In the experiments of **Figure 6.6A**, the turbidity of Hyflon AD® membranes have been studied by changing the refractive index of the solvent that fills the pores, using mixture of ethanol and water, to enable measurement of the refractive index with an Abbe refractometer. It is evident that membranes with different internal morphologies

have quite different optical responses.

Fitting these experimental data to a parabola (dashed lines in **Figure 6.6A**) it is possible to obtain the refractive index of the porous materials (see **Table 6.4**). These experimental turbidities can be fitted to the RTS model previously developed, using Equation 6.7 and the constrain of Equation 6.8. From this analysis, we obtained the p_{fit} and m_{fit} reported in **Table 6.4**.

For Sample 2 and 3, lengths estimated with the SEM analysis (reported in **Table 6.4**) are in good agreement with experimental data. For Sample 1, we do not obtain a good result, probably because of the closed and dense structure of the membrane, **Figure 6.6B**. From the SEM images it is evident that the large visible pores are not interconnected, so liquid does not fill them. For this reason, describing this porous medium with the RTS model is inappropriate.

For sample 4, too, there is no agreement between the SEM image analyses, the mean pore size dimension achieved with nitrogen flow and the optical measurements. First of all, the morphology of the sample, as shown in **Figure 6.6B**, it is difficult to study, because there is an higher polydisperisty of the pore and membrane dimension: the structure is less uniform and homogeneous and, for this reason, it is difficult to extract a value for the characteristic lengths. The measured turbidities are no compatible with the mean pore size measured with the porosimetry instrument, too (9 microns). Both from porosimeter and SEM analysis a lower increment of turbidity is expected: for all these reasons I can suppose that during the optical experiment the presence of some bubbles air, for example, has affected the measurement.

Table 6.2: Characteristic lengths of Hyflon AD® membranes.

# sample	refractive index	m SEM	p SEM	m fit	p fit	ε
1 (23)	1.334±0.001	2.7	6.2	0.6	0.6	0.5
2 (8)	1.3329±0.0006	2.8	1.5	1.9	1.9	0.5
3 (15)	1.329±0.001	3.9	11.6	6.1	8.6	0.74
4 (16)	1.3310±0.0005	5.0	4.7	61.3	76.5	0.66

Samples' refractive indices calculated from a parabolic fit of the experimental data reported in **Figure 6.6**. The lengths m and p are extrapolated from analysis of the SEM images shown in **Figure 6.6**

6.5 Scattering experiment on Hyflon AD® membranes: surfactant adsorption

For surfactant adsorption, I focused the study on scattered intensity at a fixed angle (30°) instead of transmitted light, because index-matched porous media have very low diffusive power, such that incident light passes straight through without any deviation, leading to a high transmitted light intensity and very small scattered intensity. Due to surfactant adsorption, we expect little variation in the optical response of the material, so it is more appropriate to study the scattered light. In fact, in the scattered intensity, there is a higher signal-to-background ratio.

To characterize surfactant adsorption, we utilized Sample 3 of **Figure 6.6B**, because this membrane has high porosity and a homogeneous morphology. For this sample, we performed two different types of experiments, as before with the Hyflon AD® prism, to determine the mass detection limit. In fact, with the membrane having a large available surface area for adsorption, we expect the kinetics to be mass-transport limited. We therefore performed experiments with both increasing surfactant concentration in the cuvette **Figure 6.7**, and also with increasing the fluid volume, keeping the surfactant concentration fixed (inset of **Figure 6.7**). The experiments were performed with the cationic surfactant SBSAC in deionized water at room temperature.

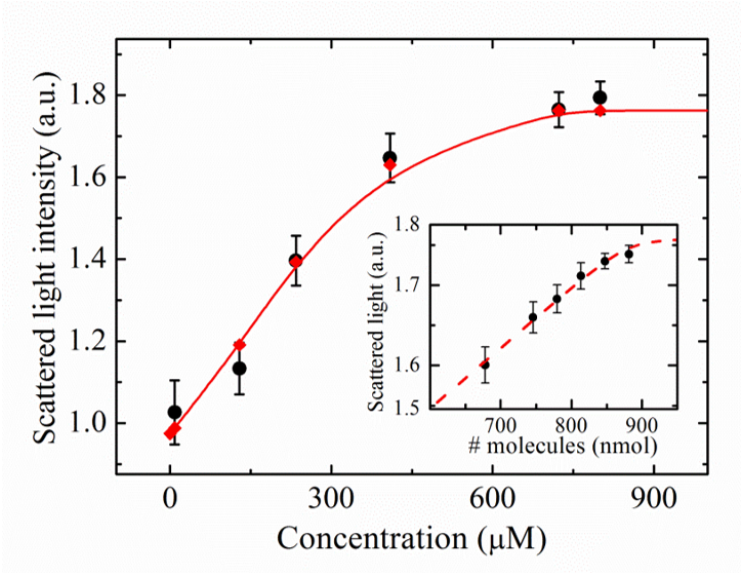

Figure 6.7: Intensity of light scattered by a microporous membrane of Hyflon AD® for different concentrations of SBSAC in deionized water. Dots and diamonds refer to experimental data and fit values, respectively. The line is a spline to guide the eye. Inset: scattered light intensity as a function of the number of molecules in cuvette for a constant concentration of 340 μM (dots) and fitting curve (dashed line).

The scattering signal increased rapidly after each addition of the surfactant to the aqueous solution and reached an equilibrium value in a few seconds. **Figure 6.7B** 2B reports such equilibrium values measured about 500 s after the addition. **Figure 6.7** shows that the equilibrium scattering signal increased as a function of the surfactant concentration until reaching a plateau corresponding to full coverage of the membrane surface. In the inset of**Figure 6.7** measurement performed by increasing the total number of molecules in solution at fixed concentration is reported. A signal increase and a

plateau were observed also in this case. This behavior indicates the presence of a large total area available for adsorption, demonstrating a high affinity for the surfactant.

The parameters extracted with the RPI method for the planar surface provided the basis upon which to interpret the adsorption of SBSAC surfactant onto this microporous membrane. The experimental data reported in **Figure 6.7** were fitted by mass-limited Langmuir, Equation 5.4, keeping the value of K_d constrained to the one obtained for the planar surface (Table 5.4). he resulting fitting curves are shown as continuous lines in **Figure 6.7** (main panel and inset). The extracted total number of binding sites N_s of the membrane surface was about 0.88 ± 0.1 μmol corresponding to an available area for adhesion about 400 times larger than that of the prism surface. As expected, the porous membrane provides a much larger adhesion surface for molecular adsorption. The increase in the available surface area agrees with the total surface of the membrane estimated by nitrogen flow resistance measurements[72].

6.6 Comparison of the optical response of different index-matched materials

Using the scattering model presented in Section 3.3 under R-G condition and thin-film theory, we can compute the thickness of the SBSAC surfactant layer on the fluorinated material. In order to evaluate this quantity, it is necessary to calculate h_0 and d_0 in the equations $R = R_0 \left(1 + \frac{h^2}{h_0^2}\right)$ and $I_s = I_0 \left(1 + \frac{d^2}{d_0^2}\right)$ for reflectivity and scattering experiments, respectively. These two quantities represent the thickness of the layer at which the measured optical signal doubles its value. I have found the formulae of these quantities to be (Equations 3.3 and 3.19) :

$$h_0 = \frac{\lambda\sqrt{R_0}}{4\pi n_l r_{1l} cos(\theta_{t1})} \tag{6.9}$$

$$d_0 = \frac{(n_m^2 - n_s^2)}{(n_l^2 - n_s^2)} \frac{\lambda}{4\,\pi\, n_s sin(\theta_s/2)}. \tag{6.10}$$

In **Figure 6.8**, the values of both these quantities are reported as a function of the incidence angle, which can be readily converted to the scattering angle θ_0, with the following relation: $\theta_s = \pi - 2\theta_0$. They were calculated taking into account the characteristics of the two different light sources and substrates (data in**Table 6.6**). At a $\theta_0 = 45°$, i.e. the reflectivity experiment, we obtain $h_0 = 3.15$ nm; for a $\theta_s = 30°$the scattering experiment, we obtain $d_0 = 3.5$ nm. Using these values and knowing the relative increment of optical signal when adsorption is complete in both experiments, we can obtain the layer thickness. As shown in **Table 6.6**, the thickness of the layer has almost the same value in both experiments. Therefore, despite the different optical signal and surface area, the detection based on prism reflectivity and membrane scattering leads to the same result.

Table 6.3: Values used to calculate h_0 and d_0 under the experimental conditions.

media	λ (nm)	$\mathbf{n}_m$	$\mathbf{n}_s$	$\mathbf{n}_l$	$\mathbf{h}_0$ **(nm)**	**Contrast**	$\mathbf{h}_{layer}$**(nm)**
prism	632.8	1.328	1.334	1.435	3.15	1.89	2.68
membrane	532	1.331	1.334	1.435	3.5	1.75	3.03

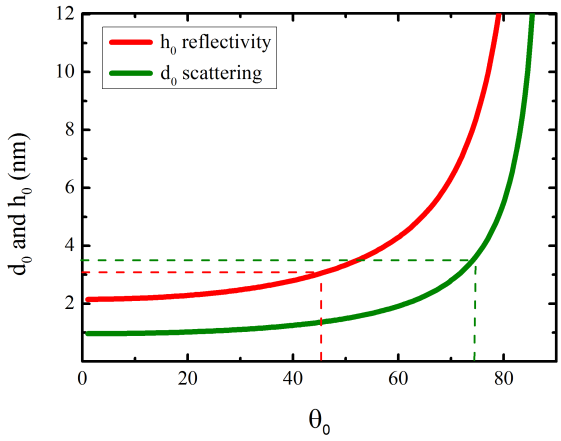

Figure 6.8: h_0 and d_0 as a function of the incident angle or scattering angle, according to the relationship: $\theta_s = \pi - 2\theta_0$. The working angle are 45° and 30° for reflectivity and scattering measurements, respectively. It is thus possible to determine the exact values of h_0 and d_0 under the working conditions.

6.7 Study of the membrane morphology with RTS model

In Section 3.4 I presented another optical model to study the response of a porous medium in the case of molecular adsorption onto its surfaces: it is the *Random Telegraph Signal* with a thin layer covering all the membrane/water interfaces. In the previous section, we found that the thickness of the surfactant layer on the membrane surface is 3 nm; using the RTS model, now, we can calculate what combination of characteristic lengths m and p would lead to the observed scattering intensity increase when a 3 nm layer of SBSAC adsorbs on the plastic surface. In fact, keeping the thickness of the surfactant layer fixed at 3 nm and its refractive index constant, it is possible to numerically calculate the scattered intensity with the RTS in the case of three different media, as a function of different m and p, as shown in Section 3.4. Also in this case, m and p satisfy the relationship of Equation 6.8. The ratio of this calculated scattered intensity in the presence of the surfactant layer, I_s, can be separated into the scattered intensity without the coating layer, I_0: in this way we obtain the theoretical contrast, $C = I_s/I_0$, due to the surfactant adsorption that can be compared with the experimental one, which is 1.75, Figure 6.7.

In **Figure 6.9A**, report these theoretical contrasts for different combinations of m and p that satisfy the porosity relationship for a fixed thickness of the surfactant layer. We find that the experimental contrast can be obtained with $17\mu m \leq p \leq 23\,\mu m$ and $12\mu m \leq m \leq 16\,\mu m$ (green region in the **Figure 6.9A**). These lengths are not in complete agreement with those found through other techniques, see **Table6.4**. With this analysis, we obtain an over-estimation of the characteristic lengths. For large values of p and m, the contrast C does not go to 1, but to a larger value that can be extracted by fitting the points in **Figure 6.9A** to a hyperbolic function. In the case reported, this value at large p is 1.34 ± 0.02. This value can be compared with that obtained in the Rayleigh-Gans approximation for a system of core-shell spheres polydispere in size. In fact, in Section 3.3, **Figure 3.4**,we found that for large radii, the contrast between a system of coated polydisperse spheres and the bare system does not go to zero, but to a fixed value that depends on the refractive indices of the particles and of the coating layer. In that calculation, the value of the contrast C found in the limit of large radii was 1.83 ± 0.01.

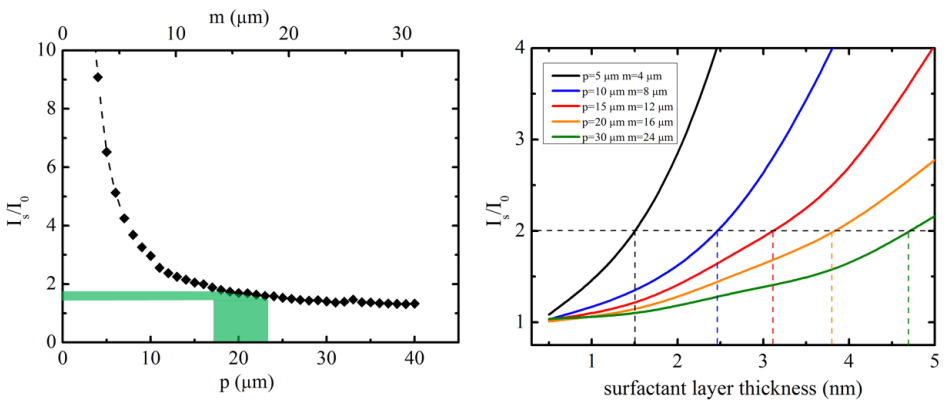

Figure 6.9: Molecular adsorption studied with RTS. A) Calculated contrast at fixed layer thickness for different combinations of the characteristic lengths that satisfy Equation 6.8. In the green region are highlighted the values of p that reflect the experimental contrast. B) Contrast as a function of layer thickness. For different combinations of m and p the value at which the contrast doubles is not constant, but depends on the characteristic lengths.

In **Figure 6.9B** contrast C as a function of the thickness of the layer is shown for different combinations of m and p that obey the condition of Equation 6.8. It is evident that in RTS the contrast depends on the characteristic sizes, **Figure 6.9B**. We did not find the same behavior using the Rayleigh-Gans model. It that case, Section 3.3, the contrast C was independent of the radius of the spheres, in the limit of large radii relative to the wavelength and in the presence of their polydispersity. In particular, we found that h^*, which is the thickness at which the contrast doubles its value, is a constant that depends on the instrument configuration and the refractive indices of the samples. Indeed, in the RTS model, the contrast always has a parabolic behavior with the thickness of the molecular layer, but the h^* value depends on the characteristic lengths m and p, **Figure 6.9B**.

This observation can be explained with the following argument. In the R-G model, we do not consider a particular distribution of sizes when we average the radii. Instead, the RTS model is based on an exponential distribution of lengths, where m and p are their mean values. The exponential distribution takes into account a large number of short lengths, those that contribute more to the increase of the contrast. Looking at the SEM images, it is quite intuitive that, inside the porous sample, there is a cut-off for the short lengths: there are not pores or membrane parts of tens of nanometers, for example. For this reason, an exponential distribution of lengths is not appropriate to describe in the best way this type of porous material. Different sorts of distributions and computational simulations of porous media can help in the description of the optical response of these samples.

Chapter 7:
Integration of micro-porous materials into micro-fluidics devices

In this last chapter, I present different strategies for the integration of new phantom materials realized in this work into microfluidic devices. This integration part is fundamental for the development of an autonomous sensor able to detect presence of surfactants and other water pollutants in aquatic environment. Three microfluidic devices are presented: one for host micro-porous membrane and two prototype of chromatography column made by phantom micro-beads. For one of the colloids devices, first optical analysis made to extract the refractive index of the beads are shown. These work is a collaboration with the University of the Basque Country UPV/EHU (Spain).

7.1 Microfluidic chip for microporous membrane integration.

To prevent the rapid clogging of the filter, I decide to adopt a cross-flow filtration [31]. In fact, in this configuration, just a portion of the water sample passes through the membrane, ensuring a longer lifetime of the membrane, that is one of the desirable characteristic of an autonomous and disposable sensor. To force the fluid to pass into the porous medium, it is necessary to win the hydraulic resistivity of the membrane. This quantity can be calculated supposing that the membrane is made of capillary holes of 5 μm diameter, as the pore size distribution suggests, in a number that can approximate the experimental volume porosity. Knowing this quantity, I designed the chip with the specifications present in **Figure 7.1**. With this configuration, the 20% of the water flow it is supposed to pass through the membrane.

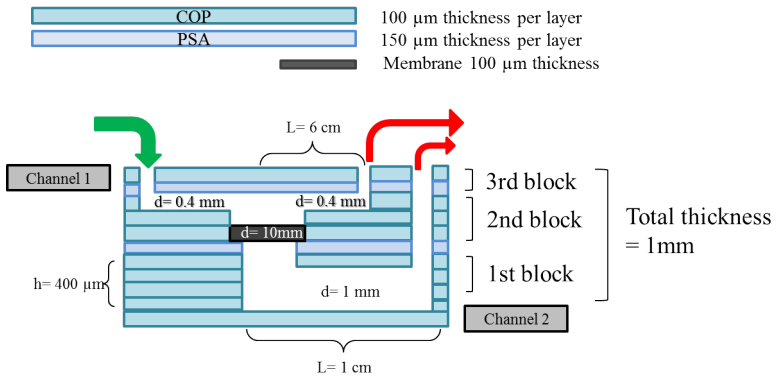

Figure 7.1: Schematic representation on the membrane microfluidic device

This micro-fluidic device is composed of several overlapped cyclo-olefin-polymer films (COP) of 100 μm thickness each, bound together by a pressure sensitive adhesive (PSA). COP is an amorphous polymer that guarantees the optical transparency in the visible wavelengths spectra, so the optical studies of this membrane will be possible [73]. In **Figure 7.2** is shown the first prototype, in which is present a commercial hydrophilic polycarbonate membrane. It does not presented leakages. A micro-fluidic device embedding a Hyflon AD® membrane was realized, **Figure 7.3**: this device works properly.

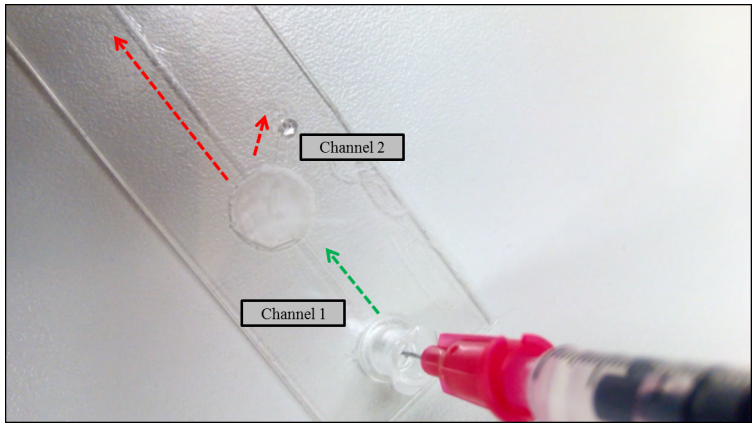

Figure 7.2: Membrane microfluidic device prepared with a polycarbonate membrane to test the flow. It works without leakages.

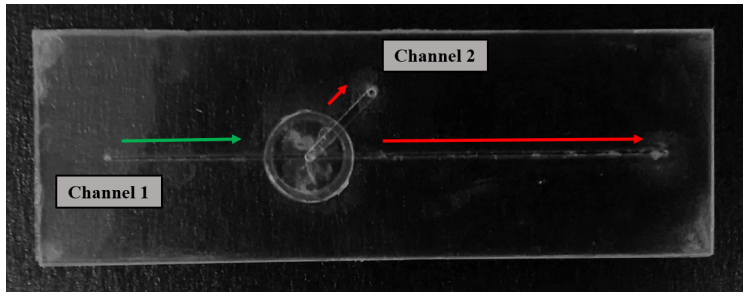

Figure 7.3: Membrane microfluidic device prepared with a Hyflon AD membrane, sample number 16.

7.2 Realization of Chromatography columns

Once obtained iso-refractive to water colloids, it is necessary to trap them into a capillary tube to realize the chromatography column. There are different ways to trap colloids into a microfluidic device [74] [75]. The easiest approach that do not require particular technology is to create a bottleneck into a rectangular glass capillary tube using a blowtorch. Then, into this waist, I put some cotton-wool as filter and then I purge the colloids inside the capillary. This configuration allows a proper washing of the colloids with different solvents to remove the surfactants present during the emulsion step. In **Figure 7.4** it is possible to see this first prototype of chromatography column filled with the fluorinated colloids, highlighted with two yellow arrows.

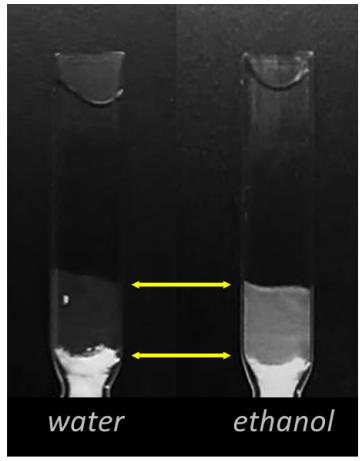

Figure 7.4: Difference in scattered light of trapped colloids in different solvents

Another prototype of chromatography column has been realized with the collaboration of University of the Basque Country UPV/EHU. Inside a microfluidic channel a wall with a passage narrower than the avarage colloids diameter is created. In **Figure 7.5** is shown a scheme and a picture of this device, containing phantom colloids.

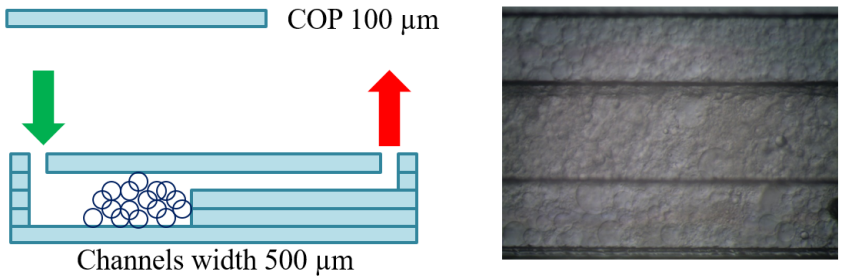

Figure 7.5: Schematic representation of colloids microfluidic device and its microscope image

7.3 Optical characterization of phantom chromatography column

In this last section, I present the optical characterization of first prototype of phantom chromatography column, **Figure 7.6**. The iso-refractive to water colloids were injected inside the channel simply using a pipette. Then, it was connected to a syringe pump and placed in the optical apparatus, shown in **Figure 7.7**. This set up is composed of a LED (amber yellow, $\lambda = 592nm$), two lenses, a diaphragm and a CCD camera, on which the image of the capillary is projected.

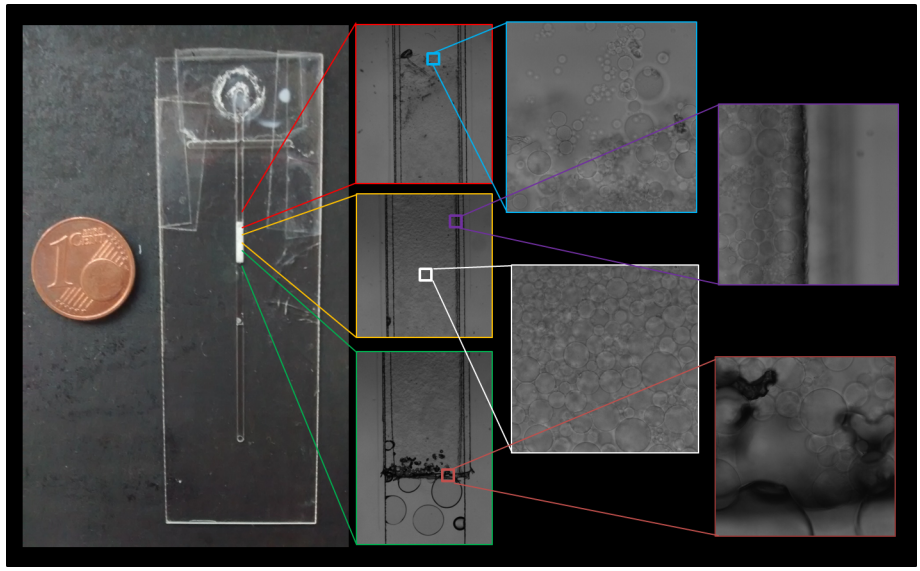

Figure 7.6: Different images of the microfluidic device filled with phantom micro beads

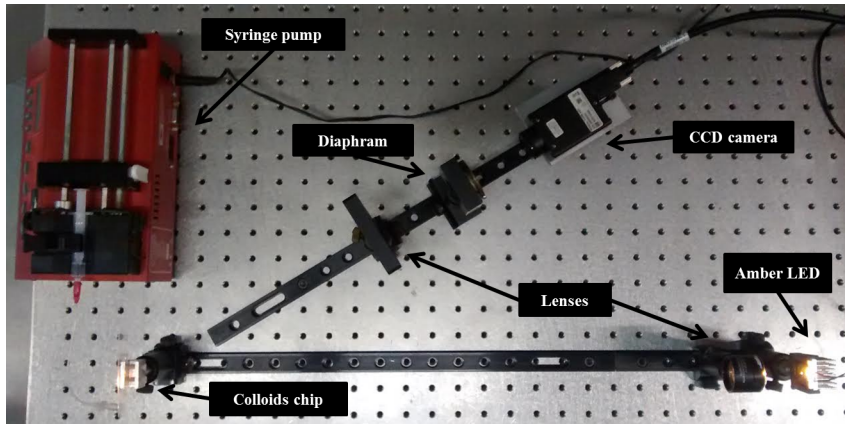

Figure 7.7: Optical apparatus to study the scattered light by the trapped beads

Thanks to the geometry of the microfluidic, it is possible to monitor the back-scattered light by the colloids: at large scattering angles a higher sensitivity is expected because h_0, according to Equation 6.9, assumes lower values for larger scattering angles ($150°$ in

the experimental set-up). To calculate this value, fundamental to achieve the amount of adsorbed surfactants, it is necessary to know the proper refractive index of the colloids. For this reason, I measured the scattering intensity by the column in function of refractive index of solvent that soaks the membrane. In particular, I flew through the channel increasing mixtures of glycerol/water, which refractive indices were measured with an Abbe refractometer.

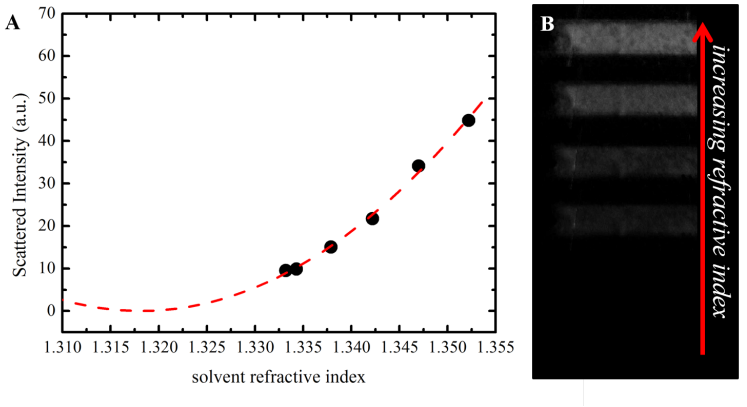

Figure 7.8: Characterization of phantom chromatograpy column. A) Scattered intensity as a function of the solvent's refractive index. B) Images of the microfluidic during the measurement.

The extrapolation of the minimum of the parabola that fits the experimental data in **Figure 7.8**, leads to the refractive index of the colloids, that results to be n=1.318. Thanks to this measurement, it is possible to calculate the h_0 of this new medium, that is 5.5 nm. So, for a layer of 3 nm thickness, an increment in the scattering light of 30% is expected. The sensitivity of this media is lower compared to the other materials used in this work, because of the high refractive index mismatch between colloids and water. Using a fluorinated oil with shorter fluorine chain or the adding of some addictive inside the Fomblin MD40® before the realization of the beads, can lead to a better index matching and, so, to a higher sensitivity of the substrate.

Future directions

In this thesis, different perfluorinated plastic substrates have been realized and used to study molecular adsorption. In particular, I specifically focused on the study of spontaneous adsorption of amphiphilic molecules on the water-plastic interface. As previous works have demonstrated, these perfluorinated plastics can be used in the field of biosensing, thanks to their optical properties: they are amorphous and they have refractive indices (1.318-1.331) very close to that of water (1.334). This is the reason why these kind of materials are called *phantom*.

The aim of this work was to use these perfluorinated materials as substrates for the detection of polluting molecules into aquatic environment, embedding them into an autonomous detector. To analyze large volumes of water, a filtering substrate is preferred because it provides a large available surface for the adsorption and because all the water sample can flow through it, without any bulk-to-surface transport problem. For this reason, I have developed, for the first time, phantom micro porous membranes and phantom chromatography column made of perfluorinated polymers. I have found the experimental condition to obtain highly porous membrane with a stable and uniform morphology, using the *Non-solvent Induced Phase Separation* method. In order to realize the phantom chromatography column, I have fabricated micro-beads via different emulsification techniques. Then the emulsion weas photo-polymerized to obtain solid colloids.

To quantify the number of polluting molecules adsorbed on the plastic surface, I have developed theoretical optical models that link the optical signal to the adsorbed molecular layer thickness. In particular, two different models that describe the scattering by a polydispersed sample of spheres and by a random porous material were developed. A simple and surprising similarity between the sensitivity of the reflectance- and scattering-based systems was found.

I have characterized the interaction between the perfluorinated plastic and the polluting molecules in the easiest configuration, in which the signal is provided by the light reflected by the planar surface of a right-angle prism. Remarkably, the adsorption behavior for different surfactants, a protein and an oil were very different, whereas all the studied surfactants displayed a similar behavior, despite the different net charge and structure. The molecular size and the molecular area in contact with the surface upon adsorption were identified as relevant parameters, through different specific mechanisms:

- the optical response scaled with the squared molecular size affecting the thickness of the adsorption layer;

- the strength of the adsorption interaction at equilibrium was found to scale with the molecular hydrophobic contact area on the perfluorinated surface;
- for the fastest adsorption kinetics, where transport phenomena became a limiting effect, the observed adsorption rate scaled with the molecular contact area and the diffusion coefficient D, where, in general, D scales with the reciprocal molecular size.

With prism substrate, I have also tested real river water samples. From the simultaneous study of the equilibrium and the kinetics adsorption, the surfactant concentration can be estimated. The scaling of surface adsorption on the molecular structure identified in this work provides a demonstration of selective detection against different classes of molecules. In order to increase the selectivity of detection, different strategies of surface functionalization are currently investigated, including the adsorption of thin hydrogels made of functional copolymers, or the immobilization of different polylysines that differ for stereochemistry and link position and polysaccharides.

Using a different kind of substrate with very low reflectivity, a glass chip with a proper anti-reflective layer, I have studied the boilogical interaction between the humane growth hormon (hGH) and specific antibodies. This device enabled detecting hGH in a few minutes, with an estimated limit of detection of about 3 ng/ml. By using this substrate, I obtained high sensitivity and clean images of the surface spotted with antibody, even in turbid and absorbing media. Moreover, and rather unexpectedly, I found that the binding performance of immobilized antibodies was unaltered by the presence of non-specific adsorption due to 60% human serum.

Regarding the porous material developed in this thesis, I have tested the optical performance of micro-porous membrane both in solventd with different refractive indices and in presence of surfactants. Surprisingly, the same thickness of the adsorbed surfactant layer was found with the planar surface and the porous membrane, meaning that the different morphology of the substrate does not alter the interaction between the plastic and the molecules. In this contest, two different theoretical models were developed accounting for the optical response of these systems: further works and computational simulations are needed to better understand the relation between the internal morphology of porous medium and its optical responce upon adsorption.

Finally, various microfluidic prototypes to embed the porous materials realized in this work are proposed. Measurements of surfactants adsorption using these novel microfluidic devices are currently in progress, addressing the overlall performance of detection and the optimal fludic parameters to provide access to the kinetics of adsorption. Regarding the phantom chromatography column, a better way to trap the colloids limiting their movements has to be found. For example, the realization of a in situ frit can be adopted. Also different tests on the fluidic performance of the device have to be done, to understand what is the proper size and polydispersity of the beads to provide an homogeneous flow inside the column.

The realization of these prototypes is fundamental for the develop of an autonomous device to analyze real water sample. These micro-fluidic devices can be easily integrated in compact optical platforms, using low cost LED and camera. This is a main objective of the NAPES project, which aim is to realize autonomous systems able to collect and concentrate the water sample, analyze it and provide a real time monitoring of the quality of aquatic environment.

Acknowledgments

Three years are long.
During this time, various people have helped me and shared beautiful and difficult moments. Now it is time to thank them.
First of all, I want to thank my supervisor Marco to be a good boss, an excellent teacher and a friend who gave me the proper freedom and assistance in my research. You gave me amazing opportunities and guided me along these three years. You has always been a certainty in these years. Thank you.
During these years, I had the wonderful opportunity to collaborate with various groups. I want to thank you all: Emanuele Di Nicoló and Mattia Bassi from Solvay Specialty Polymers (Bollate), Janire Saez and Fernando Benito-Lopez from the University of the Basque Country UPV/EHU (Spain), Davide Ferraro from Institut Curie (Paris) and all the NAPES partners. Without you a great part of this work would never see the light.
Thanks to Antonio Ricco: your help and your corrections have been fundamental in improving the work of this thesis.
Next I would like to say thank to my research group, in particular to Tommaso, Roberto and Giuliano. You have always been a source of inspiration, strength and enthusiasm. It has been a great pleasure to work with such creative and challenging persons, always ready to share their knowledge with me. Thank you.
How can I forget Fabio? Thank to be the smartest, most enlightening and perfect colleague and teacher that I can ever imagine...and thank you to have introduced me in the climbing world (and to believe in me on the blocco blu!).
Thanks to all the other lab members: Silvia, Marina, Matteo, Tommaso, GioN, GioT: breakfasts, lunches, tea times and breaks would not have been the same without your smiles, laughs, affection, warmth and friendship. Thank you.
Special thanks goes to my dear friends and ex-colleagues, from Singapore to Philadelphia, Erica and Francesca: you have sheared with me the best and the worst moments during these three years, in my work and in my life. You are the prove that the good things do not come to an end.
Finally, I want to thanks all the people who made with me part of this road. Some have been lost, some have come back on my way and others have been always by my side. You gave me the strength and the hope to go on. Thank you, from the deep of my heart.
Questo lavoro é dedicato alla mia famiglia: unico porto sicuro nel mio vagare. Grazie per esserci sempre stati e per amarmi.

Roberta

List of Publications

This work is based on the following publications:

- R. Lanfranco, F. Giavazzi, M. Salina, E. Di Nicolò and M. Buscaglia. "Optical Detection of Surfactants by Means of Reflective Phantom Interface Method Sensors", *Lecture Notes in Engineering*, Volume 319, 2015, pp 33-37
- M. Salina, F. Giavazzi, R. Lanfranco, E. Ceccarello, L. Sola, M. Chiari, B. Chini, R. Cerbino, T. Bellini and M. Buscaglia. "Multi-Spot, Label-Free Immunoassay on Reflectionless Glass" *Biosens. Bioelectron.*, Volume 74, 15 December 2015, Pages 539–545
- R. Lanfranco and M. Buscaglia. "Invisible Fluorinated Materials for Optical Sensing" *Reference Module in Materials Science and Materials Engineering*, to be published
- R. Lanfranco, F. Giavazzi, M. Salina, G. Tagliabue, E. Di Nicoló , T. Bellini and M. Buscaglia. "Selective adsorption on fluorinated plastic enables the optical detection of molecular pollutants in water", submitted.

Bibliography

[1] A. M. Becker, S. Gerstmann, and H. Frank. Perfluorooctane surfactants in waste waters, the major source of river pollution. *Chemosphere*, 72(1):115–121, 2008.

[2] Hanan S. Abd El-Gawad. Aquatic environmental monitoring and removal efficiency of detergents. *Water Science*, 28(1):51 – 64, 2014.

[3] T. Ivankovic and J. Hrenovic. Surfactants in the Environment. *Archives of Industrial Hygiene and Toxicology*, 61(1):95–110, 2010.

[4] Gazzetta ufficiale unione europea, 12-03-2004, c64e/553.

[5] C. Coll, R. Martinez, D. Marcos, F. Sancenon, and J. Soto. A Simple Approach for the Selective and Sensitive Colorimetric Detection of Anionic Surfactants in Water. *Angewandte Chemie International Edition*, 46(10):1675–1678, 2007.

[6] J. Norberg, E. Thordarson, L. Mathiasson, and J. A. Jonsson. Microporous membrane liquid-liquid extraction coupled on-line with normal-phase liquid chromatography for the determination of cationic surfactants in river and waste water. *Journal of chromatography. A*, 869(1-2):523–9, 2000.

[7] A. A. Boyd-Boland and J. B. Pawliszyn. Solid-phase microextraction coupled with high-performance liquid chromatography for the determination of alkylphenol ethoxylate surfactants in water. *Analytical chemistry*, 68(9):1521–1529, 1996.

[8] K. Ichikawa A. Tsuchiya T. Ando S. Te, K. Otsuka. Electrokinetic separations with micellar solutions and open-tubular capillaries. *Anal. Chem.*, 56:111–113, 1984.

[9] F. Foret, S. Fanali, L. Ossicini, and P. Bovcek. Indirect photometric detection in capillary zone electrophoresis. *Journal of Chromatography A*, 470(2):299–308, 1989.

[10] P. Gallagher and N. Danielson. Capillary electrophoresis of cationic and anionic surfactants with indirect conductivity detection. *Journal of Chromatography A*, 781(1-2):533–540, 1997.

[11] S. Anastasova, A. Radu, G. Matzeu, C. Zuliani, U. Mattinen, J. Bobacka, and D. Diamond. Disposable solid-contact ion-selective electrodes for environmental monitoring of lead with ppb limit-of-detection. *Electrochimica Acta*, 73:93–97, 2012.

[12] W. Groh and A. Zimmermann. What is the lowest refractive index of an organic polymer? *Macromolecules*, 24(25):6660–6663, 1991.

[13] E. Giannetti. Semi-crystalline fluorinated polymers. *Polymer International*, 50(1):10–26, 2001.

[14] V. Arcella, A. Ghielmi, and G. Tommasi. High performance perfluoropolymer films and membranes. *Annals of the New York Academy of Sciences*, 984(Mi):226–244, 2003.

[15] F. Giavazzi, M. Salina, R. Cerbino, M. Bassi, D. Prosperi, E. Ceccarello, F. Damin, L. Sola, M. Rusnati, M. Chiari, B. Chini, T. Bellini, and M. Buscaglia. Multispot,

label-free biodetection at a phantom plastic-water interface. *Proceedings of the National Academy of Sciences of the United States of America*, 110(23):9350–5, 2013.

[16] A. Milani, M. Tommasini, C. Castiglioni, G. Zerbi, S. Radice, G. Canil, P. Toniolo, F. Triulzi, and P. Colaianna. Spectroscopic studies and first-principles modelling of 2,2,4-trifluoro-5-trifluoromethoxy-1,3-dioxole (TTD) and TTD–TFE copolymers (Hyflon® AD). *Polymer*, 49(7):1812–1822, 2008.

[17] S. Turri, A. Sanguineti, and R.a Lecchi. Novel glass fiber-reinforced composites having a UV and peroxy curable fluoropolymer matrix. *Macromolecular Materials and Engineering*, 288:708–716, 2003.

[18] R. Bongiovanni, E. Zeno, a. Pollicino, P. M. Serafini, and C. Tonelli. UV light-induced grafting of fluorinated monomer onto cellulose sheets. *Cellulose*, 18(1):117–126, 2010.

[19] J. Voros. The density and refractive index of adsorbing protein layers. *Biophysical Journal*, 87(1):553 – 561, 2004.

[20] A. Ghetta, D. Prosperi, F. Mantegazza, L. Panza, S. Riva, and T. Bellini. Light scattered by model phantom bacteria reveals molecular interactions at their surface. *Proceedings of the National Academy of Sciences of the United States of America*, 102(44):15866–15870, 2005.

[21] D. Prosperi, C. Morasso, F. Mantegazza, M. Buscaglia, L. Hough, and T. Bellini. Phantom nanoparticles as probes of biomolecular interactions. *Small*, 2(8-9):1060–1067, 2006.

[22] D. Prosperi, C. Morasso, P. Tortora, D. Monti, and T. Bellini. Avidin Decorated Core–Shell Nanoparticles for Biorecognition Studies by Elastic Light Scattering. *ChemBioChem*, 8(9):1021–1028, 2007.

[23] C. Morasso, T. Bellini, D. Monti, M. Bassi, D. Prosperi, and S. Riva. Dispersed phantom scatterer technique reveals subtle differences in substrate recognition by phospholipase D inactive mutants. *ChemBioChem*, 10(4):639–644, 2009.

[24] C. Morasso, M. Colombo, S. Ronchi, L. Polito, S. Mazzucchelli, D. Monti, M. Buscaglia, T. Bellini, and D. Prosperi. Towards a universal method for the stable and clean functionalization of inert perfluoropolymer nanoparticles: Exploiting photopolymerizable amphiphilic diacetylenes. *Advanced Functional Materials*, 20(22):3932–3940, 2010.

[25] F. Giavazzi, M. Salina, E. Ceccarello, A. Ilacqua, F. Damin, L. Sola, M. Chiari, B. Chini, R. Cerbino, To. Bellini, and M.o Buscaglia. A fast and simple label-free immunoassay based on a smartphone. *Biosensors and Bioelectronics*, 58(October 2015):395–402, 2014.

[26] R. Lanfranco, F. Giavazzi, M. Salina, E. Di Nicoló, and M. Buscaglia. Optical detection of surfactants by means of reflective phantom interface method. *Lecture Notes in Electrical Engineering, Sensors*, 319:33–37, 2015.

[27] M. Cretich, G. Pirri, F. Damin, I. Solinas, and M. Chiari. A new polymeric coating for protein microarrays. *Analytical Biochemistry*, 332(1):67–74, 2004.

[28] G. W. Platt, F. Damin, M. J. Swann, I. Metton, G. Skorski, M. Cretich, and M. Chiari. Allergen immobilisation and signal amplification by quantum dots for use in a biosensor assay of IgE in serum. *Biosensors and Bioelectronics*, 52:82–88, 2014.

[29] M. Salina, F. Giavazzi, R. Lanfranco, E. Ceccarello, L. Sola, M. Chiari, B. Chini, R. Cerbino, T. Bellini, and M. Buscaglia. Multi-spot, label-free immunoassay on reflectionless glass. *Biosensors and Bioelectronics*, 74:539–545, 2015.

[30] M. Salina, F. Giavazzi, E. Ceccarello, F. Damin, Ma. Chiari, M. Ciuffo, G. Accotto,

and M. Buscaglia. Multi-spot, label-free detection of viral infection in complex media by a non-reflecting surface. *Sensors and Actuators B: Chemical*, 2015.

[31] *Membrane Technology and Applications*. McGraw-Hill, 2004.

[32] K. Smolders and a.C.M. Franken. Terminology for Membrane Distillation. *Desalination*, 72(3):249–262, 1989.

[33] C. Agarwal, a. K. Pandey, D. Pattyn, P. Ares, a. Goswami, and a. Cano-Odena. Neck-size distributions of through-pores in polymer membranes. *Journal of Membrane Science*, 415-416:608–615, 2012.

[34] J. C. Jansen, M. Macchione, and E. Drioli. On the unusual solvent retention and the effect on the gas transport in perfluorinated Hyflon AD® membranes. *Journal of Membrane Science*, 287(1):132–137, 2007.

[35] M.a Macchione, J. C. Jansen, G. De Luca, E. Tocci, M. Longeri, and E. Drioli. Experimental analysis and simulation of the gas transport in dense Hyflon® AD60X membranes: Influence of residual solvent. *Polymer*, 48(9):2619–2635, 2007.

[36] *Principles and Practice of Chromatography*. 1943.

[37] C. Charcosset, I. Limayem, and H. Fessi. The membrane emulsification process—a review. *Journal of Chemical Technology and Biotechnology*, 79(3):209–218, 2004.

[38] J. J. Meyers and a. I. Liapis. Network modeling of the convective flow and diffusion of molecules adsorbing in monoliths and in porous particles packed in a chromatographic column. *Journal of Chromatography A*, 852(1):3–23, 1999.

[39] S. M. Joscelyne and G. Traga. Membrane emulsification - A literature review. *Journal of Membrane Science*, 169(1):107–117, 2000.

[40] Ha. Yuyama, T. Watanabe, G.H. Ma, M. Nagai, and S. Omi. Preparation and analysis of uniform emulsion droplets using SPG membrane emulsification technique. *Colloids and Surfaces A: Physicochemical and Engineering Aspects*, 168(2):159–174, 2000.

[41] T. Nakashima, M. Shimizu, and M. Kukizaki. Particle control of emulsion by membrane emulsification and its applications. *Advanced Drug Delivery Reviews*, 45(1):47–56, 2000.

[42] a. R. Abate and D. a. Weitz. High-Order Multiple Emulsions Formed in Poly(dimethylsiloxane) Microfluidics. *Small*, 5(18):2030–2032, 2009.

[43] Rhutesh K. S., Ho C. S., A. C. Rowat, D. Lee, J. J. Agresti, A. S. Utada, L.-Y. Chu, J.-W. Kim, A. Fernandez-Nieves, C. J. Martinez, and D. A. Weitz. Designer emulsions using microfluidics. *Materials Today*, 11(4):18 – 27, 2008.

[44] P. Garstecki, M. J. Fuerstman, H. A. Stone, and G. M. Whitesides. Formation of droplets and bubbles in a microfluidic t-junction-scaling and mechanism of break-up. *Lab Chip*, 6:437–446, 2006.

[45] S. Sacanna, G. H. Koenderink, and A. P. Philipse. Microemulsion synthesis of fluorinated latex spheres. *Langmuir*, 20(19):8398–8400, 2004.

[46] G. H. Koenderink, S. Sacanna, C. Pathmamanoharan, M. Raşa, and A. P. Philipse. Preparation and properties of optically transparent aqueous dispersions of monodisperse fluorinated colloids. *Langmuir*, 17(20):6086–6093, 2001.

[47] R. Piazza and V. Degiorgio. Light scattering study of spherical latex particles : Measurement of surfactant adsorption and of intrinsic anisotropy. 92:45–49, 1992.

[48] S. Machlup. Noise in semiconductors: Spectrum of a two-parameter random signal. *Journal of Applied Physics*, 25(3):341–343, 1954.

[49] P. Debye, H. R. Anderson, and H. Brumberger. Scattering by an Inhomogeneous Solid. II. The Correlation Function and Its Application. *Journal of Applied Physics*, 28(6):679, 1957.

[50] *Introduction to Optics*. Prentice-Hall International, 1987.

[51] *Light Scattering by small particles*. Dover, 1957.

[52] *Dynamic Light Scattering*. Dover, 1976.

[53] I. Langmuir. The Adsorption of Gases on Plane Surfaces of Glass, Mica and Platinum. *Journal of the American Chemical Society*, 40(9):1361–1403, 1918.

[54] R. M. Weinheimer, D. Fennell Evans, and E.L. Cussler. Diffusion in surfactant solutions. *Journal of Colloid and Interface Science*, 80(2):357 – 368, 1981.

[55] H.C. Gao, R.X. Zhu, X.Y. Yang, S.Z. Mao, S. Zhao, J.Y. Yu, and Y.R. Du. Properties of polyethylene glycol (23) lauryl ether with cetyltrimethylammonium bromide in mixed aqueous solutions studied by self-diffusion coefficient {NMR}. *Journal of Colloid and Interface Science*, 273(2):626 – 631, 2004.

[56] D Brune and S Kim. Predicting protein diffusion coefficients. *Proceedings of the National Academy of Sciences of the United States of America*, 90(9):3835–3839, 1993.

[57] C. R. Wilke and P. Chang. Correlation of diffusion coefficients in dilute solutions. *AIChE Journal*, 1(2):264–270, 1955.

[58] B. Esteban Fernández de Ávila, H. M. Watkins, J. M. Pingarrón, K. W. Plaxco, G. Palleschi, and F. Ricci. Determinants of the detection limit and specificity of surface-based biosensors. *Analytical Chemistry*, 85(14):6593–6597, 2013. PMID: 23713910.

[59] S. F. Turner, , S. M. Clarke, A. R. Rennie, P. N. Thirtle, D. J. Cooke, Z. X. Li, , and R. K. Thomas. Adsorption of sodium dodecyl sulfate to a polystyrene/water interface studied by neutron reflection and attenuated total reflection infrared spectroscopy. *Langmuir*, 15(4):1017–1023, 1999.

[60] R. Atkin, † V. S. J. Craig, , and S. Biggs*. Adsorption kinetics and structural arrangements of cationic surfactants on silica surfaces. *Langmuir*, 16(24):9374–9380, 2000.

[61] M. M. George B. Sigal and George M. Whiteside. Effect of surface wettability on the adsorption of proteins and detereent. *J. Am. Chem. Soc.*, 120(14):3464–3473, 1998.

[62] W. C. Wimley and S. H White. Experimentally determined hydrophobicity scale for proteins at membrane interfaces. *Nature*, 3(10):842–848, 1996.

[63] K. D. Danov and P. A. Kralchevsky. The standard free energy of surfactant adsorption at air/water and oil/water interfaces: Theoretical vs. empirical approaches. *Colloid Journal*, 74(2):172–185, 2012.

[64] *Surfactants and Interfacial Phenomena, 4th Edition*. Wiley, 2012.

[65] T. M. Squires, R. J. Messinger, and S. R. Manalis. Making it stick: convection, reaction and diffusion in surface-based biosensors. *Nature Biotechnology*, 26(4):417–426, 2008.

[66] D. G. Myszka, X. He, M. Dembo, T. a Morton, and B. Goldstein. Extending the range of rate constants available from BIACORE: interpreting mass transport-influenced binding data. *Biophysical journal*, 75(2):583–594, 1998.

[67] Hansen, Bruus, Callisen, and Hassager. Transient convection, diffusion, and adsorption in surface-based biosensors. *Langmuir : the ACS journal of surfaces and colloids*, 28(19):7557–7563, 2012.

[68] L. Cipelletti, M. Carpineti, and M. Giglio*. Fractal morphology, spatial order, and pore structure in microporous membrane filters. *Langmuir*, 12(26):6446–6451, 1996.

[69] L. Cipelletti, M. Carpineti, and M. Giglio. Microporous membrane filters: a static light scattering study. *Physica A: Statistical Mechanics and its Applications*, 235(1–2):248 – 256, 1997. Proceedings of the Workshop on Colloid Physics.

[70] L. Cipelletti, M. Carpineti, and M. Giglio. Static light scattering characterisation of microporous membrane filters. *Journal of Molecular Structure*, 383(1–3):31 – 35, 1996. Horizons in Small Angle Scattering From Mesoscopic Systems.

[71] R. Cerbino, L. Peverini, M. a. C. Potenza, a. Robert, P. Bösecke, and M. Giglio. X-ray-scattering information obtained from near-field speckle. *Nature Physics*, 4(3):238–243, 2008.

[72] E. Iritani, S. Tachi, and T. Murase. Influence of protein adsorption on flow resistance of microfiltration membrane. *Colloids and Surfaces A: Physicochemical and Engineering Aspects*, 89(1):15 – 22, 1994.

[73] Benito-Lopez F. Diamond D. Lee L.P. Ricco A.J. Garcia-Cordero J.L., Kurzbuch D. Optically addressable single-use microfluidic valves by laser printer lithography. *Lab Chip*, 10:2680–2687, 2010.

[74] S. Scarmagnani, Z. Walsh, F. Benito Lopez, C. Slater, M.Macka, B. Paull, and D. Diamond. Photoswitchable stationary phase based on packed spiropyran functionalized silica microbeads. *e-Journal of Surface Science and Nanotechnology*, 7:649–652, 2009.

[75] Z. Walsh, S. Scarmagnani, F. Benito-López, S. Abele, F.-Q. Nie, C. Slater, R. Byrne, D. Diamond, B. Paull, and M. Macka. Photochromic spiropyran monolithic polymers: Molecular photo-controllable electroosmotic pumps for micro-fluidic devices. *Sensors and Actuators B: Chemical*, 148(2):569 – 576, 2010.